AFOSR-TR-96

0376

REPORT DOCUMENTATION PAGE

1. AGENCY USE ONLY *(Leave blank)*

2. REPORT DATE
June 1996

3. REPORT .... AND DATES COVERED
Annual - June 1994 - June 1995

4. TITLE AND SUBTITLE
Development of LES Methodology for the Analysis of High - Reynolds Number 2-D and 3-D Dynamic Stall Phenomenon

5. FUNDING NUMBERS
AFOSR
F49620-93-1-0393
2307/A3

6. AUTHOR(S)
K.N. Ghia and U. Ghia

7. PERFORMING ORGANIZATION NAME(S) AND ADDRESS(ES)
University of Cincinnati
Department of Aerospace Engineering & Engineering Mechanics
Department of Mechanical, Industrial, & Nuclear Engineering

8. PERFORMING ORGANIZATION REPORT NUMBER
AFL Report No.
95-6-83

9. SPONSORING/MONITORING AGENCY NAME(S) AND ADDRESS(ES)
Air Force Office of Scientific Research
Aerospace Sciences
Building 410
Bolling Air Force Base, DC 20332-6648

NA

10. SPONSORING/MONITORING AGENCY REPORT NUMBER
93-1-0393

11. SUPPLEMENTARY NOTES

19960726 052

12a. DISTRIBUTION/AVAILABILITY STATEMENT
Distribution of this report is unlimited.

13. ABSTRACT *(Maximum 200 words)*

The ultimate objective of this project was to analyze forced unsteady separated flows, through numerical simulation of high-Reynolds number flows. The velocity-vorticity form of the Navier-Stokes equations were to be solved using the Large-Eddy Simulation (LES) or the coarse-grid Direct Numerical Simulation (DNS) approaches. In the first year of this project, an effort was initiated and reported to develop LES technique for forced unsteady separated flows using $\left(\overline{\varpi}-\overline{V}\right)$ formulation. Although an effort, which was spearheaded to obtain 3-D simulation of $\left(\overline{\varpi}-\overline{V}\right)$ formulation, required additional theoretical work due to an incomplete boundary condition at the surface for vorticity, the corresponding 2-D results were obtained using a backstep duct geometry and presented at the 14th International Conference on Numerical Methods in July 1994. This effort was carried out in the background, while new projects have been initiated.

14. SUBJECT TERMS
Unsteady Flow
Stability
Transition
Large Eddy Simulation
Direct Num. Simulation
2-D & 3-D Flow
Plane & Curved Channel Flow
Navier-Stokes Eqs.
Spectral Tech.

15. NUMBER OF PAGES
149

16. PRICE CODE

17. SECURITY CLASSIFICATION OF REPORT
U

18. SECURITY CLASSIFICATION OF THIS PAGE
U

19. SECURITY CLASSIFICATION OF ABSTRACT
U

20. LIMITATION OF ABSTRACT

DTIC QUALITY INSPECTED 1

Table of Contents

List of Figures v

List of Tables ix

Section 1. Introduction 1

1.1. Mechanisms of Transition to Turbulence in Wall-bounded Shear Flows . 2

1.1.1. Stages of Instability and Transition in Shear Layers 3

1.1.2. Linear Mechanisms 5

1.1.3. Nonlinear Growth and Interaction of Instability Waves 7

1.1.4. Applications of Instability Theory in Canonical Flows 10

1.2. Channel Flows 11

1.2.1. Plane Channel 12

1.2.2. Curved Channel 14

1.3. The Roles of Spatial and Temporal Numerical Simulations 16

1.3.1. Assumptions of Theoretical Approaches 17

1.3.2. Numerical Simulation of Spatially Developing Flows 19

1.3.3. Temporally Developing Flows 21

1.4. Goals of this Study 22

Section 2. Mathematical Formulation 24

2.1. Governing Equations and Base Flow Solutions 24

2.1.1. Vector Form of Incompressible Time-Dependent Navier-Stokes Equations 25

2.1.2. Generalized Curvilinear Coordinates 27

2.1.3. Contravariant Form of Navier-Stokes Equations 30

2.1.4. Plane Channel Geometry 32

2.1.5. Curved Channel Geometry 33

2.1.6. Forcing Function Analysis 37

2.2. Linear Stability Theory 37

2.2.1. General Parallel Flow Formulation 38

2.2.2. Plane Channel Flow Stability Equations 39

2.2.3. Curved Channel Flow Stability Equations 41

2.3. Summary 42

Section 3. Numerical Approach 43

3.1. Spectral Methods 44

3.1.1. Model Problem 45

3.1.2. Fourier Galerkin Method 47

3.1.3. Fourier Collocation Method 48

3.1.4. Chebyshev Collocation Method 51

3.1.5. Chebyshev Collocation Method on a Staggered Grid 55

3.1.6. Chebyshev Quadrature 56
3.1.7. Summary 56
3.2. Spatial Discretization of Governing Equations 57
3.2.1. Discretization in the Spanwise Direction 58
3.2.2. Discretization in Streamwise and Wall-Normal Directions 59
3.2.3. Final Spatially Discrete Matrix System 62
3.3. Temporal Discretization and Solution Method 63
3.3.1. Temporal Discretization 64
3.3.2. Iterative Solution Method 66
3.3.3. Comparison with Previous Studies 68
3.4. Initial Condition 69
3.4.1. Discrete Linear Stability Modes for Plane Channel Flow 70
3.4.2. Discrete Linear Stability Modes for Curved Channel Flow 72
3.5. Solution Output 73
3.5.1. Summary of Output Flow Quantities 75
3.5.2. Spectral Analysis 76
3.6. Summary 79

Section 4. Plane and Curved Channel Results 80
4.1. Analytical Function Testing 82
4.1.1. Test Solutions 83
4.1.2. Streamwise Accuracy 84

4.1.3. Wall-Normal Accuracy 88

4.1.4. Temporal Accuracy 92

4.1.5. Condition Number Issues 95

4.2. Comparison to Linear Stability Theory for Plane Channel Flow 96

4.2.1. Linear Stability Theory Results 97

4.2.2. Temporal Analysis Results 104

4.3. Comparison to Linear Stability Theory for Curved Channel Flow 110

4.3.1. Linear Stability Theory Results 111

4.3.2. Temporal Analysis Results 115

4.4. Nonlinear Stability Results for Plane Channel Flow 121

4.4.1. Early Time Results 122

4.4.2. Long Time Growth of the Primary Mode 125

4.4.3. Evolution of Harmonic Modes 128

4.4.4. Finite Amplitude State for Plane Channel Flow 133

4.5. Summary 137

Section 5. Conclusions and Recommendations 139

5.1. Nonlinear Wave Interactions 139

5.2. Linear and Nonlinear Stability of Complex Flows 140

5.3. Dynamical Systems Explanations of Turbulence 142

5.4. Summary 143

Bibliography 144

List of Figures

Figure 4.1. Contours of the Prescribed Solution for Streamwise Discretization Analysis of Plane Channel Flow, Case A. 85

Figure 4.2. Demonstration of Spectral Accuracy in the Streamwise Discretization for Plane Channel, Case A. 86

Figure 4.3. Demonstration of Spectral Accuracy in the Streamwise Discretization for Plane Channel, Case B. 87

Figure 4.4. Contours of Error in Solution at t=0.01 for Plane Channel, Case B, with N_1=12, N_3=12. 87

Figure 4.5. Prescribed Solution for Wall-Normal Discretization Analysis of Plane Channel Flow, Case C. 89

Figure 4.6. Spectral Accuracy is Obtained in the Wall-Normal Discretization for Plane Channel, Case C. 90

Figure 4.7. Solution Error Due to Wall-Normal Discretization for Plane Channel, Case D. 90

Figure 4.8. Contours of Error in Solution for Plane Channel, Case D with N_1=12, N_3=12. 91

Figure 4.9. Demonstration of Second-Order Accuracy in Time for Plane Channel, Case E. 92

Figure 4.10. Demonstration of Second-Order Accuracy in Time for Plane Channel, Case E. 93

Figure 4.11. Contours of Solution Error at t=0.01 for Plane Channel, Case E. 93

Figure 4.12. Mode Shapes for Plane Channel, Case 1. 99

Figure 4.13. Mode Shapes for Plane Channel, Case 2. 99

Figure 4.14. Contours of Disturbance Quantities for Plane Channel, Case 1. 100

Figure 4.15. Contours of Disturbance Quantities for Plane Channel, Case 2. 100

Figure 4.16. Contours of Disturbance u^3 for Plane Channel, Case 1, t=0.1T. 101

Figure 4.17. Contours of Disturbance u^3 for Plane Channel, Case 1, t=1.0T. 102

Figure 4.18. Growth of Disturbance Mode Kinetic Energy Compared to Linear theory, Plane Channel, Case 1. 103

Figure 4.19. Effect of Spatial Resolution on Computed Linear Frequency, ω_R, for a) Case 1, and b) Case 2. 108

Figure 4.20. Effect of Spatial Resolution on Computed Linear Growth Rate, ω_I, for a) Case 1, and b) Case 2. 108

Figure 4.21. Effect of Temporal Resolution on Computed Linear Frequency, ω_R, for a) Case 1, and b) Case 2. 109

Figure 4.22. Effect of Temporal Resolution on Computed Linear Growth Rate, ω_I, for a) Case 1, and b) Case 2. 109

Figure 4.23. Effect of Disturbance Amplitude on Computed Linear Frequency, ω_R, for a) Case 1, and b) Case 2. 111

Figure 4.24. Effect of Disturbance Amplitude on Computed Linear Growth Rate, ω_I, for a) Case 1, and b) Case 2. 111

Figure 4.25. Mode Shapes for Curved Channel, Case 3. 113

Figure 4.26. Mode Shapes for Curved Channel, Case 4. 113

Figure 4.27. Disturbance Quantities for the Tollmien-Schlichting Wave Initial Condition for the Curved Channel, Case 3. 114

Figure 4.28. Disturbance Quantities for the Tollmien-Schlichting Wave Initial Condition for the Curved Channel, Case 4. 115

Figure 4.29. Disturbance kinetic energy for one period *T* for Curved Channel, Case 3. 116

Figure 4.30. Effect of Spatial Discretization on Computed Linear Frequency for Curved Channel, a) Case 3, and b) Case 4. 120

Figure 4.31.Effect of Spatial Discretization on Computed Linear Growth Rate, ω_I, for a) Case 3, and b) Case 4. 121

Figure 4.32. Effect of Temporal Discretization on Computed Linear Frequency for Curved Channel, a) Case 3, and b) Case 4. 121

Figure 4.33. Effect of Temporal Discretization on Computed Linear Growth Rate, ω_I, for a) Case 3, and b) Case 4. 122

Figure 4.34. Effect of Disturbance Amplitude on Computed Linear Frequency for Curved Channel, a) Case 3, and b) Case 4. 122

Figure 4.35. Effect of Disturbance Amplitude on Computed Linear Growth Rate, ω_I, for a) Case 3, and b) Case 4. 123

Figure 4.36. Growth of the primary disturbance mode for one period, *T*, of the Tollmien-Schlichting wave, for the plane channel, Case 1, with $Re = 8{,}000$ and $\alpha = 1.0$. 125

Figure 4.37. Growth of the primary disturbance mode for one period, *T*, of the Tollmien-Schlichting wave, for the plane channel, Case 2, with $Re = 4{,}000$ and $\alpha = 1.25$. 126

Figure 4.38. Growth of the primary disturbance mode for 10 periods of the Tollmien-Schlichting wave, for the plane channel, Case 1, with *Re* = 8,000 and α = 1.0. 128

Figure 4.39. Growth of the primary disturbance mode for 5 periods of the Tollmien-Schlichting wave, for the plane channel, Case 2, with *Re* = 4,000 and α = 1.0. 129

Figure 4.40. Growth of the primary disturbance mode (1,0) and its harmonics (2,0), (3,0), and (4,0) for 5 periods of the Tollmien-Schlichting wave, for the plane channel, Case 1. 132

Figure 4.41. Growth of the primary disturbance mode (1,0) and its harmonics (2,0), (3,0), and (4,0) for 20 periods of the Tollmien-Schlichting wave, for the plane channel, Case 2. The initial amplitude is 0.001 133

Figure 4.42. Growth of the primary disturbance mode (1,0) and its harmonics (2,0), (3,0), and (4,0) for 20 periods of the Tollmien-Schlichting wave, for the plane channel, Case 2. The initial amplitude is 0.1. 134

Figure 4.43. Contours of disturbance quantities after 20 periods of the Tollmien-Schlichting wave for the plane channel, Case 2. 136

Figure 4.44. Contours of total streamwise velocity and vorticity after 20 periods of the Tollmien-Schlichting wave for the plane channel, Case 2. 138

Figure 4.45. Vectors and streamlines of the disturbance velocity after 20 periods of the Tollmien-Schlichting wave for the plane channel, Case 2. 138

List of Tables

Table 4.1. Test Cases for Analytical Function Tests. 85

Table 4.2. Temporal Stability Simulation Test Cases. 96

Table 4.3. Effect of Spatial Resolution on Computed Temporal Frequency ω_R and Temporal Growth Rate ω_I for Plane Channel. 105

Table 4.4. Effect of Temporal Resolution on Computed Temporal Frequency ω_R and Temporal Growth Rate ω_I for Plane Channel. 106

Table 4.5. Effect of Disturbance Amplitude on Computed Temporal Frequency ω_R and Temporal Growth Rate ω_I for Plane Channel. 107

Table 4.6. Effect of Spatial Resolution on Computed Temporal Frequency ω_R and Temporal Growth Rate ω_I for Curved Channel. 118

Table 4.7. Effect of Temporal Resolution on Computed Temporal Frequency ω_R and Temporal Growth Rate ω_I for Curved Channel. 119

Table 4.8. Effect of Initial Amplitude on Computed Temporal Frequency ω_R and Temporal Growth Rate ω_I for Curved Channel. 120

Section 1. Introduction

The study of fluid dynamics began long before manned flight, and has progressed to the present day along with the science of aerospace engineering. In the aerospace industry, designs are pushed to the limit of current technological capabilities. The technology of flight involves the understanding of a complex set of aerodynamic phenomena that accompany flight. The complexity of the aerodynamic flows over flight vehicles is due in part to the shape and mission of these vehicles, but an even greater obstacle in fully understanding and predicting aerodynamic behavior is the complexity inherent in the equations governing the dynamics of fluid flows. Though the incompressible Navier-Stokes equations, which govern fluid flows at low Mach numbers, are simple in form, the non-linearity in the equations admits solutions of a chaotic nature. It is the nature of fluid flows to break down and transition to a turbulent state at a sufficiently high Reynolds number. In a turbulent state, the full range of scales of motion are active, from the length scale of the vehicle under consideration down almost to the molecular level.

In 1883, Reynolds in his classic experiment on pipe flows, determined that transition to turbulence was a result of the instability of the smooth, laminar flow with respect to small perturbations. Instability can occur in many forms and at many different scales in a complex fluid flow. Boundary layers occur near vehicle surfaces in regions of attached flow. As boundary layers grow downstream of some originating location, they become unstable and allow transition to a turbulent boundary layer. This layer, though significantly thicker than its laminar counterpart, is still thin with respect to the macroscopic features of the fluid flow. However, the turbulent boundary layer causes higher levels of skin friction and heat transfer. It also decreases the likelihood of flow separation due to the higher level of kinetic energy in the boundary layer. Instability is also observed in shear layers separated from the body in the form of the breakdown of large scale structures into smaller, disordered structures. Similarly, vortices are often observed to have a coherent, laminar region followed by a breakdown to a disordered state that no longer resembles a vortex. In all of these cases, the breakdown of ordered flow drastically changes the nature of the flow, and consequently, the aerodynamic performance of the vehicle under consideration.

In recent years, great progress has been made in the understanding of instability and transition to turbulence. Often advances are made by the investigation of flows involving simple geometries rather than flows over complex shapes. From the examination of transition to turbulence of these simple flows, the basic features of transition in more complex flows can be studied. In this study, the instability and transition in channel flows is investigated. This chapter begins with the development of a theoretical framework for investigating transition to turbulence in terms of the simplified problem of instability in 2-D channel flows, presented in §§1.1 and 1.2. The role of numerical simulations in studying these flows is outlined in §1.3. The chapter concludes with a summary of the specific goals of this study, in §1.4.

1.1. Mechanisms of Transition to Turbulence in Wall-bounded Shear Flows

Though transition to turbulence in fluid flows of engineering interest takes many different forms and is still largely beyond the realm of predictability, recent progress has been significant. The early stages of the transition process in certain canonical flows have been studied in great depth to identify the physical mechanisms of instability. It is expected that these mechanisms are indicative of the causes of transition to turbulence in more complex flows.

1.1.1. Stages of Instability and Transition in Shear Layers

The flows of interest for aerodynamic applications are those of homogeneous incompressible or compressible Newtonian fluids. These flows are induced by the motion of a body through the fluid. The fluid, which must stick to the surface of the body, undergoes shearing forces in regions near the body and in the wake of the body. These *shear layers* are the sites at which transition to a turbulent state may occur. The typical process of transition in shear flows can be considered to consist of four stages: namely receptivity, linear instability, weakly nonlinear instability, and nonlinear breakdown (Reed and Saric, 1989, Blodgett, 1995).

The first stage of the transition process, *receptivity*, is one of the least understood. It is the process by which disturbances become imbedded in the shear layer. The source of the disturbance may be the flow far away from the body and may reach the body in terms of acoustic waves. It may, for example, be turbulence in the freestream flow passing over the body, or it may be bumps and imperfections in the body surface which provide the disturbance. The receptivity stage is complete when it has triggered an instability mechanism in the shear flow, which can then proceed down the path to turbulence. The study of receptivity is a major area of current research. Reviews can be found in Choudhari (1993) and Blodgett (1995).

The second stage, *linear instability*, is by far the most well understood. Linear instability is the study of the initial appearance of disturbance waves in a shear flow.

These *linear instability waves*, though presumed to be triggered by some receptivity mechanism, are greatly determined by the nature of the shear flow itself . One explanation of the linear instability mechanism due to the equilibrium of forces present in a fluid. In a shear flow, the fluid moves according to its inertia, and its internal stresses due to pressure and friction. These forces must always remain in equilibrium. When the equilibrium is stable, a small disturbance that shifts the flow away from its equilibrium will not upset the balance of forces, and the flow will return to equilibrium after some time. However, if the equilibrium is unstable to a particular type of disturbance, it is possible to upset the balance in such a way that the flow cannot return to its original equilibrium, even if the amplitude of the disturbance is infinitesimally small.

The particular disturbance to which the shear flow is most unstable is designated as the *primary linear instability wave* for that flow. It is assumed that the receptivity mechanism will select and feed energy into this instability. In disturbance environments in which many types of small disturbances are present, the most unstable linear wave will be excited. However, it is possible to force specific instability waves in the flow by imposing a disturbance of a certain type, e.g. of a certain frequency. In this case, the nature of linear instability waves are determined both by the susceptibility of the shear flow to disturbances and the type of the disturbances imposed. In general, though, it is sufficient to assume that the transition process is initiated with the growth of the most unstable linear wave. The search for the primary instability of a shear flow is performed using linear stability theory, which is outlined in §1.1.2.

The third stage of the transition process considers the evolution of the primary instability once it has grown to a noticeable amplitude in the shear flow. The primary instability evolves nonlinearly according to the Navier-Stokes equations. It also interacts with any other disturbances present in the flow. The field of *weakly-nonlinear stability theory* considers the self- and mutual-interactions of small amplitude instability waves to determine the long-time evolution of a disturbance once it is generated. This approach will be discussed in §1.1.3.

Once instability waves grow out of the range of "small amplitude," rapid breakdown is often observed, producing the highly disordered state generically called turbulence. The final stage of transition to turbulence, *nonlinear breakdown*, is a combination of all the stages following the weakly-nonlinear stability stage until a fully turbulent state is achieved. The only approaches to understanding this flow regime are experimental measurements and direct simulations of the Navier-Stokes equations using very high resolution. Theoretical and statistical tools for investigating turbulence itself can be used to probe these experimental and computational measurements of the transition regime with hopes of identifying the underlying structure of turbulence. From this perspective, much work has been done in the investigation of nonlinear breakdown. A review can be found in Kachanov (1994).

1.1.2. Linear Mechanisms

The earliest method for examining stability of fluid flows is still the most important tool for understanding the transition process. Linear stability theory begins by representing a solution to the Navier-Stokes equations as some known solution, called the *base state* or *base flow*, plus a small perturbation. Neglecting terms that are nonlinear in perturbation quantities, a linearized set of governing equations is obtained. Next, the disturbance is assumed to be periodic in at least one direction, typically the streamwise and/or spanwise directions. The solution to this linear system is then considered as a superposition of Fourier modes in the periodic direction(s). Complex exponential variation is assumed in time for each mode. The study of the stability of this linearized system then becomes the search for eigensolutions for each Fourier mode. Each of the resulting eigenvectors is a mode shape of the perturbed flow. The corresponding eigenvalue contains the growth rate for that mode as its imaginary part, and the frequency of oscillation of that mode as its real part. This modal decomposition of the flow allows the search for the "most dangerous mode," or the mode with the most positive growth rate, given the various other parameters in the analysis, such as the Reynolds number and spatial wavelength(s). If the growth rate of this mode is positive, the base state is said to be linearly unstable. The standard text on linear stability theory is Drazin and Reid (1981). See also Bayly, Orszag and Herbert (1988) and Reed and Saric (1989).

Certain pieces of information are conspicuously missing from the modal decomposition explanation of instability. At first glance, it seems that linear theory simply describes whether or not a base state is linearly unstable; and if unstable, it provides the characteristic shape of the disturbance that activates the instability. However, linear instability does not predict the evolution of the flow, once departed from the base state. Also, it does not predict the response of the base state to a disturbance of finite size. It also is incapable of estimating the amplitude of the disturbance that will be present. For these reasons, linear stability theory alone is incapable of predicting transition to turbulence.

However, the most dangerous mode of the linear stability problem is often observed in experiments to dominate all other modes that might be present, and to grow to measurably large amplitude before other types of instability can grow to noticeable size. This is evidence that the most unstable linear mode plays a significant role in the transition process. In fact, Henningson and Reddy (1994) show that linear mechanisms must be present for nonlinear growth of disturbances to occur. Thus, in spite of its limitations in providing information on the evolution of instabilities, linear theory does often shed light on the inception of the transition process.

1.1.3. Nonlinear Growth and Interaction of Instability Waves

The limitations of linear theory for predicting transition led researchers to investigate the role of nonlinear mechanisms in the transition process. Though many approaches have been followed in considering the transition process, a fairly unified perspective and mathematical treatment of nonlinearity in the Navier-Stokes equations has become dominant. This approach is called *weakly-nonlinear stability theory*. In this approach, the primary instability wave is assumed to force its higher harmonics through the nonlinear convective term in the Navier-Stokes equations. The theory assumes that the primary disturbance is small, but not infinitesimal, and forces its harmonics at a finite level. The interaction of the primary disturbance with its harmonics modulates the growth of the primary as it feeds some of its energy into its harmonics.

Assuming that the primary disturbance amplitude is very small, its weakly nonlinear evolution is given by the Landau equation (Drazin and Reid, 1981). The Landau equation is an ordinary differential evolution equation in time for the modulus of the amplitude of the primary disturbance, given its initial value:

$$\frac{d}{dt}|A|^2 = 2\omega|A|^2 - \ell|A|^4 \qquad \textbf{(1.1)}$$

where ω is the growth rate from linear theory, and ℓ is the so-called *Landau coefficient*. As the amplitude becomes infinitesimal, the fourth-order term becomes negligible, and the solution reverts to that predicted by linear theory, i.e., an exponential in time:

$$|A|^2 = A_0^2 e^{2\omega t} \Rightarrow |A| = A_0 e^{\omega t} \tag{1.2}$$

where $A_0 = |A(t=0)|$ is the initial amplitude. For finite amplitude, the modulus of the amplitude is given in closed form as a function of time:

$$\frac{|A|^2}{A_0^2} = \left\{ \frac{\ell}{2\omega} A_0^2 + \left(1 - \frac{\ell}{2\omega} A_0^2 \right) e^{-2\omega t} \right\}^{-1} \tag{1.3}$$

As shown in Drazin and Reid (1981), the Landau equation predicts four categories of weak coupling between the primary mode and its harmonics, depending on the sign of the ω and ℓ.

1. For $\omega<0$, the flow is linearly stable. That is, infinitesimal disturbances will decay.
    a. For $\ell>0$, both terms on the right hand side of Eq. (1.1) are of the same sign, and a finite size disturbance will decay.
    b. For $\ell<0$, the two terms of Eq. (1.1) are of opposite sign. For initial amplitudes below the threshold value of:

    $$A_e \equiv \left(\frac{2\omega}{\ell} \right)^{1/2} \tag{1.4}$$

    the disturbance will decay, but for amplitudes above the threshold value, the disturbance will grow rapidly. This condition is called *subcritical instability.* Though the Reynolds number is below the critical value for linear instability, the base flow is unstable if a large enough disturbance is imposed.

2. For $\omega>0$, the flow is linearly unstable. Infinitesimal disturbances will grow exponentially, and the solution will depart rapidly from the base flow solution.

    c. For $\ell>0$, the fourth-order term is of opposite sign to the linear term. Therefore, when the disturbance grows to a finite amplitude, its growth will be slowed until a threshold value, again given by Eq. (1.4), is approached. The solution will then remain at this solution for all time. Also, if the initial amplitude is larger than the threshold value, the solution will decay to the threshold value. This condition is called *supercritical stability*. Though the flow is linearly unstable, a small but finite amplitude stable solution will be obtained when the base flow is perturbed. This process can also be considered as a bifurcation of the unstable base flow to a new flow in which the nonlinear interactions are in equilibrium.

    d. For $\ell<0$, the two terms of Eq. (1.1) are of the same sign. The nonlinearity will enhance the growth of the disturbance as it increases in magnitude.

This theory is the simplest example of the theoretical framework used to understand nonlinear interactions which occur early in the transition process. It introduces the concepts of subcritical instability and supercritical stability. The Landau equation is a subset of a more general perturbation-methods approach in which multiple levels of wave interactions are considered. Numerous recent studies have greatly expanded knowledge in this area. See Herbert (1988b), Reed and Saric (1989), Crouch and Herbert (1993), and Singer, Erlebacher and Zang (1992) for reviews and examples.

1.1.4. Applications of Instability Theory in Canonical Flows

How can the above concepts be investigated for the flow over a flight vehicle in real flight conditions? A simplified understanding of the stability of such a flow can be obtained by performing an experiment on the flight vehicle to characterize and measure the shear layers on the vehicle. Boundary layers, separated regions, wakes, and jets are all shear layers that occur over flight vehicles. Is breakdown evident in these structures? Is there a definite transition location at which the flow becomes turbulent? What is the spatial extent of the transition region?

Many of the answers to explaining the observed flow features lie in the investigation of the stages of transition in canonical flows such as the plane boundary layer. Receptivity mechanisms can be used to explain when and if instabilities occur in certain test conditions and thus lead to the hope of control of instabilities. The earliest stage of instability is often observed to match the primary instability wave predicted by linear theory. The subsequent growth of this wave can often be explained by weakly-nonlinear theory. The nonlinear breakdown and fully turbulent regions can be understood in terms of measurements of transition and turbulence in canonical flows. Thus canonical flows provide answers that apply to many types of more complex flows. This approach is incomplete in explaining all of the features of transition, and is painfully lacking in the ability to predict when and where transition will occur in the flow over a complex geometry. However, it provides a fundamental understanding of transition, which is a necessary prerequisite to advanced prediction capabilities. The application of studies of the stability of canonical flows to the understanding of transition in complex flows are given in Kaiktsis, Karniadakis and Orszag (1991) and Karniadakis and Triantafyllou (1992).

Channel flows comprise a particularly simple class of canonical flows. Though channel flows are internal flows, the stability and transition characteristics of channel flows closely match those of boundary layers. Because they are internal flows, the computational and mathematical framework for their investigation is much simpler because the domain is small and wall-bounded. These flows may examined in greater depth than corresponding boundary layer flows.

In this study, the linear and weakly non-linear stages in the growth of small, prescribed disturbances will be examined in the setting of 2-D channel flows. The receptivity stage is assumed to have already occurred, allowing disturbances of a known type to be present in the flow. Furthermore, the highly nonlinear stages characterized by rapid evolution and breakdown of 3-D structures in the flow will be assumed to occur after the flow has evolved according to linear and weakly-nonlinear mechanisms. These concepts are applied specifically to channel flows in the following section.

1.2. Channel Flows

For the purposes of this study, *channel flows* will described as flows between two stationary infinite plates, induced by a mean pressure gradient. The walls may be curved in the streamwise-wall normal plane, but may not be curved in the spanwise direction. The flow will be induced by either a constant mean pressure gradient in the streamwise direction, or by a variable mean pressure gradient adjusted to maintain a constant streamwise flow rate in the channel. Flows in this category include the plane channel, or Poiseuille flow, and curved channel, or Taylor-Dean flow, both of which are 1-D geometries and have 1-D analytical base flow solutions. The more general class of periodic 2-D channel flows do not have analytical base flow solutions. Examples are plane and curved channels with streamwise periodic constrictions, expansions, grooves, or wavy walls. Examples of studies of complex channel flows are Guzmán and Amon (1994), Roberts (1994), Sobey and Drazin (1986), Amon and Patera (1989), Ghaddar *et al.* (1986), and Karniadakis, Mikic and Patera (1988).

Many of the features of transition observed in experiments on boundary layers and more complex flows have been thoroughly investigated using simple channel flow geometries. Different types of channel geometries demonstrate very different routes to turbulence. Plane channel flow is one of the simplest examples of a flow which exhibits subcritical instability, while curved channel flow exhibits supercritical stability. The initial nonlinear stages of instability give plane and curved channel flows very different routes to turbulence. In fact, these two canonical flows serve as examples of the two major categories of routes to turbulence: the secondary instability route to turbulence, and the Ruelle-Takens-Newhouse scenario.

1.2.1. Plane Channel

Plane channel flow is one of the canonical settings for the secondary instability route to turbulence. In spite of the simplicity of the base flow solution, the explanation of the transition scenario occurring in plane channel flow is still a topic of debate and continued study. However, a general framework for the early stages of transition in plane channel flow has been agreed upon and argued to be typical of a broad range of flows susceptible to secondary instabilities. See the studies of Orszag and Patera (1983), Singer, Reed and Ferziger (1989) and Zang and Hussaini (1985, 1987, and 1990) and the review of Kleiser and Zang (1991).

The first stage of the transition process in plane channel flow is the growth to a finite amplitude of a primary instability mode superimposed on the 1-D parabolic base flow. Though many types of linear instability modes exist in plane channel flow, such as

2-D Tollmien-Schlichting modes, oblique Tollmien-Schlichting modes, streamwise center modes, and streamwise vortex modes, the base flow is linearly stable to all of these disturbances at Reynolds numbers at which transition to turbulence has been observed in experiments, Reynolds numbers as low as 1,000. However, weakly nonlinear theory for channel flow predicts subcritical instability of the 2-D Tollmien-Schlichting mode for an initial disturbance amplitude above a threshold value, for Reynolds number above 2,900 and below the critical Reynolds number of 5,772. Furthermore, for Reynolds below 2,900, nonlinear self-interaction of the finite-amplitude Tollmien-Schlichting mode causes it to decay on a slow, viscous time scale, effectively lowering the threshold Reynolds number for which further bifurcations may occur (Orszag and Patera, 1983).

The initial departure from a 2-D finite-amplitude state to a 3-D state is the result of a linear instability of the 2-D state to spanwise disturbances. This is called *secondary instability*. Experiments and numerical simulations have shown that the spanwise, secondary instability leads to the creation of 3-D vortical structures called Λ (lambda) vortices. These structures grow to a finite amplitude, and then rapidly break down, presumably to some tertiary instability. This process continues until a turbulent state is reached. The scenario by which instability modes grow in time to a finite amplitude and then become unstable to other instability modes, with this process continuing until full nonlinear breakdown is achieved, is called the *secondary instability route to turbulence* (Orszag and Patera, 1983, Bayly, Orszag and Herbert, 1988, Reed and Saric, 1989, Herbert, 1988b).

The progression of the 2-D Tollmien-Schlichting state with a linearly growing spanwise instability mode is not unique, but is highly dependent on the disturbance environment. Nonlinear interactions between various linear stability modes present in the initial flow can cause different 3-D states to result. In particular, theoretical attention has been given to the interaction of streamwise vortices (linear vortex modes), the finite-amplitude Tollmien-Schlichting wave, and the secondary instability mode (Hall and Smith, 1989, Nayfeh and Al-Maaitah 1988, Orszag and Patera, 1983).

The growth of the secondary instability mode is followed quickly, i.e., on a convective time scale, by breakdown to turbulence. Observations of this breakdown suggest that the secondary instability mode grows, with nonlinear interaction with other linear modes, into a lambda vortex structure. The time evolution of this vortex structure can be considered in terms of inviscid vortex filament concepts. The bent vortex shape will be unstable and will have a tendency to pull together like a hairpin, stretching in the streamwise direction, and then breaking apart leaving streamwise streaks at the wall. This explanation is satisfying to those who observe similar structures in fully-developed turbulence in channels and boundary layers.

1.2.2. Curved Channel

The flow in a channel with constant radius of curvature exhibits qualitatively different behavior than plane channel flow even for very slight curvature.

The most dominant instability mode of curved channel flow even with small levels of curvature is a pair of counter-rotating stationary streamwise vortices. This flow, called Dean vortex flow, results from instability of the base flow to spanwise disturbances. The wavelength of the Dean vortex mode (a single pair of counter-rotating vortices) is approximately 2.5 times the channel height.

For Reynolds numbers below the critical value given by linear theory, curved channel flow is stable, even to finite size disturbances. Above the critical Reynolds number, the base flow is unstable and a Dean vortex mode will grow. However, the vortex mode will saturate at a small finite amplitude. Thus curved channel flow follows the supercritical stability model. The growth and final amplitude of the Dean vortex mode can be qualitatively predicted by weakly nonlinear theory. This vortex flow is stable to streamwise disturbances for a large range of Reynolds number.

The route to turbulence in curved channel flow is currently thought to follow the Ruelle-Takens-Newhouse scenario. The route to turbulence is understood in terms of the bifurcations undergone by the flow as the Reynolds number is slowly increased. At a fixed Reynolds number between the critical Reynolds number and the value at which full nonlinear breakdown is observed, the flow will settle into an intermediate finite-amplitude state dependent on the Reynolds number. As the Reynolds number is increased the flow will bifurcate from to a more complex state. The *Ruelle-Takens-Newhouse scenario* suggests that the first bifurcation of the flow is from the base state to a periodic flow with frequency ω_1. At higher Reynolds number, this flow will bifurcate to one with two incommensurate frequencies, ω_1 and ω_2, that is ω_1 is not an integer multiple of ω_2 and vise versa. This results in a so-called *quasi-periodic* state. Eventually, a state will appear with three frequencies. Dynamical systems theory predicts that after the appearance of the third incommensurate frequency, any disturbance will trigger chaos. In the Ruelle-Takens-Newhouse scenario, a quasi-periodic flow with three frequencies is rapidly followed by turbulence (Guckenheimer, 1986).

This describes the route to turbulence in curved channel flow. Starting with the Dean vortex flow as the base flow, a critical Reynolds number (dependant on the curvature) exists above which the flow is linearly unstable to a traveling streamwise disturbance. The flow at a particular point is then periodic with frequency ω_1. Two different types of streamwise instability modes have been found (Finlay, Keller and

Ferziger, 1988, Bland and Finlay, 1991). For lower Reynolds numbers, a long wavelength disturbance can yield an "undulating" vortex similar to the wavy vortex mode found in Taylor-Couette flow. For higher Reynolds numbers and greater channel curvature, a "twisting" vortex with a shorter disturbance wavelength is more unstable and becomes dominant. At higher Reynolds number, the flow in computations has been observed to be quasi-periodic with two, then three frequencies, suggesting the Ruelle-Takes-Newhouse scenario for curved channel flow.

1.3. The Roles of Spatial and Temporal Numerical Simulations

As seen from the descriptions above, the transition to turbulence in wall-bounded shear flows is a complex process, one which has challenged researchers for over a century. Progress in the qualitative understanding of the mechanisms of instability, saturation, bifurcation and chaos has been accompanied by progress in the prediction of quantitative aspects of transitional flow, such as mode shapes and growth rates, critical Reynolds numbers and amplitudes of saturated states. Progress has been obtained through cooperation and dialog between researchers using many different techniques for studying transition. In many of the studies cited above, experimental observations were used as the impetus for the research. Numerical simulation studies of transition are invariably accompanied by stability theory results and predictions. Theoretical studies rely heavily on numerical methods for solving the derived equations. All of the methods for studying transition explain observed behavior in the language of mathematics of nonlinear systems.

In this study, numerical simulation methods are used to study the early stages of transition in channel flows. Two basic approaches may be taken to the numerical simulation of the stability of flows. For spatially periodic base flows, the temporal simulation method is used the most often. For non-periodic flows, i.e., those with spatial development, the spatial approach is more appropriate. These two approaches, along with the theoretical framework for the numerical investigation of flow instability and transition in channel flows is described in the following sections.

1.3.1. Assumptions of Theoretical Approaches

Theoretical approaches to the study of the Navier-Stokes equations by necessity involve assumptions and approximations. Asymptotic methods find approximate solutions of the Navier-Stokes equations using a truncated infinite series in powers of a small parameter. Truncation of the system results in simplified equations for which solutions can be sought. Linearization of the governing equations, and thus linear stability theory, results from the first-order truncation of the series. Weakly nonlinear theory is obtained by retaining additional terms in the truncation. These approximations are valid only in a certain range of the perturbation parameter. This type of approximation gives the bounds of applicability of theoretical results. See Crouch and Herbert (1993) for a complete example.

Another type of approximation used in most theoretical approaches is the simplification of the boundary conditions from those required for an exact solution to the problem. In particular, most stability theories replace the physical domain used in experiments, which will contain inflow and outflow regions and side walls, with a periodic domain of a given length. That is, the geometry is assumed to be infinite in extent but repeating itself in the streamwise and/or spanwise directions *ad infinitum.* Several difficulties result from this type of approximation. First, periodicity strictly applies only to fully developed flows and should give an accurate approximation of the flow field only in regions far from the entrance, exit and side walls. This is not a problem for geometries in which the streamwise and spanwise extent is very large in comparison to the distance between channel walls. Second, the choice of a periodic wavelength necessarily excludes behavior associated with other wavelengths. Linear and weakly nonlinear stability theory considers the periodic wavelength of the disturbance as a free parameter. This allows selection of the wavelength in the solution process, but it does not allow for the influence of wavelengths larger than the selected periodicity to influence the stability. Third, periodicity assumes an ordered, repeating structure to the flow solution. In most cases experimental results show streamwise and spanwise variation of structures that are much less orderly than the results obtained from theory.

A third type of approximation used for theoretical studies is an assumed form of the solution. The truncated governing equations with approximate boundary conditions are solved by assuming a particular form of the solution. The spatial form of the solution is required, because of periodic boundary conditions, to be a wave. The temporal variation of the equations is assumed as well. Linear stability theory assumes a complex exponential variation of the solution in time, allowing wave behavior through the imaginary part of the exponent, and pure growth or decay through the real component. Weakly nonlinear theory results from modifying this assumption and creating an initial value problem for the temporal variation. However, in nonlinear theory, many *ad hoc* assumptions must be made as to the relative contribution of various terms in determining the temporal evolution of the perturbation.

The above approximations are the art and essence of using theoretical approaches; the computed solution is only as good as the approximations used in obtaining it. However, these approximations allow the standard mathematical tools of Fourier analysis, eigenvalue methods, and nonlinear dynamical systems analysis to be applied to the incompressible Navier-Stokes equations. They also allow parametric variation and study of general classes of flow solutions. Most of the advances in the understanding of instability and transition have resulted from the use of such methods in conjunction with experiments or numerical simulations.

1.3.2. Numerical Simulation of Spatially Developing Flows

The most natural approach for simulating an experimentally observed flow using a computational method is to attempt to match the experimental setup. Inflow and outflow regions are required, as well as side walls. The inflow condition must match as closely as possible the inflow in the experiment; the incoming flow will have certain velocity profile and disturbance characteristics. The outflow conditions must also be selected so that numerical difficulties are not encountered which would cause different behavior than that observed in the experiment. Typically, an idealized version of the experimental boundary conditions is used. The inlet profile is usually assumed to be a fully-developed channel flow, plus a disturbance. The disturbance is usually a traveling wave solution obtained from the linearized Navier-Stokes equations, or a combination of such solutions. Random disturbances have also been used. The outflow condition usually requires special treatment, such as modification of the governing equations in a *buffer domain* near the outflow, so that disturbances will travel smoothly out of the domain without reflection (Blodgett, 1995, Danabasoglu and Biringen, 1991).

The methodology for simulating instability in such flows is to first obtain a base flow, and then to perturb that base flow to determine its stability. The base flow is obtained by performing the simulation without the disturbance. A time-asymptotic state, usually steady, is obtained from the numerical simulation starting from some suitable initial condition. Then a second simulation is performed with the added disturbance. The effect of the disturbance on the base flow is obtained by subtracting the first solution from the second. The problem has the character of a boundary value problem for the disturbance, in that the disturbance is generated through an inflow boundary condition and is allowed to grow or decay spatially in the domain.

Using the spatial simulation method, the disturbances will be observed to grow or decay as they travel from the inflow to the outflow. If the base flow is unstable to the perturbation, the onset of three-dimensionality, quasi-periodicity, etc., will be observed in the spatial development of the flow. This is in marked contrast to the theoretical approach, in which the entire flow bifurcates to a new state when the previous state becomes unstable due to the global nature of the instability growth assumed through the periodicity condition. However, the spatial development can be related to the temporal bifurcation by realizing that the temporal approach describes the evolution of a single wave traveling downstream at the convective wave speed of the flow.

Though the spatial approach seems ideal, it is often impractical due to the requirement that the domain must be long enough to contain all of the desired development of the disturbance from its inflow value to its finite growth and possible bifurcation. However, certain features of the flow can be observed in spatial simulations that are not adequately described by the temporal approach. Solutions can exhibit less-ordered aperiodic structure observed in experiments. An example of this is the study of Guo and Finlay (1994) on spatially developing curved channel flow, in which Dean vortices are observed to slowly merge and split as they travel downstream, as seen in the experiments of Ligrani (1992), Finlay and Nandakumar (1990) and Ligrani and Niver (1988). Thus the Dean vortices are not strictly parallel to one another as is assumed in the temporal approach. These issues are addressed in Kleiser and Zang (1991), Blodgett (1995) and Danabasoglu and Biringen (1991).

1.3.3. Temporally Developing Flows

Though spatial simulations of channel flow instability are necessary for studying certain aspects of the transition process, temporal simulations are predominantly used. In the temporal numerical simulation method, the study proceeds much more closely with theory. Since theoretical approaches often assume periodic boundaries in space, the temporal numerical simulations can be used to provide a fully nonlinear solution for comparison with weakly nonlinear theories. The validity of the approximations (other than simplified boundary conditions) made in the theoretical approach are then revealed. Thus temporal numerical simulation is used more often than spatial simulation when investigating the nature of bifurcations and the transition scenario.

The temporal numerical simulation approach is quite different than that of the spatial approach due to the different role of the boundary and initial conditions. In the temporal approach, the disturbance is included with the base flow as the initial condition. The periodic boundary conditions insure that when this disturbance travels out of the domain, it re-enters through the inflow. The base flow is obtained as a time-asymptotic state with the same boundary conditions, with no disturbance. In the case of plane or curved channel flow, a fully-developed profile, either analytical or numerically approximated, may be used as the base flow. The perturbation, as well as the periodic wavelength, is obtained from the linearized Navier-Stokes equations. The temporal evolution of the disturbance is then investigated. If the base flow is unstable to the disturbance, the entire flow will bifurcate to a new stable flow or will breakdown in time and asymptote to a fully turbulent state. The solution method has the character of an initial value problem, with all of the dynamics of the flow determined by the nature of the initial conditions. See Kleiser and Zang (1991) for a thorough discussion.

The temporal approach has several significant advantages over using the spatial approach. The solution may be obtained with much less computational resources since the domain length is one wavelength of the disturbance. Therefore, more advanced stages of the transition process can be studied for flows, such as plane channel flow, in which fully turbulent flow will eventually occur. Another significant advantage is that the stability and bifurcation behavior can be thoroughly studied by varying the Reynolds number of the flow. The critical Reynolds number of the base flow can be determined by slowly increasing the Reynolds number until growth of the disturbance is observed. Subsequent bifurcations may be obtained by further increasing the Reynolds number. In this manner the critical Reynolds numbers and nature of the bifurcations can be observed. See Singer, Erlebacher and Zang (1992) and Guzmán and Amon (1994) for examples.

In summary, the mathematical tools used for understanding transition are usually framed in terms of temporal growth of disturbances in spatially periodic flows. Temporal simulation, therefore, closely mirrors the theoretical approach and places the results in the framework of bifurcation theory, or the theory of nonlinear dynamical systems.

1.4. Goals of this Study

As was discussed above, numerical simulation of the Navier-Stokes equations with periodic boundary conditions can be effectively used for investigating the stages of transition in general 2-D channel flows. It was also observed that the transition scenario for channel flows has application to understanding transition to turbulence in shear flows in general and to engineering applications in aerodynamics. The long term purpose of this research is to investigate the routes to turbulence in channel flows with the eventual application of explaining transition phenomena in more general flow configurations.

The specific purpose of this study is to develop a tool for investigating the stability of the incompressible flow in 2-D channels using a 3-D numerical simulation. In Section 2, the formulation of the equations governing flows in 2-D channels will be described, including the 3-D Navier-Stokes equations in general curvilinear coordinates, and the 2-D linearized Navier-Stokes equations for plane and curved channel flows, for use in linear stability theory. In Section 3, a spectral numerical simulation method will be described for solving the 3-D Navier-Stokes equations. The methods for using the results of linear stability theory to obtain the initial condition, and the extraction of stability information from the computed results are also discussed. In Section 4, the development and validation of a computer code for simulating 2-D flow in plane and curved channels is described along with the flow results for these two geometries. The results primarily validate the simulation methodology, but they also show some of the interesting effects of nonlinearity in the early stages of transition. Particularly, a finite-amplitude equilibrium state is computed for plane channel flow at a subcritical Reynolds number. Section 5 contains conclusions and recommendations for further study.

Section 2. Mathematical Formulation

The incompressible Navier-Stokes equations describe the flow of a liquid or a low-speed gas which is homogeneous and Newtonian. Also, it is assumed that viscosity is constant, or equivalently, that temperature gradients in the flow are negligible and do not need to be computed or considered to affect the viscosity. The incompressible Navier-Stokes equations consist of the conservation of linear momentum, which is the application of Newton's second law to an infinitesimal fluid volume, and the conservation of mass, or the continuity equation.

The Navier-Stokes equations are formulated in terms of general curvilinear coordinates, with application to a general 2-D channel, in §2.1. The simplified forms of the Navier-Stokes equations for plane and curved channel flow are also given. In §2.2, the linear stability equations are derived for the plane and curved channel by linearizing the Navier-Stokes equations about a base state and applying a Fourier mode disturbance. The numerical aspects of solving these equations and using them for the study of instabilities in channel flows is reserved for Section 3.

2.1. Governing Equations and Base Flow Solutions

The Navier-Stokes equations in vector form are deceptively simple. This section applies these equations to a general 2-D channel geometry, which requires a general curvilinear coordinate transformation in the plane of the streamwise and wall-normal directions. The channel is assumed to be infinite with no curvature in the spanwise direction, thus allowing a simple linear transformation. The purpose of the transformations is to map the geometry onto a computational box which can be used to solve the flow in any 2-D channel geometry. The computational domain will be further discussed in the numerical formulation of Section 3.

In addition, it is necessary to derive the Navier-Stokes equations for the specific cases of the plane channel, and the constant curvature channel (called a curved channel), so that the linearized stability equations for these cases can be derived in §2.2. These two special cases have analytical solutions which are used in the stability analysis and in the initial condition for the numerical simulation. These solutions are also derived in this section.

2.1.1. Vector Form of Incompressible Time-Dependent Navier-Stokes Equations

The non-dimensional time-dependent Navier-Stokes equations governing the incompressible flow of a homogeneous fluid are:

$$\begin{aligned} \frac{\partial}{\partial t}\boldsymbol{u}+\nabla\cdot(\boldsymbol{u}\boldsymbol{u}) &= -\nabla\tilde{p}+\frac{1}{Re}\nabla^2\boldsymbol{u}+\boldsymbol{Q} \\ \nabla\cdot\,\boldsymbol{u} &= 0 \end{aligned} \qquad \textbf{(2.1)}$$

where, lengths are non-dimensionalized by an appropriate reference value L_r, the velocity, $\boldsymbol{u}$, is non-dimensionalized by the reference velocity U_r, and the pressure , $\tilde{p}$, is non-dimensionalized by U_r^2. The density of the fluid is constant and has been non-dimensionalized by the reference value ρ_r so that $\rho = 1$. The Reynolds number, Re, is $\rho_r U_r L_r / \mu$, where μ is the dimensional viscosity of the fluid. The vector $\boldsymbol{Q}$ is reserved for use as a source term for forcing the solution during the validation phase of the study.

The domain of interest is the region between two walls infinite in span. The domain is defined in terms of the computational coordinates ξ^i, I=1,2,3.

- Streamwise direction: $\xi^1 \in [0, 2\pi]$
- Spanwise direction: $\xi^2 \in [0, 2\pi]$
- Wall-normal direction: $\xi^3 \in [-1, 1]$

The boundary conditions for channel flow problems are periodic in two directions:

$$\begin{gathered}
\boldsymbol{u}(\xi^1,\xi^2,\xi^3) = \boldsymbol{u}(\xi^1+2\pi,\xi^2,\xi^3) = u(\xi^1,\xi^2+2\pi,\xi^3) \\
\tilde{p}(\xi^1,\xi^2,\xi^3) = \tilde{p}(\xi^1+2\pi,\xi^2,\xi^3) + const = \tilde{p}(\xi^1,\xi^2+2\pi,\xi^3) \\
\boldsymbol{u}(\xi^1,\xi^2,-1) = \boldsymbol{u}_{lower\ wall} \\
\boldsymbol{u}(\xi^1,\xi^2,1) = \boldsymbol{u}_{upper\ wall}
\end{gathered} \qquad \textbf{(2.2)}$$

Note that pressure is required to have a net pressure gradient in the streamwise direction to allow a net flux of mass in the streamwise direction to occur. Therefore, a known constant pressure gradient is imposed, and the pressure is split into a known non-periodic component, P, which forces the flow in the streamwise direction, and a component, p, which is periodic in ξ^1. Note that P is chosen so that its gradient is constant in ξ^1. Also note that no wall boundary conditions are needed for pressure. Finally, since the pressure appears only in terms of its gradient, an additional, arbitrary, condition is required. In this study, the condition that is specified on pressure is that the mean pressure in the domain is zero. These conditions are expressed mathematically as:

$$\begin{aligned} \tilde{p} &= P + p \\ \nabla P \cdot \vec{e}_1 &= const \\ \iiint_D p \, dV &= 0 \end{aligned} \tag{2.3}$$

2.1.2. Generalized Curvilinear Coordinates

A generalized two-dimensional transformation is used to map the physical domain, given by Cartesian coordinates x^i, into the computational domain, given by computational coordinates ξ^i. Use is made of an intermediate coordinate system given by η^i, which is related linearly to the computational coordinate system. The domain of each coordinate is:

$$\begin{aligned} & x^i \in [x^i_{\min} \, , \, x^i_{\min} + L_{x^i}] \quad \text{for } i=\{1,2,3\} \\ & \eta^i \in [\eta^i_{\min} \, , \, \eta^i_{\min} + L_{\eta^i}] \quad \text{for } i=\{1,2,3\} \\ & \xi^1 \in [0 \, , \, 2\pi] \\ & \xi^2 \in [0 \, , \, 2\pi] \\ & \xi^3 \in [-1 \, , \, 1] \end{aligned} \tag{2.4}$$

The first transformation, T_1, relates x^i to η^i and is given analytically by:

$$T_1 : \left\{ \begin{array}{c} \eta^1 = \eta^1(x^1, x^3) \\ \eta^2 - \eta^2_{\min} = \dfrac{L_{\eta^2}}{L_{x^2}} (x^2 - x^2_{\min}) \\ \eta^3 = \eta^3(x^1, x^3) \end{array} \right\} \tag{2.5}$$

where the spanwise computational coordinate is an arbitrary linear scaling of the Cartesian coordinate x^2. The linear transformation T_2 then relates η^i to ξ^i:

$$T_2 : \left\{ \begin{aligned} \xi^1 &= \frac{2\pi}{L_{\eta^1}} (\eta^1 - \eta^1_{\min}) \\ \xi^2 &= \frac{2\pi}{L_{\eta^2}} (\eta^2 - \eta^2_{\min}) \\ \xi^3 + 1 &= \frac{2}{L_{\eta^3}} (\eta^3 - \eta^3_{\min}) \end{aligned} \right\} \tag{2.6}$$

Covariant and contravariant base vectors are defined, respectively, in terms of the above transformations:

$$\vec{e}_i = \frac{\partial x^j}{\partial \xi^i} \hat{e}_j \qquad \vec{e}^{\,i} = \frac{\partial \xi^i}{\partial x^j} \hat{e}_j \tag{2.7}$$

where $\hat{e}_i$ represents the Cartesian unit basis $\{\vec{i},\vec{j},\vec{k}\}$ for i={1,2,3}, respectively. The Cartesian base vectors can also be expressed in terms of covariant and contravariant base vectors:

$$\hat{e}_j = \frac{\partial \xi^i}{\partial x^j} \quad , \quad \vec{e}_i = \frac{\partial x^j}{\partial \xi^i} \vec{e}^{\,i} \tag{2.8}$$

Summation notation will be used consistently in this document unless otherwise noted. The covariant and contravariant metric tensors are defined in terms of the base vectors:

$$
\begin{gathered}
g_{ij} = \vec{e}_i \cdot \vec{e}_j \qquad g^{ij} = \vec{e}^{\,i} \cdot \vec{e}^{\,j} \\
g^{i}{}_{j} = \vec{e}^{\,i} \cdot \vec{e}_j = \delta_{ij} \qquad g_i{}^{j} = \vec{e}_i \cdot \vec{e}^{\,j} = \delta_{ij} \\
\text{matrix } \{g_{ij}\} = \left[\text{matrix } \{g^{ij}\}\right]^{-1}
\end{gathered}
\tag{2.9}
$$

The Jacobian of the transformation,

$$
J = \frac{\partial(x^1,x^2,x^3)}{\partial(\xi^1,\xi^2,\xi^3)} \tag{2.10}
$$

is related to the determinate of the covariant metric tensor $g = \det\{g_{\mathrm{ij}}\} = J^2$. The scaling of the volume of curvlinear space relative to Cartesian space is given by $\sqrt{g} = |J|$.

A vector field such as the velocity field $\boldsymbol{u}(\xi^1,\xi^2,\xi^3)$ has several representations in the general coordinate system:

$$
\begin{aligned}
\boldsymbol{u} &= \hat{u}^{\,i}\ \hat{e}_i && \text{Cartesian} \\
\boldsymbol{u} &= u^{i}\ \vec{e}_i && \text{Contravariant} \\
\boldsymbol{u} &= u_i\ \vec{e}^{\,i} && \text{Covariant}
\end{aligned}
\tag{2.11}
$$

Christoffel symbols arise when derivatives of base vectors are required:

$$\frac{\partial}{\partial \xi^i}\vec{e}_j = \frac{\partial}{\partial \xi^i}\frac{\partial x^k}{\partial \xi^j}\hat{e}_k = \frac{\partial^2 x^k}{\partial \xi^i \partial \xi^j}\frac{\partial x^k}{\partial \xi^l} g^{lm}\vec{e}_m = \Gamma^m_{ij}\vec{e}_m$$

$$\text{where } \Gamma^m_{ij} = g^{lm}\frac{\partial^2 x^k}{\partial \xi^i \partial \xi^j}\frac{\partial x^k}{\partial \xi^l}$$

$$\frac{\partial^2}{\partial \xi^i \partial \xi^j}\vec{e}_k = \frac{\partial}{\partial \xi^i}\left(\Gamma^m_{jk}\vec{e}_m\right) = \left(\frac{\partial}{\partial \xi^i}\Gamma^m_{jk}\right)\vec{e}_m + \Gamma^m_{jk}\frac{\partial}{\partial \xi^i}\vec{e}_m = \Lambda^m_{ijk}\vec{e}_m \tag{2.12}$$

$$\text{where } \Lambda^m_{ijk} = \frac{\partial}{\partial \xi^i}\Gamma^m_{jk} + \Gamma^l_{jk}\Gamma^m_{il}$$

where Γ^m_{ij} is a Christoffel symbol of the second kind, and is symmetric with respect to *i* and *j*. Second derivatives of base vectors are also required. The symbols Λ^m_{ijk} are also symmetric with respect to *i* and *j*.

2.1.3. Contravariant Form of Navier-Stokes Equations

To apply the generalized coordinate system to the governing equations Eq. (2.1), the following differential operators are needed:

$$\begin{pmatrix} \nabla \\ \nabla\cdot \\ \nabla\times \end{pmatrix} A \equiv \lim_{\partial V \to 0} \iint_{\partial S} \begin{pmatrix} \vec{n} \\ \vec{n}\cdot \\ \vec{n}\times \end{pmatrix} A dS$$

$$= \frac{1}{\sqrt{g}}\frac{\partial}{\partial \xi^i}\left[\sqrt{g}\begin{pmatrix} \vec{e}^{\,i} \\ \vec{e}^{\,i}\cdot \\ \vec{e}^{\,i}\times \end{pmatrix} A\right] \qquad \text{conservative form} \tag{2.13}$$

$$= \begin{pmatrix} \vec{e}^{\,i} \\ \vec{e}^{\,i}\cdot \\ \vec{e}^{\,i}\times \end{pmatrix}\frac{\partial}{\partial \xi^i}A \qquad \text{non-conservative form}$$

where in the case of the gradient, **A** is an arbitrary scalar, vector, or tensor, and in the divergence and curl is an arbitrary vector or tensor. Applying the general coordinate transformation to Eq. (2.1) along with the pressure splitting from Eq. (2.3) yields:

$$\frac{\partial}{\partial t}\boldsymbol{u} + \frac{1}{\sqrt{g}}\frac{\partial}{\partial \xi^j}\left(\sqrt{g}u^i\boldsymbol{u}\right) = -\vec{e}^{\,m}\frac{\partial}{\partial \xi^m}p - \vec{e}^{\,m}\frac{\partial P}{\partial \xi^m} + \frac{1}{Re}\frac{1}{\sqrt{g}}\frac{\partial}{\partial \xi^i}\left(\sqrt{g}g^{ij}\frac{\partial}{\partial \xi^j}\boldsymbol{u}\right) + \boldsymbol{Q} \qquad \textbf{(2.14)}$$

for the momentum equation. In order to place the vector momentum equation into a form in which it can be solved, it must be separated into a system of scalar equations. The vector ***u*** must be replaced by its contravariant components, and the derivatives of base vectors must be expanded in terms of Christoffel symbols. The contravariant components of the momentum equation become:

$$\text{Momentum}\cdot\vec{e}^{\,m} \rightarrow$$

$$\begin{aligned}\frac{\partial}{\partial t}u^m + \frac{1}{\sqrt{g}}\frac{\partial}{\partial \xi^i}\left(\sqrt{g}u^i u^m\right) + u^i u^j \Gamma^m_{ij} = -g^{im}\frac{\partial p}{\partial \xi^i} - g^{im}\frac{\partial P}{\partial \xi^i} + \\ \frac{1}{Re}\left[\frac{1}{\sqrt{g}}\frac{\partial}{\partial \xi^i}\left(\sqrt{g}g^{ij}\frac{\partial u^m}{\partial \xi^j}\right) + \frac{1}{\sqrt{g}}\frac{\partial}{\partial \xi^i}\left(\sqrt{g}g^{ij}u^k\right)\Gamma^m_{jk} + g^{ij}\frac{\partial u^k}{\partial \xi^j}\Gamma^m_{jk} + g^{ij}u^k\Lambda^m_{ijk}\right] + Q^m\end{aligned} \qquad \textbf{(2.15)}$$

for *m*=1,2,3. The continuity equation in terms of contravariant velocities is:

$$\frac{1}{\sqrt{g}}\frac{\partial}{\partial \xi^i}\left(\sqrt{g}u^i\right) = 0 \qquad \textbf{(2.16)}$$

2.1.4. Plane Channel Geometry

The plane channel geometry is obtained using a Cartesian coordinate system, that is, the intermediate coordinate system is identified with Cartesian coordinates, $\eta^i = x^i$ for

$i=\{1,2,3\}$. The Cartesian coordinates are non-dimensionalized by the channel half-height h. Thus the transformation between computational coordinates and Cartesian coordinates is given by:

$$T_{1,2} : \left\{ \begin{aligned} \xi^1 &= \frac{2\pi}{L_{x^1}} x^1 \\ \xi^2 &= \frac{2\pi}{L_{x^2}} x^2 \\ \xi^3 &= 2\,x^3 + 1 \end{aligned} \right\} \qquad \textbf{(2.17)}$$

for a Cartesian domain:

$$\begin{aligned} &x^1 \in [0\ ,\ L_{x^1}] \\ &x^2 \in [0\ ,\ L_{x^2}] \\ &x^3 \in [-1\ ,\ 1] \end{aligned} \qquad \textbf{(2.18)}$$

The reference velocity for the plane channel flow is taken to be the maximum base flow velocity, U_{max}. Thus the Reynolds number is $Re = \rho_r U_{\max} h / \mu$.

The metrics are easily determined from the above transformation. All of the metrics and base vectors are constant and the derivatives of base vectors are zero. Substituting these metrics into Eqs. (2.14) and (2.16) yields the contravariant momentum and continuity equations for the plane channel geometry in terms of the generalized coordinates ξ^i. Also of interest are the governing equation formulated in terms of the original Cartesian coordinates x^i. These equations are used to determine analytical solutions of the equations and to formulate the linear stability equations in the next section. The Cartesian governing equations are:

$$\frac{\partial}{\partial t}\hat{u}^m + \frac{\partial}{\partial x^i}\hat{u}^i\hat{u}^m = -\frac{\partial}{\partial x^m}p - \delta_{1m}\frac{dP}{dx^1} + \frac{1}{Re}\frac{\partial}{\partial x^i}\frac{\partial}{\partial x^i}\hat{u}^m + \hat{Q}^m$$

$$\frac{\partial}{\partial x^i}\hat{u}^i = 0 \tag{2.19}$$

The above system of equations with domain given by Eq. (2.18) has an analytical solution for flow in the streamwise direction with no-slip walls:

$$\boldsymbol{u} = U(x^3)\hat{e}_1 = (1-(x^3)^2)\hat{e}_1$$

$$\frac{dP}{dx^1} = -\frac{2}{Re} \tag{2.20}$$

2.1.5. Curved Channel Geometry

To obtain the curved channel geometry, a polar coordinate system is used. The intermediate coordinate system η^i is identified with polar coordinates, $\{\eta^1{=}\theta, \eta^2{=}y, \eta^3{=}r\}$, with domain

$$\begin{aligned} \theta &\in [\theta_{\min}\ ,\ \theta_{\min}+L_\theta] \\ y &\in [0\ ,\ L_y] \\ r &\in [R_c-1\ ,\ R_c+1] \end{aligned} \tag{2.21}$$

where R_c is the mean radius of curvature of the channel. Again all lengths are non-dimensionalized by the channel half-height h. The standard transformation between polar coordinates and Cartesian coordinates is:

$$T_1 = \left\{ \begin{array}{c} \theta = \tan^{-1}\left(\dfrac{x^3}{x^1} \right) \\ y = x^2 \\ r = \sqrt{(x^1)^2 + (x^3)^2} \end{array} \right\} \quad T_1^{-1} = \left\{ \begin{array}{c} x^1 = r\cos(\theta) \\ x^2 = y \\ x^3 = r\sin(\theta) \end{array} \right\} \qquad \textbf{(2.22)}$$

along with its inverse. The transformation between computational coordinates and polar coordinates is a linear transformation:

$$T_2 = \left\{ \begin{array}{c} \xi^1 = \dfrac{2\pi}{L_\theta}(\theta - \theta_{\min}) \\ \xi^2 = \dfrac{2\pi}{L_y} y \\ \xi^3 = r - R_c \end{array} \right\} \qquad \textbf{(2.23)}$$

The metrics relating computational coordinates to Cartesian coordinates are determined from transformations T_1 and T_2. Note that by using the standard polar coordinate system the direction of increasing ξ^1 is from right to left (for θ in the first two quadrants). For the results shown in this study, the orientation of the plots is reversed so that ξ^1 increases from left to right.

In addition to the governing equations in terms of computational coordinates and contravariant velocities, the equations for curved channel flow in polar coordinates are needed. For this purpose, an alternate representation of the velocity vector is used:

$$
\begin{gathered}
\boldsymbol{u} = u^{\theta}\hat{e}_{\theta} + u^{y}\hat{e}_{y} + u^{r}\hat{e}_{r} \\
\text{where} \quad
\begin{aligned}
\hat{e}_{\theta} &= \vec{e}_1 / |\vec{e}_1| \\
\hat{e}_{y} &= \vec{e}_2 / |\vec{e}_2| \\
\hat{e}_{r} &= \vec{e}_3 / |\vec{e}_3|
\end{aligned} \\
\text{therefore} \quad
\begin{aligned}
u^{\theta} &= u^{1} / \sqrt{g^{11}} \\
u^{y} &= u^{2} / \sqrt{g^{22}} \\
u^{r} &= u^{3} / \sqrt{g^{33}}
\end{aligned}
\end{gathered}
\tag{2.24}
$$

These are the polar velocity components typically used in the literature and are simply a scaling of the contravariant components. The polar momentum equations are obtained by taking the dot product of the vector momentum equation, Eq. (2.1), with each of the polar unit base vectors $\{\hat{e}_{\theta}, \hat{e}_{y}, \hat{e}_{r}\}$. The resulting momentum equations are

$$
\begin{gathered}
\frac{\partial}{\partial t}u^{\theta} + u^{r}\frac{\partial u^{\theta}}{\partial r} + \frac{u^{\theta}}{r}\frac{\partial u^{\theta}}{\partial \theta} + u^{y}\frac{\partial u^{\theta}}{\partial y} - \frac{u^{\theta}u^{r}}{r} = -\frac{1}{r}\frac{\partial p}{\partial \theta} - \frac{1}{r}\frac{dP}{d\theta} + \\
\frac{1}{Re}\left[\frac{\partial^2 u^{\theta}}{\partial r^2} + \frac{1}{r}\frac{\partial u^{\theta}}{\partial r} + \frac{1}{r^2}\frac{\partial^2 u^{\theta}}{\partial \theta^2} + \frac{\partial^2 u^{\theta}}{\partial y^2} + \frac{2}{r^2}\frac{\partial u^{r}}{\partial \theta} - \frac{u^{\theta}}{r^2}\right] + Q^{\theta} \\
\frac{\partial}{\partial t}u^{r} + u^{r}\frac{\partial u^{r}}{\partial r} + \frac{u^{\theta}}{r}\frac{\partial u^{r}}{\partial \theta} + u^{y}\frac{\partial u^{r}}{\partial y} - \frac{u^{\theta 2}}{r} = -\frac{\partial p}{\partial r} + \\
\frac{1}{Re}\left[\frac{\partial^2 u^{r}}{\partial r^2} + \frac{1}{r}\frac{\partial u^{r}}{\partial r} + \frac{1}{r^2}\frac{\partial^2 u^{r}}{\partial \theta^2} + \frac{\partial^2 u^{r}}{\partial y^2} - \frac{u^{r}}{r^2} - \frac{2}{r^2}\frac{\partial u^{\theta}}{\partial \theta}\right] + Q^{r} \\
\frac{\partial}{\partial t}u^{y} + u^{r}\frac{\partial u^{y}}{\partial r} + \frac{u^{\theta}}{r}\frac{\partial u^{y}}{\partial \theta} + u^{y}\frac{\partial u^{y}}{\partial y} = -\frac{\partial p}{\partial y} + \\
\frac{1}{Re}\left[\frac{\partial^2 u^{y}}{\partial r^2} + \frac{1}{r}\frac{\partial u^{y}}{\partial r} + \frac{1}{r^2}\frac{\partial^2 u^{y}}{\partial \theta^2} + \frac{\partial^2 u^{y}}{\partial y^2}\right] + Q^{y}
\end{gathered}
\tag{2.25}
$$

and the continuity equation is

$$\frac{1}{r}\frac{\partial u^{\theta}}{\partial \theta} + \frac{1}{r}\frac{\partial}{\partial r}\left(r u^{r} \right) + \frac{\partial u^{y}}{\partial y} = 0 \tag{2.26}$$

The above system of equations has an analytical solution for flow in the streamwise direction with no-slip walls:

$$\boldsymbol{u} = U^{\theta}(r)\hat{e}_{\theta} = Dr\left[\ln r + C + E\frac{1}{r^{2}} \right]\hat{e}_{\theta}$$

$$\frac{\partial P}{d\theta} = -\frac{2D}{Re}$$

$$\frac{\partial P}{dr} = \frac{(U^{\theta})^{2}}{r}$$

$$C = \frac{R_i^2}{4R_c}\ln\eta + \ln R_o \qquad\qquad R_i = R_c - 1 \tag{2.27}$$

where

$$E = -R_i^2\frac{R_o^2}{4R_c}\ln\eta \qquad \text{and} \qquad R_o = R_c + 1$$

$$D = \frac{-2}{R_c + E\ln\eta} \qquad\qquad \eta = \frac{R_i}{R_o}$$

See Singer, Erlebacher and Zang (1992). To be consistent with the literature, the reference velocity for curved channel flow is taken to be the mean base flow velocity,

$$U_{ref} \equiv \overline{U}^{\theta} = \frac{1}{2}\int_{R_c-1}^{R_c+1} U^{\theta}(r)\,dr \tag{2.28}$$

Thus the Reynolds number is $Re = \rho_r \overline{U}^{\theta} h/\mu$.

2.1.6. Forcing Function Analysis

The purpose of the forcing function $\boldsymbol{Q}$ is described in this section. Since few analytical solutions of the Navier Stokes equations are known, it is helpful for purposes of code validation to provide an analytical solution and require that it be a solution to the governing equations by choosing a suitable forcing function. In general, this can be done by prescribing the velocity vector $\boldsymbol{u}=\boldsymbol{U}_{test}$ in any coordinate system, along with the pressure $\tilde{p} = P_{test}$. In this study, only divergence-free test solutions $\boldsymbol{U}_{test}$ were selected. After substituting the test solution into the momentum equation, the forcing function vector $\boldsymbol{Q}$ is chosen to be the residual of the equation. In vector form, this can be written as:

$$\boldsymbol{Q} = \frac{\partial}{\partial t}\boldsymbol{u} + \nabla\cdot(\boldsymbol{u}\boldsymbol{u}) + \nabla\tilde{p} - \frac{1}{Re}\nabla^2\boldsymbol{u} \qquad \textbf{(2.29)}$$

In this study, the analytical test solution was substituted into either the Cartesian momentum equations, Eq. (2.19), or the polar momentum equations, Eq. (2.25). The forcing function $\boldsymbol{Q}$ was evaluated symbolically using *Mathematica* software (Wolfram, 1991) and stored within the code. During the simulation, the forcing function vector $\boldsymbol{Q}$, is a known function of space and time. Adding this term does not change the nature of the Navier-Stokes equations as a system of differential equations.

2.2. Linear Stability Theory

The linear stability equations for plane and curved channel flows are obtained using both the Navier-Stokes equations linearized about some known base flow, and a given form for disturbances about that base flow. An abbreviated description of linear stability theory for plane and channel flows, along with the derivation of the stability equations and the Orr-Sommerfeld equation are described below. For more complete details, refer to Drazin and Reid (1981).

2.2.1. General Parallel Flow Formulation

Linear stability analysis is based upon a series of assumptions and approximations about perturbations to some known solution of the governing equations. The known solution is the *base flow* or *basic state*, $\boldsymbol{u}=\boldsymbol{U}_b$ and $p=P_b$. The stability of this base flow to periodic wave disturbances in a given direction ξ^{wave}, or ξ^{w}, is investigated. In this study, ξ^{w} may be either ξ^1, or ξ^2, but not ξ^3 since the walls at $\xi^3 = -1$ and 1 prohibit a periodic solution. The base flow is assumed to be parallel in the wave direction, that is $\partial/\partial\xi^{w}\boldsymbol{U}_b = \partial/\partial\xi^{w}P_b = 0$ in the derivation of the following stability equations. Given a basic state and wave direction, the following steps lead to linear stability results.

First, a perturbation is applied to the basic state. For an infinitely small perturbation, the temporal variation may be assumed to be complex exponential in time with both the velocity vector and pressure having the same temporal variation. The perturbation is assumed to be periodic in the ξ^{w}-direction with wavelength $\lambda = 2\pi/\alpha$ where α is the wavenumber, assumed to be real in this study. This puts the perturbation in the form:

$$\boldsymbol{u} = \boldsymbol{U}_b + \boldsymbol{u}'$$

$$p = P_b + p'$$

$$\boldsymbol{u}' = \sum_{k=-\infty}^{\infty} \mathrm{Real}\left\{ \tilde{\boldsymbol{u}}_k(\xi^3)\ e^{\mathrm{i}(k\alpha\xi^{w}-\omega t)} \right\} \qquad \textbf{(2.30)}$$

$$p' = \sum_{k=-\infty}^{\infty} \mathrm{Real}\left\{ \tilde{p}_k(\xi^3)\ e^{\mathrm{i}(k\alpha\xi^{w}-\omega t)} \right\}$$

where $\tilde{\boldsymbol{u}}_k(\xi^3)$ and $\tilde{p}_k(\xi^3)$ are the complex mode shapes. The above substitutions are made into the governing equations. Since the base flow is known to be a solution to the governing equations, the governing equations with the base flow substituted are subtracted from the perturbed equation. The equations are then linearized, i.e., any term quadratic in perturbation quantities (which are assumed infinitely small) is neglected.

The linear stability equations are obtained analytically by taking derivatives with respect to time and ξ^w. Since the equations are linear, each mode of the Fourier series may be considered independently. Typically, the Fourier mode number, *k*, is dropped in the development of the linear stability equations. Actually, it is just absorbed into α. The system of linear differential equations with prescribed boundary conditions only has a solution for certain combinations of the various parameters in the equations, namely the Reynolds number *Re,* spatial wavenumber α (actually $k\alpha$) and complex temporal growth rate ω. In this study, the Reynolds number and spatial wavenumber are prescribed. The unknown parameter, the complex temporal growth rate, can then be determined as an eigenvalue of the system of differential equations. The eigensolution corresponding to a particular eigenvalue consists of the mode shapes $\tilde{\boldsymbol{u}}$ and $\tilde{p}$. The linear stability equations for streamwise disturbances in plane and curved channel flow are given in the following two sections.

2.2.2. Plane Channel Flow Stability Equations

The stability equations for plane channel flow are obtained from the Cartesian Navier-Stokes equations Eq. (2.19) with base flow given by Eq. (2.20). In this study, the perturbation is assumed to be two-dimensional. To investigate the streamwise instability of the base flow to two-dimensional disturbances, a perturbation of the form

$$\tilde{\boldsymbol{u}} = \tilde{u}^i \hat{e}_i$$
$$\boldsymbol{u}' = \tilde{u}^i(x^3)\mathrm{e}^{\mathrm{i}(\alpha x^1 - \omega t)}\hat{e}_i \tag{2.31}$$

is assumed, where Cartesian components of the velocity mode vector are used. The plane channel linear stability equations are obtained by substituting Eqs. (2.31) and (2.30) into the Cartesian Navier-Stokes equations, Eq. (2.19), and assuming the base flow to be the analytical solution Eq. (2.20). The following system of linear ordinary differential equations is obtained:

$$\left[\frac{1}{Re}(D^2-\alpha^2)+\mathrm{i}(\omega-\alpha U_b)\right]\tilde{u}^1 - \frac{dU_b}{dx^3}\tilde{u}^3 - \mathrm{i}\alpha\tilde{p} = 0$$
$$\left[\frac{1}{Re}(D^2-\alpha^2)+\mathrm{i}(\omega-\alpha U_b)\right]\tilde{u}^3 - D\tilde{p} = 0 \tag{2.32}$$
$$\mathrm{i}\alpha\tilde{u}^1 + D\tilde{u}^3 = 0$$

where D represents the differential operator d/dx^3. The three equations can be combined into a single fourth-order ordinary differential equation by eliminating the streamwise velocity component and the pressure. The resulting equation is called the Orr-Sommerfeld equation:

$$\left[\left((D^2-\alpha^2)+\mathrm{i}Re(\omega-\alpha U_b)\right)(D^2-\alpha^2)+\mathrm{i}Re\,\alpha\frac{d^2U_b}{(dx^3)^2}\right]\tilde{u}^3 = 0$$

or **(2.33)**

$$\left[D^4+\left(\mathrm{i}Re(\omega-\alpha U_b)-2\alpha^2\right)D^2+\alpha^2\left(\alpha^2-\mathrm{i}Re(\omega-\alpha U_b)\right)+\mathrm{i}Re\,\alpha\frac{d^2U_b}{(dx^3)^2}\right]\tilde{u}^3 = 0$$

2.2.3. Curved Channel Flow Stability Equations

The stability equations for curved channel flow are obtained in a similar manner. The polar Navier-Stokes equations Eqs. (2.25) and (2.26) are used with the base flow given by Eq. (2.27). To investigate the instability of the base flow to streamwise two-dimensional disturbances, a perturbation of the form:

$$\boldsymbol{u}' = \tilde{u}^{\theta}(r)\,\mathrm{e}^{\mathrm{i}(\alpha\theta-\omega t)}\hat{e}_{\theta} + \tilde{u}^{r}(r)\,\mathrm{e}^{\mathrm{i}(\alpha\theta-\omega t)}\hat{e}_{r} \tag{2.34}$$

is assumed for each Fourier mode. The curved channel linear stability equations are:

$$\begin{gathered}
\left[\frac{1}{Re}(r^2\mathcal{L}-1)+\mathrm{i}r(r\omega-\alpha U_b)\right]\tilde{u}^{\theta} + \left[\frac{1}{Re}2\mathrm{i}\alpha - r^2\frac{dU_b}{dr} - rU_b\right]\tilde{u}^{r} - \mathrm{i}r\alpha\tilde{p} = 0 \\
\left[-\frac{1}{Re}2\mathrm{i}\alpha + 2rU_b\right]\tilde{u}^{\theta} + \left[\frac{1}{Re}(r^2\mathcal{L}-1)+\mathrm{i}r(r\omega-\alpha U_b)\right]\tilde{u}^{r} - r^2 D\tilde{p} = 0 \\
\mathrm{i}\alpha\tilde{u}^{\theta} + D(r\tilde{u}^{r}) = 0 \\
\text{where}\quad \mathcal{L} = D^2 + \frac{1}{r}D - \frac{\alpha^2}{r^2}
\end{gathered} \tag{2.35}$$

where D represents the differential operator *d/dr.* Again, the three equations can be combined into a single fourth-order ordinary differential equation by eliminating the streamwise velocity component and the pressure. The resulting equation is the curved channel Orr-Sommerfeld equation::

$$\left[a_4 D^4 + a_3 D^3 + a_2 D^2 + a_1 D + a_0\right] \tilde{u}^r = 0$$

where

$$\begin{aligned} a_4 &= r^4 \\ a_3 &= 6r^3 \\ a_2 &= 5r^2 - 2\alpha^2 r^2 + \mathrm{i}Re\omega r^4 - \mathrm{i}Re\alpha r^3 U_b \\ a_1 &= -r - 2\alpha^2 r + 3\mathrm{i}Re\omega r^3 - 3\mathrm{i}Re\alpha r^2 U_b \end{aligned} \tag{2.36}$$

$$\begin{aligned} a_0 = {} & 1 - 2\alpha^2 + \alpha^4 + \mathrm{i}Re\omega r^2 - \mathrm{i}Re\alpha^2\omega r^2 - 2\mathrm{i}Re\alpha r U_b + \\ & \mathrm{i}Re\alpha^3 r U_b + \mathrm{i}Re\alpha r^2 \frac{dU_b}{dr} + \mathrm{i}Re\alpha r^3 \frac{d^2U_b}{dr^2} \end{aligned}$$

See Singer, Erlebacher and Zang (1992) for a similar derivation. However, in their study, the nonlinear evolution equations are derived, of which the linear disturbance equation is a subset.

2.3. Summary

In §2.1, the 3-D Navier-Stokes equations were formulated for the geometry of interest, that is a general 2-D channel. At this point, the equations and all boundary conditions are prescribed with the exception of the initial condition. The initial condition will be obtained using the linear stability theory of §2.2. The numerical methodology for employing this initial condition and for temporal numerical simulation of the Navier-Stokes equations on a discrete set of points is given in the next chapter.

Section 3. Numerical Approach

The numerical simulation of stability and transition in channel flows is accomplished by solving the continuum governing equations described in Section 2 using numerical methods. Although any valid numerical method for solving time-dependent partial differential equations can be used, *spectral* methods are most commonly used for solving spatially periodic stability problems. The standard text on spectral methods is that of Canuto *et al.* (1988) and is the source of the information in this section relating to spectral methods. A detailed example of the use of spectral methods for solving the Navier-Stokes equations is given in Zang and Hussaini (1985b). The spectral discretization used in periodic stability problems employs Fourier decomposition in the periodic directions, thus providing solutions which are periodic to the Nth derivative, where $N+1$ is the number of Fourier modes used. The Fourier method is also well-matched to the temporal simulation problem since the solutions obtained from linear stability theory which are used to create the initial condition for numerical simulation, are Fourier modes in the streamwise and/or spanwise directions. Errors in the solution obtained with a Fourier method can always be expressed in terms of the omitted high frequency modes $|n| > N/2$. Therefore low mode-number waves can be resolved exactly.

In the non-periodic (wall-normal, or ξ^3) direction, a Fourier method cannot be used. Instead, the solution is represented in terms of orthogonal *Chebyshev* polynomials, and the grid points are selected using Gaussian quadrature. Though this method is more computationally intensive per grid point (or Chebyshev mode) then, for example, the finite difference method, the greater accuracy of the solution allows the use of fewer points than other methods. The basic development of the Fourier and Chebyshev spectral methods are described in §3.1. The methods are then applied to the governing equations in §3.2.

The discretization in time is performed with a standard second-order finite difference scheme. The development of the temporal discretization and the iterative matrix method used to solve the discrete system of governing equations at each time step are described in §3.3. The remaining two sections of this chapter, §§3.4 and 3.5, respectively, describe the generation of the initial flow solution using linear stability theory and the extraction of mode information from the computed solution for comparison with stability theory.

3.1. Spectral Methods

The problem of numerical approximation to a continuum system of differential equations can be approached from many different perspectives. One consistent methodology is to formulate a discrete *basis* to represent the spatial variation of the solution. In spectral methods, the discrete basis used to represent the solution in one direction is obtained from a singular Sturm-Liouville problem with appropriate boundary conditions. The Fourier system is one such basis, and can be used to expand periodic functions. Other bases are Chebyshev polynomials, Legendre polynomials, and other Jacobi polynomials. These bases can be used to represent non-periodic functions. The key feature of spectral methods is that discretization is global rather than local. The derivatives of the solution at a given point are determined from the solution values at every point. Therefore, the order of accuracy of the solution increases as points are added. Thus in the limit as an infinite number of discrete points are used, the order of accuracy becomes infinite. This is referred to as *spectral accuracy* and is in direct contrast to a local discretization method such as finite difference, in which as the number of points becomes infinite, the order of accuracy of the scheme remains fixed at, for example, second order.

The formal arguments as to the accuracy of spectral discretizations are more complex than those of finite difference schemes. Refer to Canuto *et al.*(1988) for a thorough analysis of spectral methods. In this study, several numerical experiments are performed to demonstrate the accuracy of the spectral scheme. These are found in §4.1.

This section shows an example of the use of spectral methods for solving a one-dimensional heat equation. Then, the Fourier and Chebyshev discretizations are described in detail. The notation used in this section is tailored to its use in subsequent sections. In particular note that the Fourier and Chebyshev collocation methods determine the location of the discrete grid points and give the derivative operator as a matrix. This will be used extensively in the discretization shown in §3.2.

3.1.1. Model Problem

To demonstrate the use of an orthogonal basis to solve a partial differential equation, consider the 1-D heat equation:

$$\frac{\partial}{\partial t}f(x,t) = -\frac{\partial^2}{\partial x^2}f(x,t) \qquad \textbf{(3.1)}$$

with appropriate boundary conditions. The dependent variable $f(x,t)$ can first be expanded in terms of any complete basis $\phi_n(x)$ with $n = 0,1,2...,\infty$ or with $n = -\infty,...,\infty$, depending on the basis. Assuming the latter is used,

$$f(x,t) = \sum_{n=-\infty}^{\infty} \hat{f}_n(t)\,\phi_n(x) \tag{3.2}$$

The spatial derivatives of the basis functions are needed to determine the spatial derivatives of f . They must be expressed in terms of the original basis. Once this is known, the next step is to expand the spatial derivative of f in terms of the orthogonal basis. In this case, for example,

$$\frac{d^2}{dx^2}\phi_n(x) = \sum_{m=-\infty}^{\infty} g_{nm}\,\phi_m(x) \tag{3.3}$$

Once this is known, the next step is to expand the spatial derivative of f in terms of the orthogonal basis.

$$\begin{aligned} \frac{\partial^2}{\partial x^2} f(x,t) &= \sum_{n=-\infty}^{\infty} \hat{f}_n(t)\frac{d^2\phi_n(x)}{dx^2} = \sum_{n=-\infty}^{\infty} \hat{f}_n(t) \sum_{m=-\infty}^{\infty} g_{nm}\phi_m(x) \\ &\equiv \sum_{p=-\infty}^{\infty} \hat{f}_{p,xx}(t)\,\phi_p(x) \quad \text{where} \quad \hat{f}_{p,xx}(t) \equiv \sum_{m=-\infty}^{\infty} g_{mp}\hat{f}_m(t) \end{aligned} \tag{3.4}$$

A spatially discrete system is then easily obtained by truncating the expansion to include only N+1 terms $n = -N/2,\ldots,N/2$. Substituting the discrete expansion of f and its second derivative into Eq. (3.1) yields a system of N+1 ordinary differential equations in time. In the example,

$$\frac{d}{dt}\hat{f}_n(t) = -\hat{f}_{n,xx}(t) \quad , \quad n = -N/2,\ldots,N/2 \tag{3.5}$$

Once the relationship between the basis functions and their derivatives is determined, that is, the constants g_{nm}, most of which are zero, the system can be easily solved.

The goal of the spectral discretization is to transform the original differential equation into $N+1$ ordinary differential equations in time. The boundary conditions are implemented in various ways depending on the type of scheme used. The crux of the discretization is the determination of the spatial derivatives of the basis functions. Then, a self-consistent set of coupled ordinary differential equations for the amplitude of each basis function is obtained.

Two approaches to setting up this system of ODEs are used in this study. The Fourier Galerkin method, described in the next section, uses a Fourier basis to represent the solution to the governing equations. The equations themselves are transformed into Fourier space. The second and third are both called collocation methods. These methods use the basis function formulation to derive a method of differentiating the solution, without the need to transform the solution into Fourier or Chebyshev space. The derivative is obtained as a matrix multiplication operator.

3.1.2. Fourier Galerkin Method

The *Fourier Galerkin* spectral method uses a trigonometric polynomial basis, or Fourier basis, to represent the solution to the governing equations. The application of the Fourier basis to the above model problem is straight-forward. A domain of $x \in [0,2\pi]$ is assumed.

$$\phi_n(x) = e^{inx}$$

$$f(x,t) = \sum_{n=-\infty}^{\infty} \hat{f}(t)e^{inx}$$

$$\frac{\partial^2}{\partial x^2}f(x,t) = \sum_{n=-\infty}^{\infty} -n^2\hat{f}_n(t)e^{inx} \equiv \sum_{n=-\infty}^{\infty} \hat{f}_{n,xx}(t)e^{inx} \tag{3.6}$$

$$\text{where } \hat{f}_{n,xx}(t) = -n^2\hat{f}_n(t)$$

and the resulting system of ordinary differential equations would be, after truncation:

$$\frac{d}{dt}\hat{f}_n(t) = n^2\hat{f}_n(t) \quad , \quad n=-N/2,...,N/2 \tag{3.7}$$

The Fourier basis has the unique property that derivatives of a basis function are proportional, with a complex constant, to the basis function. Thus the ODEs that are obtained from discretization are decoupled. Notice, however, that this occurs only for linear differential equations with coefficients that are constant in the direction of discretization! Nonlinear terms and non-constant coefficient terms introduce coupling in the ODEs. However, these terms will not be treated using a Fourier Galerkin method in this study, but will instead employ the Fourier collocation method of the next section.

3.1.3. Fourier Collocation Method

The Fourier collocation method, and the Chebyshev collocation method of the following section use orthogonal bases to satisfy the governing equations as did the Fourier Galerkin method. However, the Fourier Galerkin method, by solving the governing equations in transform space, assumes that the solution satisfies the transformed governing equations everywhere in the domain, and that the solution will have an error of the order of the lowest frequency mode neglected in the approximation. However, collocation methods assume that the basis functions hold only at certain points, called the *collocation points*, which are given by a quadrature rule. Thus the solution is represented as $N+1$ discrete values rather than $N+1$ mode amplitudes. The basis is used to determine the relationship between the solution and its derivatives.

In the Fourier collocation method, again trigonometric polynomials are used as a basis. The solution is determined at $N+1$ collocation points, where is N is even. The Gauss-Lobatto collocation points are used:

$$\xi_i = \frac{2\pi i}{N+1} \quad , \quad i=0,\ldots,N \tag{3.8}$$

where the dependent variables are periodic in ξ with period 2π and are represented on the computational domain $\xi \in [0,2\pi]$. The values of the dependent variables at the collocation points are given by the expansion, (usually called the inverse Fourier transform):

$$f(\xi_i) = \sum_{k=-N/2}^{N/2} \hat{f}_k e^{ik\xi_i} \tag{3.9}$$

and the expansion coefficients are given by the Fourier transform:

$$\hat{f}_k = \frac{1}{N+1} \sum_{i=0}^{N} f(\xi_i)\, e^{-ik\xi_i} \tag{3.10}$$

Differentiation of the dependent variables is accomplished through the expansion:

$$\left.\frac{df}{d\xi}\right|_{\xi_i} = \sum_{k=-N/2}^{N/2} \mathrm{i}k\hat{f}_k \mathrm{e}^{\mathrm{i}k\xi_i} \tag{3.11}$$

The transformations and differentiation can be expressed strictly as matrix operations. First, the dependent variable and its transform are expressed in vector notation:

$$\begin{aligned} F &\equiv \text{vector } \{f(\xi_i)\,|\,i=0,N\} \\ \frac{d}{d\xi}F &\equiv \text{vector } \{\frac{df}{d\xi}(\xi_i)\,|\,i=0,N\} \\ \hat{F} &\equiv \text{vector } \{\hat{f}_k\,|\,k=-N/2,N/2\} \end{aligned} \tag{3.12}$$

The Fourier transform and inverse transform are then expressed as matrix multiplies:

$$F = C_F^{-1}\hat{F} \qquad \hat{F} = C_F F$$
$$\text{where } \{C_F^{-1}\}_{jk} = \mathrm{e}^{\mathrm{i}k\xi_j}, \qquad \{C_F\}_{jk} = \frac{1}{N+1}\,\mathrm{e}^{-\mathrm{i}k\xi_j} \tag{3.13}$$

and differentiation is also represented as a matrix multiply:

$$\begin{aligned} \frac{d}{d\xi}F &= D_F F \\ D_F &= C_F^{-1}\operatorname{diag}\{\mathrm{i}k\}C_F \end{aligned} \tag{3.14}$$

The matrix derivative D_F can also be evaluated in closed form using:

$$\{D_F\}_{ij} = -\frac{1}{N+1}\sum_{k=-N/2}^{N/2} k\sin\left(\frac{2k(i-j)\pi}{N+1}\right) \tag{3.15}$$

The model problem, Eq. (3.1) , can be formulated using the Fourier collocation method. Using the notation of Eq. (3.12), the heat equation can be expressed as:

$$\frac{dF}{dt} = -D_F^2 F \tag{3.16}$$

Also, a nonlinear problem may also be formulated using the Fourier collocation method. For example the nonlinear Burger's equation,

$$\frac{\partial}{\partial t} f(x,t) = -f(x,t)\,\frac{\partial f(x,t)}{\partial x} \tag{3.17}$$

with periodic boundary conditions can be discretized spatially as:

$$\frac{dF}{dt} = -F * (D_F F) \tag{3.18}$$

where the multiplication in the nonlinear term is a pointwise vector multiply, denoted by the symbol *. In the remainder of this document, pointwise multiplication, rather than an inner or outer product, is assumed when two vectors are multiplied and the symbol * is omitted.

To review, a single matrix operator D_F is derived which represents the combination of transforming the solution into Fourier space, taking the derivative by scaling each expansion coefficient, and transforming the solution back into physical space. Note that the periodic boundary condition on the solution is automatically satisfied by the choice of basis functions and that no additional boundary conditions are needed. See

Canuto *et al.*(1988) for more details on the Fourier collocation method, including estimates of accuracy.

3.1.4. Chebyshev Collocation Method

In the *Chebyshev collocation method*, a Chebyshev polynomial basis is used to represent the solution. Chebyshev polynomials are given by:

$$T_m(\xi_i) = \cos\left(m\cos^{-1}(\xi_i)\right) \tag{3.19}$$

Trigonometric identities give the following recursion relations for Chebyshev polynomials:

$$\begin{gathered} T_0(\xi) \equiv 1 \\ T_1(\xi) \equiv \xi \\ T_{m+1}(\xi) \equiv 2\xi T_m(\xi) - T_{m-1}(\xi) \quad , \quad m \geq 1 \end{gathered} \tag{3.20}$$

The derivative of a Chebyshev polynomial is found in terms of other Chebyshev polynomials using the recursion properties. The recursion rule for the derivative is:

$$2T_m(\xi) = \frac{1}{m+1} T'_{m+1}(\xi) - \frac{1}{m-1} T'_{m-1}(\xi) \quad m \geq 1 \tag{3.21}$$

To discretize a differential equation using the Chebyshev collocation method, first, the collocation points are defined from a Chebyshev quadrature rule:

$$\xi_i = -\cos\left(\frac{\pi i}{N}\right) \tag{3.22}$$

Then, the solution at the collocation points is expanded in terms of the Chebyshev basis:

$$f(\xi_i) = \sum_{m=-N}^{N} \hat{f}_m T_m(\xi_i) \tag{3.23}$$

Again, the solution, its transform, and its derivative are represented as solution vectors of length $N+1$:

$$\begin{aligned} F &\equiv \text{vector } \{f(\xi_i)\,|\,i=0,N\} \\ \frac{d}{d\xi}F &\equiv \text{vector } \{\frac{df}{d\xi}(\xi_i)\,|\,i=0,N\} \\ \hat{F} &\equiv \text{vector } \{\hat{f}_m\,|\,m=0,N\} \end{aligned} \tag{3.24}$$

The Chebyshev transform and inverse Chebyshev transform are then given as matrix multiplication operators:

$$F = C_C^{-1}\hat{F} \qquad \hat{F} = C_C F$$

$$\{C_C^{-1}\}_{jk} = \cos\left(\frac{\pi jk}{N}\right), \quad \{C_C\}_{jk} = \frac{2}{Nc_jc_k}\cos\left(\frac{\pi jk}{N}\right) \tag{3.25}$$

$$c_m = \begin{cases} 2 & m=0,N \\ 1 & 1\le m\le N-1 \end{cases}$$

Differentiation is again accomplished through a matrix multiplication:

$$\begin{aligned} \frac{d}{d\xi}F &= D_C F \\ D_C &= C_C^{-1}\, R\, C_C \end{aligned} \tag{3.26}$$

The R operator above refers to the application of the recursion relationship of Eq. (3.21), which can be expressed as a matrix multiply. As in the Fourier collocation method, a closed form exists for the Chebyshev derivative operator:

$$\{D_C\}_{mn} = \begin{cases} \dfrac{c_m}{c_n}\,\dfrac{(-1)^{m+n}}{\xi_m - \xi_n} & m \neq n \\[2ex] \dfrac{-\xi_m}{2(1-\xi_m^2)} & 1 < m = n < N \\[2ex] \dfrac{2N^2+1}{6} & m = n = 1 \\[2ex] -\dfrac{2N^2+1}{6} & m = n = N \end{cases} \qquad \mathbf{(3.27)}$$

The Chebyshev collocation method can be applied to the above model problems. However, the boundary conditions cannot be periodic. Rather, say the end values are fixed, and the domain is given as $x \in [-1,1]$. The first problem is discretized as:

$$\frac{dF}{dt} = -D_C^2 F \qquad \mathbf{(3.28)}$$

The boundary conditions are imposed directly by removing the two equations at the boundaries and replacing them with conditions that the statement of fixed boundary conditions:

$$\begin{aligned} F_0 &= f(-1) \\ F_N &= f(1) \end{aligned} \qquad \mathbf{(3.29)}$$

3.1.5. Chebyshev Collocation Method on a Staggered Grid

In this study a staggered grid is needed in the direction in which Chebyshev polynomials are used. Specifically, the pressure solution and continuity equation are located at points staggered from the velocity solution and momentum equation. This can be easily accomplished within the collocation framework. The "half-cell" grid points, called the *half points* for lack of a better name, are prescribed by the quadrature rule:

$$\xi_{i+\frac{1}{2}} = -\cos\left(\frac{\pi\left(i+\frac{1}{2}\right)}{N}\right) \qquad \textbf{(3.30)}$$

The Chebyshev transform and inverse transform on the half points are modified slightly:

$$\{C_C^{-1}\}_{jk} = \cos\left(\frac{\pi(j+\frac{1}{2})k}{N}\right) \ , \qquad \{C_C\}_{jk} = \frac{2}{Nc_jc_k}\cos\left(\frac{\pi(j+\frac{1}{2})k}{N}\right) \qquad \textbf{(3.31)}$$

$$\text{for} \qquad 0 \le j \le (N-1) \qquad \text{and} \qquad 0 \le k \le N$$

The operators on the half points are denoted with a "*o*". The grid points are denoted with "+". Interpolation between the grid points and the half points is accomplished by Chebyshev interpolation. To interpolate, for example, the pressure *P* from the half points to the grid points, the pressure is transformed from the half point physical values into Chebyshev space, and then from Chebyshev space onto the regular grid points. This can be represented as a matrix operation:

$$P^{+} = A_o^{+} P^{o}$$

$$\text{where} \quad A_o^{+} = C_C^{-1} C_C^{o} \qquad \textbf{(3.32)}$$

where A_+^o represents interpolation from the grid points to the half points. The inverse of this matrix is:

$$A_o^+ = (A_+^o)^{-1} = (C_C^o)^{-1} C_C \tag{3.33}$$

and represents the reverse interpolation.

3.1.6. Chebyshev Quadrature

To determine the kinetic energy of the disturbance in the simulation, an integral is needed across the Chebyshev grid. This can be accomplished using Chebyshev quadrature. The weights for Chebyshev quadrature are computed by integrating the recursion rule Eq. (3.21). The integration is given by:

$$\int_{-1}^{1} f(\xi)\, d\xi = \sum_{i=0}^{N} w_i\, f(\xi_i)$$

$$w_i = \begin{cases} \displaystyle\sum_{\substack{m=0 \\ m\ even}}^{N} \frac{4c_m}{N(1-m^2)} \cos\left(\frac{\pi m i}{N}\right) & 0<i<N \\ \displaystyle\frac{1}{(N^2-1)} & i=0,N \end{cases} \tag{3.34}$$

3.1.7. Summary

The use of basis functions in all three spatial directions allows discrete derivative operators to be derived, assuming that the solution is represented on certain collocation points. In the next section, these operators and collocation points are used to discretize the continuum Navier-Stokes equations formulated for general 2-D channels.

3.2. Spatial Discretization of Governing Equations

The general approach for the spatial discretization of the Navier-Stokes equations for a generalized 2-D channel geometry is to use 1) a Fourier Galerkin method in the spanwise direction, excluding the nonlinear terms, 2) a Fourier collocation method in the streamwise direction and to evaluate the nonlinear terms in the spanwise direction, and 3) a Chebyshev collocation method in the wall-normal direction. The mixed use of Fourier Galerkin and Fourier collocation in the spanwise direction is consistent with the literature, but note that in some of the literature this type of method would be called a "pseudo-spectral method" or a would retain the name "collocation method." In both cases, the implication is that the method is not truly Galerkin if some terms are evaluated using a collocation method.

The approach to the spatial discretization in this study is similar to that used by others to study plane and curved channel flows. See the review of Kleiser and Zang (1991) and the simulations of Orszag and Patera (1983), Finlay, Keller and Ferziger (1988), Streett and Hussaini (1991) and Zang and Hussaini (1987). However, this study differs notably from those above in that a general curvilinear coordinate system is used in the plane of the streamwise and wall-normal directions. Two examples of studies of 2-D channel flows incorporating general curvilinear coordinates are Karniadakis, Mikic and Patera (1988) and Guzmán and Amon (1994), both of which used the spectral element numerical method. This method is quite different from the spectral method used here. The spectral element method is closely related to the finite element method and uses local basis functions to represent the solution quantities on small geometric elements. The present method uses global basis functions as described in the previous chapter.

The discrete form of the Navier-Stokes equations will be derived first by transforming the equations into Fourier space. The nonlinear terms are included as a source term which will be computed using the Fourier collocation method. Second, the solution will be discretized on the Fourier-Chebyshev collocation grid, with pressure and continuity staggered. The continuum derivative operators will be replaced with discrete spectral operators. In addition, the metrics in the equations will be replaced with discrete vectors containing values of the metrics at each point.

3.2.1. Discretization in the Spanwise Direction

The contravariant component momentum equations, Eq. (2.15), are Fourier transformed in the spanwise direction:

$$
\begin{aligned}
&\frac{\partial \hat{u}_k^{\,m}}{\partial t} + \frac{1}{Re} k^2 g^{22} \hat{u}_k^{\,m} \\
&- \frac{1}{Re}\frac{1}{\sqrt{g}}\left[\frac{\partial}{\partial \xi^1}\left(\sqrt{g}\, g^{11} \frac{\partial \hat{u}_k^{\,m}}{\partial \xi^1} \right) + \frac{\partial}{\partial \xi^1}\left(\sqrt{g}\, g^{13} \frac{\partial \hat{u}_k^{\,m}}{\partial \xi^3} \right) \right. \\
&\quad + \frac{\partial}{\partial \xi^3}\left(\sqrt{g}\, g^{31} \frac{\partial \hat{u}_k^{\,m}}{\partial \xi^3} \right) + \frac{\partial}{\partial \xi^3}\left(\sqrt{g}\, g^{33} \frac{\partial \hat{u}_k^{\,m}}{\partial \xi^3} \right) \\
&\left. + \frac{\partial}{\partial \xi^1}\left(\sqrt{g}\, g^{11} \hat{u}_k^{\,n} \right)\Gamma^m_{1n} + \frac{\partial}{\partial \xi^1}\left(\sqrt{g}\, g^{13} \hat{u}_k^{\,n} \right)\Gamma^m_{3n} + \frac{\partial}{\partial \xi^3}\left(\sqrt{g}\, g^{31} \hat{u}_k^{\,n} \right)\Gamma^m_{1n} + \frac{\partial}{\partial \xi^3}\left(\sqrt{g}\, g^{33} \hat{u}_k^{\,n} \right)\Gamma^m_{3n} \right] \\
&- \frac{1}{Re}\left[g^{11}\left(\frac{\partial \hat{u}_k^{\,n}}{\partial \xi^1}\Gamma^m_{1n} + \hat{u}_k^{\,n}\Lambda^m_{11n} \right) + g^{13}\left(\frac{\partial \hat{u}_k^{\,n}}{\partial \xi^3}\Gamma^m_{1n} + \hat{u}_k^{\,n}\Lambda^m_{13n} \right) \right. \\
&\left. \quad + g^{31}\left(\frac{\partial \hat{u}_k^{\,n}}{\partial \xi^1}\Gamma^m_{3n} + \hat{u}_k^{\,n}\Lambda^m_{31n} \right) + g^{33}\left(\frac{\partial \hat{u}_k^{\,n}}{\partial \xi^3}\Gamma^m_{3n} + \hat{u}_k^{\,n}\Lambda^m_{33n} \right) \right] \\
&+ g^{1m}\frac{\partial}{\partial \xi^1}\hat{p}_k + \mathrm{i}k g^{2m}\hat{p}_k + g^{3m}\frac{\partial}{\partial \xi^3}\hat{p}_k = -g^{1m}\frac{\partial P}{\partial \xi^1} - g^{3m}\frac{\partial P}{\partial \xi^3} + \hat{F}_k^{\,m} + \hat{Q}_k^{\,m}
\end{aligned}
\tag{3.35}
$$

for $k = -N_2/2$, $N_2/2$, and $m = 1,2,3$. The nonlinear convective term is given by $\hat{F}_k$, which represents the k mode of the transformed nonlinear term. The discretization of the nonlinear term in physical space is given in Eq. (3.42).

The transformed continuity equation in terms of contravariant velocities is:

$$\frac{1}{\sqrt{g}}\frac{\partial}{\partial \xi^1}\left(\sqrt{g}\,\hat{u}_k^1\right) + \mathrm{i}k\hat{u}_k^2 + \frac{1}{\sqrt{g}}\frac{\partial}{\partial \xi^3}\left(\sqrt{g}\,\hat{u}_k^3\right) = 0 \tag{3.36}$$

3.2.2. Discretization in Streamwise and Wall-Normal Directions

The spatial differentiation in the streamwise and wall-normal directions is accomplished through the Fourier and Chebyshev collocation methods, respectively, described above. The discrete solution vector is represented as:

$$\begin{aligned} \hat{\boldsymbol{U}}_k &= \hat{U}_k^{\,m}\vec{e}_m \\ \hat{U}_k^{\,m} &= \mathrm{vector}\{\hat{u}_k^{\,m}(\xi_i^1,\xi_j^3) \mid i=0,N_1 \ , \ j=0,N_3\} \\ \hat{P}_k^{\,m} &= \mathrm{vector}\{\hat{p}_k^{\,m}(\xi_i^1,\xi_{j+\frac{1}{2}}^3) \mid i=0,N_1 \ , \ j=0,N_3-1\} \end{aligned} \tag{3.37}$$

for $k = -N_2/2$, $N_2/2$. The metric terms are written as diagonal matrices so that matrix multiplication can be used to represent the products in Eqs. (3.35) and (3.36). These are written as:

$$\begin{aligned} G &= \mathrm{diag}\{\sqrt{g}(\xi_i^1,\xi_j^3)\} \\ G^{mn} &= \mathrm{diag}\{g^{mn}(\xi_i^1,\xi_j^3)\} \\ \Gamma_{mn}^{p} &= \mathrm{diag}\{\Gamma_{mn}^{p}(\xi_i^1,\xi_j^3)\} \\ \Lambda_{mnp}^{q} &= \mathrm{diag}\{\Lambda_{mnp}^{q}(\xi_i^1,\xi_j^3)\} \end{aligned} \tag{3.38}$$

To obtain the spatially discrete governing equations, derivatives in the streamwise and wall-normal directions are replaced by their matrix equivalents. In addition, a matrix collocation derivative is required in the spanwise direction for the evaluation of the nonlinear term. These matrix operators are:

$$\begin{gathered} D_1 = \frac{\partial}{\partial \xi^1} = \text{Fourier Collocation in } \xi^1 \\ D_2 = \frac{\partial}{\partial \xi^2} = \text{Fourier Collocation in } \xi^2 \text{, for use in non-linear term} \\ D_3 = \frac{\partial}{\partial \xi^3} = \text{Chebyshev Collocation in } \xi^3 \end{gathered} \qquad \textbf{(3.39)}$$

Additional multiplications by Chebyshev interpolation matrices are required to account for the staggered pressure and continuity equation. The spatially discrete momentum equations are:

$$\begin{gathered} \frac{\partial}{\partial t} \hat{U}_k^m - \frac{1}{Re} \mathrm{i} k^2 \hat{U}_k^m - \frac{1}{Re}\left[(E_1 D_1 + E_3 D_3)\hat{U}_k^m + \Gamma_{ij}^m H_i \hat{U}_k^j + S_p^m \hat{U}_k^p\right] \\ + F_m \hat{P}_k^+ = -\hat{\mathscr{F}}_k^m - G^{mi}\frac{\partial P}{\partial \xi^i} + \hat{Q}_k^m \end{gathered}$$

where

$$\begin{gathered} E_i = G^{-1}(D_1 G G^{i1} + D_3 G G^{i3}) \\ F_i = G^{i1} D_1 + G^{i3} D_3 \\ H_i = E_i + F_i \\ S_p = \Lambda_{ijp}^m G^{ij} \end{gathered} \qquad \textbf{(3.40)}$$

and $\hat{P}_k^+ = A_o^+ \hat{P}_k$

for $k = -N_2/2, N_2/2$, and m=1,2,3, where the nonlinear convective terms are calculated in physical (non-transformed) space and then transformed into Fourier space. The solution vector representations of the velocity and nonlinear term are:

$$
\begin{aligned}
U^m &= \text{vector}\{u^m(\xi_i^1,\xi_n^2,\xi_j^3) \mid i=0,N_1\ ,\ n=0,N_2\ ,\ j=0,N_3\} = C_F \hat{U}^m \\
\hat{U}^m &= \text{vector}\{\hat{u}_k^m(\xi_i^1,\xi_j^3) \mid k=-N_2/2\,,N_2/2\ ,\ i=0,N_1\ ,\ j=0,N_3\} \\
\mathscr{F}^m &= \text{vector}\{\ f^m(\xi_i^1,\xi_n^2,\xi_j^3) \mid i=0,N_1\ ,\ n=0,N_2\ ,\ j=0,N_3\} = C_F \hat{\mathscr{F}}^m \\
\hat{\mathscr{F}}^m &= \text{vector}\{\hat{f}_k^m(\xi_i^1,\xi_j^3) \mid k=-N_2/2\,,N_2/2\ ,\ i=0,N_1\ ,\ j=0,N_3\}
\end{aligned}
\qquad \textbf{(3.41)}
$$

$$\text{where} \qquad f = f^m \vec{e}_m = \nabla\cdot(\boldsymbol{uu})$$

Using the above notation, the nonlinear term is written:

$$
\begin{gathered}
\mathscr{F}^m = J_1 U^1 U^m + J_2 U^2 U^m + J_3 U^3 U^m + \\
\Gamma_{11}^m U^1 U^1 + 2\Gamma_{13}^m U^1 U^3 + \Gamma_{33}^m U^3 U^3 \\
\text{where} \\
J_1 = G^{-1} D_1 G \\
J_2 = G^{-1} D_2 G \\
J_3 = G^{-1} D_3 G
\end{gathered}
\qquad \textbf{(3.42)}
$$

The Fourier transforms are accomplished through matrix multiplications. The steps for computing the nonlinear term are:

$$
\begin{aligned}
&1)\ \ U^m = C_F^{-1}\ \hat{U}^m \\
&2)\ \ \text{Compute } \mathscr{F}^m \\
&3)\ \ \hat{\mathscr{F}}^m = C_F\ \mathscr{F}^m
\end{aligned}
\qquad \textbf{(3.43)}
$$

Finally, the continuity equation, interpolated onto the staggered grid, is:

$$A^o\left(D_1 G \hat{U}_k^1 + \mathrm{i}k\hat{U}_k^2 + D_3 G \hat{U}_k^3\right) = 0 \qquad \textbf{(3.44)}$$

3.2.3. Final Spatially Discrete Matrix System

The above system of equations must be solved in a coupled manner in order to determine the discrete solution at all times. The coupled matrix system, still continuous in time, can be concisely expressed as:

$$\boldsymbol{A} = \left\{ \begin{matrix} \boldsymbol{L} & \boldsymbol{G} \\ \boldsymbol{D} & \boldsymbol{0} \end{matrix} \right\}$$

$$\left\{ \begin{matrix} \frac{\partial}{\partial t}\hat{U}_k \\ 0 \end{matrix} \right\} + \boldsymbol{A} \left\{ \begin{matrix} \hat{\boldsymbol{U}}_k \\ \hat{P}_k \end{matrix} \right\} = \left\{ \begin{matrix} \hat{\boldsymbol{R}}_k \\ 0 \end{matrix} \right\} \tag{3.45}$$

for $k = -N_2/2, N_2/2$. The terms $\boldsymbol{L}$, $\boldsymbol{G}$, and $\boldsymbol{D}$ refer to the linear Laplacian, gradient, and divergence coefficients, respectively, obtained from placing Eqs. (3.40) and (3.44) in matrix form. The N_2+1 systems are coupled through the term $\hat{\boldsymbol{R}}_k$, which represents the three terms on the right hand side of Eq. (3.40)

Boundary conditions are implemented directly by omitting equations from the above matrix system and replacing them with implicit statements of the boundary conditions. The periodic condition in the streamwise and spanwise directions is automatically satisfied by the Fourier discretization. At the walls, the velocity is specified. While no boundary conditions on the pressure are required, it is necessary to provide one pressure condition. Since the pressure appears in the governing equations only in terms of its gradient, the pressure is determined only up to an arbitrary constant. This is manifested in the current formulation as a single zero eigenvalue in the linear coefficient matrix, $\boldsymbol{A}$, due to a redundant equation in the continuity equation. Therefore, one continuity equation, at an arbitrary location, is removed and replaced by a condition which sets the arbitrary value of pressure. This is achieved by requiring that the mean value of pressure be zero. After taking the Fourier transform, this condition becomes:

$$\sum_{i=0}^{N_1} \sum_{j=0}^{N_3} \sqrt{g}\, \hat{p}_k(\xi_i^1, \xi_j^3)\; w_j = 0 \tag{3.46}$$

for each value of k, where w_j represent the Chebyshev quadrature weights of Eq. (3.34).

For a given discrete initial condition, the above system of discrete equations, with prescribed wall velocities and the mean pressure condition, is a well-posed set of coupled ordinary differential equations in time. It does, however, have the problem of being highly ill-conditioned, as will be discussed in Section 4.

3.3. Temporal Discretization and Solution Method

The solution of a set of linear first-order coupled ordinary differential equations (ODEs) is a commonplace problem in numerical analysis. The system is linear in the time derivative, but has a coupled nonlinear function as its source term. This type of problem can be solved using any of a number of standard procedures. Explicit or implicit methods of various orders can be used. For this study, a second-order implicit trapezoidal integration was selected. Iteration is required at each time step to update the nonlinear terms. The scheme could easily be replaced with a higher-order implicit method.

Though the discretized system is a system of ODEs, the partial differential equation (PDE) nature of the original equations has a severe effect on the nature of the coupled discrete system. In particular, the continuity equation acts as an instantaneous compatibility equation between the velocity components which must be satisfied at every point. The approach used here is that while the discretized Navier-Stokes equations can be solved using any of a number of standard procedures for linear first-order coupled

ODEs, the tight coupling enforced by the continuity equation must be carefully accounted for. For this reason, the continuity equation must be completely implicit at each time step and for each iteration. Thus the tight coupling between the solution components will be maintained even as the nonlinear terms are iteratively updated. Numerical experiments in which continuity was solved iteratively all showed rapid divergence.

The application of the trapezoidal integration scheme to the spatially-discrete Navier-Stokes equations is shown in the following section, while the iterative procedure for advancing the solution from one time level to the next is described in §3.3.2.

3.3.1. Temporal Discretization

The integration of the spatially discrete system of equations, Eq. (3.45), can be performed using any numerical method for solving initial-value ordinary differential equations. In this study a second-order central difference discretization is applied. Time is discretized with a constant time step, $t = n\Delta t$. The entire equation is evaluated at the half time level n+1/2. This is achieved by averaging the solution at the n and n+1 time levels. The discretized form of Eq. (3.45) is:

$$\frac{1}{\Delta t}\begin{Bmatrix} \hat{U}_k^{n+1} - \hat{U}_k^{n} \\ 0 \end{Bmatrix} + A\begin{Bmatrix} \dfrac{\hat{\boldsymbol{U}}_k^{n+1} + \hat{\boldsymbol{U}}_k^{n}}{2} \\ \dfrac{\hat{P}_k^{n+1} + \hat{P}_k^{n}}{2} \end{Bmatrix} = \begin{Bmatrix} \hat{\boldsymbol{R}}_k\left(\dfrac{U^{n+1} + U^{n}}{2}\right) \\ 0 \end{Bmatrix} \tag{3.47}$$

This is re-written in terms of the change in the solution vector at each time step. The final discrete version of the governing equations is given in two forms:

$$\frac{1}{\Delta t}\begin{Bmatrix}\Delta\hat{\boldsymbol{U}}_k\\ \boldsymbol{0}\end{Bmatrix} + \boldsymbol{A}\begin{Bmatrix}\hat{\boldsymbol{U}}_k^n + \frac{1}{2}\Delta\hat{\boldsymbol{U}}_k\\ \hat{P}_k^n + \frac{1}{2}\Delta\hat{P}_k\end{Bmatrix} = \begin{Bmatrix}\hat{\boldsymbol{R}}_k\left(\boldsymbol{U}^n + \frac{1}{2}\Delta\boldsymbol{U}\right)\\ 0\end{Bmatrix}$$

where

$$\begin{aligned}\Delta\hat{\boldsymbol{U}}_k &= \hat{\boldsymbol{U}}_k^{n+1} - \hat{\boldsymbol{U}}_k^n\\ \Delta\hat{P}_k &= \hat{P}_k^{n+1} - \hat{P}_k^n\\ \Delta\boldsymbol{U} &= \boldsymbol{U}^{n+1} - \boldsymbol{U}^n\end{aligned} \tag{3.48}$$

or

$$\boldsymbol{B}\begin{Bmatrix}\Delta\hat{\boldsymbol{U}}_k\\ \Delta\hat{P}_k\end{Bmatrix} = \Delta t\left[-\boldsymbol{A}\begin{Bmatrix}\hat{\boldsymbol{U}}_k^n\\ \hat{P}_k^n\end{Bmatrix} + \begin{Bmatrix}\hat{\boldsymbol{R}}_k\left(\boldsymbol{U}^n + \frac{1}{2}\Delta\boldsymbol{U}\right)\\ 0\end{Bmatrix}\right]$$

where

$$\boldsymbol{B} = \begin{Bmatrix}\boldsymbol{I} + \frac{\Delta t}{2}\boldsymbol{L} & \frac{\Delta t}{2}\boldsymbol{G}\\ \frac{\Delta t}{2}\boldsymbol{D} & \boldsymbol{0}\end{Bmatrix} \tag{3.49}$$

In the second form, the linear matrix $\boldsymbol{B}$ is multiplied by the vector of unknowns. The first term on right hand side is known from the previous time level, while the second term is dependent on the unknown $\Delta\boldsymbol{U}$. Thus the system of equations is of the form $\boldsymbol{L}\,\boldsymbol{X} = \boldsymbol{N}(\boldsymbol{X})$, where $\boldsymbol{X}$ is the vector of unknowns, $\boldsymbol{L}$ is a linear coefficient matrix, and $\boldsymbol{N}(\boldsymbol{X})$ is a nonlinear function of $\boldsymbol{X}$. An iterative method is needed in order to solve this system.

3.3.2. Iterative Solution Method

The matrix system Eq. (3.49) is solved at each time step using an iterative solution technique. At each time step, first the change in the solution vector is guessed as $\Delta \boldsymbol{U}_k = \Delta \boldsymbol{U}_k^0$, $\Delta P_k = \Delta P_k^0$. The above system is then used to determine a correction to the guess:

$$\tilde{\boldsymbol{B}} \begin{Bmatrix} \delta \hat{\boldsymbol{U}}_k \\ \delta \hat{P}_k \end{Bmatrix} = \Delta t \cdot \textbf{Residual}$$

$$\text{where} \quad \textbf{Residual} = -\frac{1}{\Delta t} \boldsymbol{B} \begin{Bmatrix} \Delta \hat{\boldsymbol{U}}_k \\ \Delta \hat{P}_k \end{Bmatrix} - \boldsymbol{A} \begin{Bmatrix} \hat{\boldsymbol{U}}_k^n \\ \hat{P}_k^n \end{Bmatrix} + \begin{Bmatrix} \hat{\boldsymbol{R}}_k \left(\boldsymbol{U}^n + \frac{1}{2} \Delta \boldsymbol{U} \right) \\ 0 \end{Bmatrix} \tag{3.50}$$

$$\begin{Bmatrix} \Delta \hat{\boldsymbol{U}}_k^{m+1} \\ \Delta \hat{P}_k^{m+1} \end{Bmatrix} = \begin{Bmatrix} \Delta \hat{\boldsymbol{U}}_k^m \\ \Delta \hat{P}_k^m \end{Bmatrix} + \begin{Bmatrix} \delta \hat{\boldsymbol{U}}_k \\ \delta \hat{P}_k \end{Bmatrix}$$

where $\tilde{\boldsymbol{B}}$ is some approximation to the original $\boldsymbol{B}$. This approximation gives a certain degree of flexibility in the iterative method. For example, if the choice $\tilde{\boldsymbol{B}} = \boldsymbol{I}$ is used, the method collapses to point-Jacobi. The iteration is repeated until the maximum absolute value of the residual is below some convergence criterion. Note, however, that the continuity equation is unstable to the above iterative technique, so a minor revision is necessary. The iterative system is actually solved by requiring that all corrections to the velocity vector be divergence free; that is, every velocity solution and correction is required to satisfy the continuity equation. With this modification, the final iterative system is written:

$$\tilde{\boldsymbol{B}} \begin{Bmatrix} \delta\hat{U}_k \\ \delta\hat{P}_k \end{Bmatrix} = \Delta t \, \{\, \boldsymbol{I} \quad \boldsymbol{0} \,\} \cdot \textbf{Residual} \qquad \textbf{(3.51)}$$

where $\tilde{\boldsymbol{B}}$ contains some approximation to the momentum equation operator, but contains the exact continuity equation operator. The continuity equation has been removed from the right hand side (by multiplication by zero).

To summarize the solution procedure, at each time step the change in the solution is guessed. This guess is selected as the change in the solution at the previous time level. Using the guessed solution, the residual of the momentum equation is computed. The maximum absolute value of the residual at each iteration is computed and compared to some convergence criterion ϵ. For the results in this study, the convergence level was $\epsilon = 10^{-12}$. Typically, 2 to 8 iterations were needed, depending on the size of the time step. For each iteration, the update to the solution was determined using the block Lower-Upper (LU) decomposition method. The block LU method is a version of direct block Gaussian elimination in which the coefficient matrix is factored into lower triangular and upper triangular block matrices, and the solution is found by forward elimination and back substitution of the right hand side into the factored coefficient matrix. The factorization need be performed only once since the coefficient matrix $\tilde{\boldsymbol{B}}$ does not depend on the solution quantities. The matrix, $\tilde{\boldsymbol{B}}$, which can be any suitable approximation to $\boldsymbol{B}$, is selected by removing terms in the Laplacian so that does not depend on the spanwise wavenumber, k. The same $\tilde{\boldsymbol{B}}$, computed and factored one time, is used for all of the spanwise modes. Even with this choice of $\tilde{\boldsymbol{B}}$, it consumes approximately 75% of the memory needed for the simulation.

3.3.3. Comparison with Previous Studies

The direct approach taken here, i.e., an implicit iterative method for the solution of the fully-coupled discretized equations of motion, is somewhat unique. Previous channel flow simulations (i.e., Zang and Hussaini, 1985, 1987, 1990) have used methods for decoupling the momentum equation from the continuity equation by solving a Poisson equation for pressure. They also do not solve the entire equation implicitly; the nonlinear terms are lagged at each time level using a third- or fourth-order Runge-Kutta method. This removes the need for iteration as is used in this study. See Canuto *et al.* (1988) for a complete discussion of the solution methods used by previous authors.

The advantages of an implicit iterative method over an implicit/explicit method are mostly heuristic. It is satisfying to know that the residual of the discrete system will be forced below a convergence criterion at each time step. This is not done in partially explicit methods. The numerical stability properties of implicit methods are somewhat better than explicit methods, though the iteration introduces its own limits on the maximum allowable time step. Finally, the decoupling of the momentum and continuity equations used in previous studies requires the use of approximate boundary conditions on pressure. The validity of various approximate boundary conditions for pressure has been debated. It is certain that any approximate boundary condition imposed on the pressure will introduce some error in the flow solution, bu tit is argued that these errors are of the order of truncation error. Again, see Canuto *et al.* (1988) for details. In this study, the momentum and continuity equations are solved fully coupled, removing the need for such approximations.

The present implicit method is an efficient choice for the general curved channel problem. Though the memory requirements are large (approximately 64 megabytes for a

8x64x8 grid), today's supercomputers have sufficient memory for such computations. In addition, the complexity of the general coordinate system primarily arises in the computation of the Laplacian term in $\boldsymbol{A}$ (and therefore in $\boldsymbol{B}$ and $\tilde{\boldsymbol{B}}$). This term is computed only once at the beginning of the simulation. Finally, the forward elimination and back substitution step required each iteration is quick. It uses low-level matrix operations which are easily vectorized or parallelized to take advantage of the supercomputer architecture. In summary, the numerical approach is efficient and appropriate for the general channel problem.

3.4. Initial Condition

The spatially and temporally discrete system Eq. (3.49) is complete and well-posed. Periodicity is ensured in two spatial dimensions, and the velocity boundary conditions are implemented directly, while no boundary conditions are needed for pressure. The only remaining aspect of the problem is the initial condition. In a temporal simulation of channel flow instabilities, the initial condition is of utmost importance. If an initial condition is specified as simply the base flow with no disturbance, the numerical method would not provide enough truncation error or round-off error to trigger any instabilities in a finite time; since a spectral method is being used, the errors would be of the order of machine accuracy. Thus while in some studies, perturbations which trip instabilities are assumed to exist due to numerical error, this is never the case in simulations of transition, in which the error is controlled to be very small, and any disturbances to the base flow must be carefully prescribed.

The initial condition in a temporal simulation is the entry point for information obtained from linear stability theory. For prescribed dimensions of the geometry and for prescribed Reynolds number, linear stability theory is used to give disturbance waves to start the nonlinear simulation. As was mentioned in Section 1, in the physical problem under consideration, it is assumed that receptivity mechanisms have tripped the primary linear instability mode, so that it has grown to a perceptible amplitude. The actual amplitude of the linear wave, however, is critical to its evolution. Nonlinear effects occur only for disturbances of sufficiently large amplitude. It is conceivable that in a particular experiment or realistic flow situation, that the disturbance environment will vary. Thus, in this study, perturbations of various initial amplitudes are examined, from well within the linear regime to very large amplitude disturbances for which even weakly-nonlinear stability theory is not valid.

The initial condition is comprised of the base flow plus a primary instability wave at a given amplitude, plus other higher modes of various amplitudes. These higher modes are also obtained from linear theory as harmonics of the primary mode. Though the initial amplitude of these harmonics proved to be of little importance in this study, as is shown in Section 4, they are included for completeness and could have important effects in future studies.

The remainder of this section describes the method for determining the initial condition from the results of linear stability theory. The initial conditions for plane and curved channel flow with streamwise disturbances, used to obtain the results of Section 4, are presented. The development of other specific types of initial conditions, such as spanwise modes for the plane and curved channel, and initial conditions for other channel shapes will be reserved for the next phase of this work.

3.4.1. Discrete Linear Stability Modes for Plane Channel Flow

To study the stability of plane or curved channel flow, linear stability theory is used to generate a perturbation to the base flow. The base flow plus perturbation is then supplied as the initial value of the solution. As the solution is marched in time using the above method, the evolution of the perturbation is ascertained. The perturbation is selected as the least stable eigenmode of the linearized stability equations. The eigenmode profiles were obtained using the linear stability code of Herbert (1988a) using the fourth-order Orr-Sommerfeld equation, Eq. (2.33). This code was used to compute the wall-normal velocity component mode shape and to provide the corresponding eigenvalue (complex temporal growth rate) for comparison with numerical results. Given the wall-normal mode shape, the streamwise mode shape and pressure were computed. The streamwise velocity was computed directly from the continuity equation, while the pressure mode was computed from the streamwise momentum equation.

For plane channel flow, the mode shapes were calculated using:

$$\tilde{u}^1(x^3) = -\frac{1}{\mathrm{i}\alpha} D\tilde{u}^3(x^3)$$

$$\tilde{p}(x^3) = \frac{1}{\mathrm{i}\alpha}\left\{\left[\frac{1}{Re}(D^2-\alpha^2)+\mathrm{i}(\omega-\alpha U_b)\right]\tilde{u}^1(x^3) - \frac{dU_b}{dx^3}\tilde{u}^3(x^3)\right\} \qquad \textbf{(3.52)}$$

$$\text{where} \quad D = \frac{\partial}{\partial x^3} = D_3$$

where D_3 is the Chebyshev collocation derivative in computational coordinates. Note that the transformation between Cartesian and computational coordinates is one-to-one in the wall-normal direction due to non-dimensionalization. After the velocity and pressure mode shapes were computed, they were normalized by the maximum value of the modulus of $\tilde{u}^3$.

Multiple disturbance modes, with wavenumbers of α , 2α , 3α , etc., were obtained using this procedure for each combination of Reynolds number and α desired. The initial condition was computed by scaling each disturbance mode by the desired amplitude, ϵ_k, and summing the base flow, given by Eq. (2.20), and the disturbances.

$$\hat{u}^1(x_i^1,x_j^3) = U_b(x_j^3) + \sum_{k=1}^{k_{\max}} \mathrm{Real}\left\{\epsilon_k\ \tilde{u}_k^1(x_j^3)\ e^{ik\alpha x_i^1}\right\}$$

$$\hat{u}^3(x_i^1,x_j^3) = \sum_{k=1}^{k_{\max}} \mathrm{Real}\left\{\epsilon_k\ \tilde{u}_k^3(x_j^3)\ e^{ik\alpha x_i^1}\right\} \qquad \mathbf{(3.53)}$$

$$p\left(x_i^1,x_{j+\frac{1}{2}}^3\right) = \sum_{k=1}^{k_{\max}} \mathrm{Real}\left\{\epsilon_k\ \tilde{p}_k\left(x_{j+\frac{1}{2}}^3\right)\ e^{ik\alpha x_i^1}\right\}$$

The velocities were then converted from Cartesian to contravariant components.

$$u^1(\xi_i^1,\xi_j^3) = \sqrt{g^{11}}\,\hat{u}^1(x_i^1,x_j^3)$$

$$u^3(\xi_i^1,\xi_j^3) = \sqrt{g^{33}}\,\hat{u}^3(x_i^1,x_j^3) \qquad \mathbf{(3.54)}$$

3.4.2. Discrete Linear Stability Modes for Curved Channel Flow

Similarly, for the curved channel, the mode shapes are computed using:

$$\tilde{u}^\theta(r) = -\frac{1}{i\alpha}D(r\tilde{u}^r(r))$$

$$\tilde{p}(r) = \frac{1}{ir\alpha}\left\{\left[\frac{1}{Re}(r^2\mathscr{L} - 1) + ir(r\omega - \alpha U_b)\right]\tilde{u}^\theta(r) + \left[\frac{1}{Re}2i\alpha - r^2\frac{dU_b}{dr} - rU_b\right]\tilde{u}^r(r)\right\} \qquad \mathbf{(3.55)}$$

$$\text{where} \quad \mathscr{L} = D^2 + \frac{1}{r}D - \frac{\alpha^2}{r^2}$$

$$\text{and} \quad D = \frac{\partial}{\partial r} = D_3$$

The mode shapes were normalized by the maximum value of the modulus of $\tilde{u}^{\theta}(r)$. The initial condition was then computed by adding the base flow, given by Eq. (2.27), and the disturbances. After the mode shapes are computed, the velocities are transformed from polar components to contravariant components. These two steps are:

$$\begin{aligned} u^{\theta}(\theta_i,r_j) &= U_{\theta}(r_j) + \sum_{k=1}^{k_{\max}} \mathrm{Real}\left\{ \epsilon_k\ \tilde{u}_k^{\theta}(r_j)\ \mathrm{e}^{\mathrm{i}k\alpha\theta_i}\right\} \\ u^{r}(\theta_i,r_j) &= U_{r}(r_j) + \sum_{k=1}^{k_{\max}} \mathrm{Real}\left\{ \epsilon_k\ \tilde{u}_k^{r}(r_j)\ \mathrm{e}^{\mathrm{i}k\alpha\theta_i}\right\} \\ p\left(\theta_i,r_{j+\frac{1}{2}}\right) &= \sum_{k=1}^{k_{\max}} \mathrm{Real}\left\{ \epsilon_k\ \tilde{p}_k\left(r_{j+\frac{1}{2}}\right)\ \mathrm{e}^{\mathrm{i}k\alpha\theta_i}\right\} \end{aligned} \tag{3.56}$$

$$\begin{aligned} u^1(\xi_i^1,\xi_j^3) &= \sqrt{g^{11}}\, u^{\theta}(\theta_i,r_j) \\ u^3(\xi_i^1,\xi_j^3) &= \sqrt{g^{33}}\, u^{r}(\theta_i,r_j) \end{aligned} \tag{3.57}$$

3.5. Solution Output

The solution to Eq. (3.49) consists of the Fourier transformed values of the velocity components and the pressure at all grid points for each time step. First, the inverse Fourier transform is used to obtain the solution in physical space. This solution is then output in several forms so that the results can be studied effectively. Of course, planes of data at certain times are output so that instantaneous velocity vectors and contours, and pressure contours may be shown. For these results, pressure is spectrally interpolated from the half points to the grid points. In these results, the perturbation quantities are also output by subtracting the original base flow from the instantaneous results. The evolution of the disturbance as it grows or decays and possibly changes form can be investigated by studying snapshots of the flow at various times. In addition, the vorticity is computed for each snapshot of the flow. These computations are summarized in the following section.

It is desirable to perform further analysis of the flow solution every time step or every few time steps, so that the temporal evolution of the disturbances may be tracked closely. This is done using spectral analysis. The flow is decomposed into its Fourier components in the periodic directions. The change in the amplitude and phase of each component in time gives information about the propagation of waves through the domain. The integrated kinetic energy of each wave is also computed and is used as the standard measure of the growth or decay of each wave and the balance of energy between the various modes. The kinetic energy is also useful in that it gives an estimate of the truncation error of the discretization. In theory, the integrated kinetic energy of all neglected modes should be less than the kinetic energy of the highest retained mode. The computation of the temporal evolution of waves in the solution is outlined in §3.5.2.

Finally, it is often desirable to interpolate the solution from a coarser grid to a finer grid. This is needed when the resolution needs to be increased after some time. It is also useful for displaying results obtained on a fairly coarse grid. The low number of points needed in the periodic directions hides makes the solution appear to be very coarse when it is in fact quite accurate. The stability results shown in this study are all interpolated on much finer grids in the streamwise direction. Again, spectral interpolation is used. Since the method is very similar to the interpolation used to transfer values from the grid points to the half points and vise versa, as shown in §3.1.5, it will not be further elaborated upon.

3.5.1. Summary of Output Flow Quantities

The first step in outputting the flow solution is to transform the solution from Fourier space to physical space in the spanwise direction. The solution is computed at the Fourier collocation points given by Eq. (3.8), with $N = N_2$, by multiplying the solution by the transform operator, Eq. (3.13). The second step is to interpolate the pressure, in the wall-normal direction, onto the grid points using the interpolation operator Eq. (3.32). These operations are summarized below:

$$\begin{aligned} U^m &= C_F^{-1}\,\hat{U}^m\,, \quad m=1,2,3 \\ P &= A_o^+\,C_F^{-1}\,\hat{P} \end{aligned} \tag{3.58}$$

After transformation from Fourier space, contravariant velocity components are available on the grid points. To plot velocity vectors, the velocities need to be output as Cartesian components. These are calculated using:

$$\hat{u}^m = \frac{\partial x^m}{\partial \xi^i}\,u^i \tag{3.59}$$

However, to plot contours of velocity for the curved channel case, it is desirable to compute the polar components of velocity, which can be computed from the contravariant components by a linear scaling:

$$\begin{aligned} u^\theta &= \frac{u^1}{\sqrt{g^{11}}} \\ u^r &= \frac{u^3}{\sqrt{g^{33}}} \end{aligned} \tag{3.60}$$

The disturbance velocities and pressure are also obtained by subtracting the base flow, which is given in Cartesian velocity components for the plane channel and in polar components for the curved channel.

Finally, the vorticity is computed from the velocities. Cartesian components of the vorticity are needed:

$$\hat{\omega} = \hat{\omega}_k \hat{e}_k = \epsilon_{ijk} \frac{\partial \hat{u}_j}{\partial x^i} \hat{e}_k$$

$$\text{or} \qquad \hat{\omega}_k = \left(\frac{\partial \hat{u}_j}{\partial x^i} - \frac{\partial \hat{u}_i}{\partial x^j} \right) , \quad \text{for } i, j, k \text{ cyclic} \tag{3.61}$$

The disturbance vorticity is computed by subtracting the vorticity of the base flow from the total vorticity.

3.5.2. Spectral Analysis

The extraction of information about the propagation and growth of instability waves in the solution is not a trivial task. The solution is already Fourier transformed in the spanwise direction. The Fourier transform of the solution in the streamwise direction must be taken:

$$\hat{\hat{u}}^{m}_{k\ell}(\xi^3_j) = \frac{1}{N_1+1} \sum_{p=0}^{N_1} \mathrm{e}^{-\mathrm{i}\ell\xi^1_p} \, \hat{u}_k{}^{m}(\xi^1_p, \xi^3_j) \tag{3.62}$$

The next step is to integrate some quantity in the wall-normal direction. One quantity of interest is the kinetic energy. The kinetic energy of a single streamwise-spanwise Fourier mode is given by:

$$E_{k\ell} = \frac{1}{1+\delta_{0k}} \frac{1}{1+\delta_{0\ell}} \int_{-1}^{1} |\hat{\hat{\boldsymbol{u}}}_{k\ell}(\xi_j^3)|^2 d\xi_3 \ , \quad for \quad k=0,N_2/2 \ , \quad \ell=0,N_1/2$$

$$|\hat{\hat{\boldsymbol{u}}}_{k\ell}(\xi_j^3)|^2 = \left| \hat{\hat{u}}_{k\ell}^m \frac{dx^1}{d\xi^m} \right|^2 + \left| \hat{\hat{u}}_{k\ell}^m \frac{dx^2}{d\xi^m} \right|^2 + \left| \hat{\hat{u}}_{k\ell}^m \frac{dx^3}{d\xi^m} \right|^2 \qquad \mathbf{(3.63)}$$

where the contributions from the negative modes have been summed with the positive modes.

The kinetic energy of a mode exhibits growth or decay as the solution proceeds. Linear theory suggests that this growth is exponential. Therefore, local exponential growth is assumed when computing the growth rate of each mode. Assuming that the local growth is given by:

$$E_{k\ell}(t_2) = E_{k\ell}(t_1)\ \mathrm{e}^{2\,\omega_{k\ell,I}(t_2-t_1)} \qquad \mathbf{(3.64)}$$

where t $_1$ and t $_2$ are two arbitrary times, and $\omega_{k\ell,\mathrm{I}}$ is the imaginary part of the complex growth rate, $\omega_{k\ell,\mathrm{I}}$ may be computed using:

$$\omega_{k\ell,I} = \frac{1}{t_2-t_1} \ln\left(\frac{E_{k\ell}(t_2)}{E_{k\ell}(t_1)} \right) \qquad \mathbf{(3.65)}$$

Obviously, if the growth is not actually exponential, the above equation is only accurate as t_2 approaches t_1. The kinetic energy and growth rate of each mode is computed and output at regular intervals.

Because the kinetic energy is computed from the modulus of the velocity vector, it contains no information about the phase of each mode. Consequently, the rate of oscillation, or the real part of the complex growth rate, cannot be computed from the energy. For this purpose, the transformed wall-normal contravariant velocity component was integrate in the wall-normal direction. This quantity is labeled $f_{k\ell}$:

$$f_{k\ell} = \int_{-1}^{1} \hat{\hat{u}}^{3}_{k\ell}(\xi^{3}_{j})\,d\xi_{3}\ , \quad \mathit{for} \quad k = -N_2/2, N_2/2\ , \quad \ell = N_1/2, N_1/2 \tag{3.66}$$

Again assuming local exponential growth, this integrated complex quantity should be descriptive of the wave nature of the flow and should behave according to:

$$f_{k\ell}(t_2) = f_{k\ell}(t_1)\ \mathrm{e}^{-\mathrm{i}\omega_{k\ell}(t_2 - t_1)} \tag{3.67}$$

where $\omega_{k\ell}$ is complex. To split this relation into expressions for the real and imaginary parts of $\omega_{k\ell}$, the function is separated into amplitude and phase:

$$\begin{aligned} f_{k\ell} &= F_R + \mathrm{i}F_I = |F|\,\mathrm{e}^{\mathrm{i}\Phi} \\ |F| &= \sqrt{F_R^2 + F_I^2} \\ \Phi &= \tan^{-1}\frac{F_I}{F_R} \end{aligned} \tag{3.68}$$

The real and imaginary parts of the complex growth rate can then be found from the phase and amplitude:

$$\begin{aligned} \omega_{k\ell,R} &= \frac{1}{t_2 - t_1}\ \ln\frac{\Phi(t_2)}{\Phi(t_1)} \\ \omega_{k\ell,I} &= \frac{1}{t_2 - t_1}\ \ln\frac{|F|(t_2)}{|F|(t_1)} \end{aligned} \tag{3.69}$$

As will be discussed in Section 4, the imaginary part of the growth rate computed from the two methods above were very close, but not identical. However, the real part of the growth rate was found to match the theoretical oscillation rate very well even for cases for which linear theory does not hold.

3.6. Summary

This chapter contains a description of the majority of the effort performed in this study. The selection and implementation of a numerical method for solving the governing equations of Section 2 was one of the primary goals of this study. The methodology for studying temporal stability problems was also developed, specifically, the computation of the initial condition from linear stability theory. Finally, tools were developed for the analysis of the results to determine the time evolution of the stability waves which were placed in the flow at the initial time. The following chapter shows results that were used to validate the above numerical procedure for plane and curved channel flows to insure that the equations are being solved accurately and that linear stability theory results are reproduced for small amplitude disturbances. The last section of the results moves beyond the validation level and investigates some early nonlinear flow evolutions. However, the development and concurrent validation of the numerical method of this chapter is the key result of this work and will allow future studies to progress in the analysis of the stability of general 2-D channel flows.

Section 4. Plane and Curved Channel Results

The first phase of this study was the development and validation of a two-dimensional computer code for performing the numerical simulation of the temporal stability of channel flows. The mathematical formulation and numerical approach described in the previous chapters were employed. This code was studied extensively to examine its effectiveness for simulation of channel flow problems. Plane and curved channel flows, described in Section 2, were examined.

To generate a two-dimensional version of the formulation, the flow solution was assumed to be constant in the spanwise, or ξ^2-direction, and all terms representing differentiation in the spanwise direction were dropped. In the 2-D stability analysis, the Orr-Sommerfeld equation, Eqs. (2.33) or (2.36) were used to provide Tollmien-Schlichting wave disturbances for the plane and curved channel, respectively. Since the spanwise terms were neglected, the temporal stability behavior only reflects instability in the plane of the streamwise (ξ^1) and wall-normal (ξ^3) directions. The important effects of spanwise linear stability modes and the spanwise secondary instability of Tollmien-Schlichting waves are not considered in this study. In the numerical formulation, requiring the solution to be two-dimensional is equivalent to using a single Fourier mode, the k=0 mode, to represent the spanwise variation of the solution. In this chapter, the flow solution quantities are assumed to correspond to the k=0 mode, and both the k subscript and ^ notation are dropped, i.e., $\hat{u}_k^1 \rightarrow u^1$.

First, the analytical test function analysis described in §2.1.6 was employed to determine the truncation error behavior as the grid resolution and time step were refined. Spectral accuracy was obtained as the number of grid points in the streamwise and wall-normal directions was increased. Second-order accuracy was obtained as the time-step was refined. This analysis, is shown for the plane channel for two Reynolds numbers in §4.1.

As a second validation of the code, and to determine the ability of the code to solve stability problems, linear stability results were obtained for both the plane and curved channel. For the plane channel, two Reynolds numbers were selected to provide both a linearly unstable and a linearly stable test case. For the curved channel, two cases with different radii of curvature were selected, again to provide both a linearly unstable and a linearly stable test case. For these four cases, simulation results were obtained for ten time steps, and the growth and oscillation rates of the stability mode were computed. These were compared to linear theory. By varying the grid resolution, time step, and amplitude of the initial disturbance, the appropriate bounds for obtaining growth rates consistent with linear theory were obtained. These results are shown in §4.2 for the plane channel and in §4.3 for the curved channel.

The final set of results was obtained to study the nonlinear stability of channel flows. Nonlinear stability results were obtained for the same four test cases simply by increasing the amplitude of the initial disturbance. In addition, higher frequency modes were added so that the nonlinear wave interactions between the modes could be examined for different initial amplitudes of the harmonic modes. An attempt was made to determine the long-time evolution of these states. Due to the extremely large number of time steps required, the solution for each case was only integrated in time for up to thirty periods of the Tollmien-Schlichting wave. These results are shown in §4.4.

4.1. Analytical Function Testing

The first validation of the numerical method was performed using the forcing function $\boldsymbol{Q}$ introduced in §2.1.6. This method allows the prescription of arbitrary analytical functions, $\boldsymbol{U}_{\text{test}}$ and P_{test}, which are enforced to be solutions of the Navier-Stokes equations by the proper choice of the forcing function. Using this method, the spatial discretization error in the streamwise and spanwise directions, as well as the temporal discretization error, may be analyzed. Thus without performing the simulation of a flow problem, the accuracy properties of the solution method can be scrutinized.

Two types of analyses were performed. By choosing a steady state test solution the spatial discretization was investigated without running even a single time step. The test solution was simply substituted into the discrete system, Eq. (3.50), and the residual was computed. This residual is exactly zero in the absence of truncation error; when non-zero, the residual of the momentum equation is equal to the combined error in the discretization of the convective (nonlinear) term and the diffusive and pressure gradient (linear) terms. Since the test velocity was always chosen to be a divergence free vector function, the residual of the continuity equation is simply the divergence of the velocity created by discretization error.

The second type of analysis prescribed a solution which varied in time. The test solution at $t = 0$ was used as the initial condition. Then, the simulation was performed to a time of $t = 0.01$ (using $\Delta t = 0.001$ for the spatial accuracy tests). The numerical solution was compared to the test solution at $t = 0.01$. This analysis provided a test of all of the steps in the simulation procedure. For the most part, the maximum error in the solution at

$t = 0.01$ matched the residual from the steady-state analysis quite well. However, the time-dependent analysis revealed to a greater extent the growth of round-off error in the solution procedure, which is due to the high condition number of the system for small Δt and large N. This issue is discussed further in §4.1.5.

4.1.1. Test Solutions

To determine the truncation error in both the spatial and temporal discretization, a divergence-free analytical solution was selected by prescribing the stream function of the solution. The general form for the stream function was selected as:

$$\begin{aligned}\psi(\xi^1,\xi^3) = \; & \left[1 + a_1 \sin(k_1 \xi^1) + b_1 \cos\left(\pi \sin(\xi^1)\right)\right] * \\ & \left[1 + a_3 (\xi^3)^3 + b_3 \sin(k_3 \xi^3)\right] * \\ & \left[1 + a_t t + b_t \exp(k_t t)\right]\end{aligned} \tag{4.1}$$

where the constants a_1, a_3, a_t, b_1, b_3, b_t, k_1, k_3, and k_t determine specific solutions. The flow solution was then prescribed as:

$$\begin{aligned}u^1(\xi^1,\xi^3) &= -\frac{1}{\sqrt{g}}\frac{\partial}{\partial \xi^3}\psi(\xi^1,\xi^3) \\ u^3(\xi^1,\xi^3) &= \frac{1}{\sqrt{g}}\frac{\partial}{\partial \xi^1}\psi(\xi^1,\xi^3) \\ p(\xi^1,\xi^3) &= \frac{1}{\sqrt{g^{11}}} u^1(\xi^1,\xi^3)\end{aligned} \tag{4.2}$$

This general solution was selected so that it would contain spatial components (with coefficients a_1 and a_3) which could be resolved exactly with a small number of modes. This required the use of a sinusoidal solution in the streamwise direction and a polynomial solution in the wall-normal direction. In addition, components of the solution (with coefficients b_1 and b_3) were selected which could not be resolved exactly and would require a large number of modes to achieve machine accuracy. The forcing function vector $\boldsymbol{Q}$ required to make Eq. (4.2) a solution to the momentum equation is obtained as:

$$\boldsymbol{Q} = \frac{\partial \boldsymbol{u}}{\partial t} + \nabla\cdot(\boldsymbol{uu}) + \nabla p - \frac{1}{Re}\nabla^2 \boldsymbol{u} \qquad \textbf{(4.3)}$$

where $\boldsymbol{u}$ and p are given by Eq. (4.2). This substitution was performed separately for the Cartesian and polar momentum equations using *Mathematica* software (Wolfram, 1991). The resulting expressions were stored in the code and evaluated for each point every time step. Results are shown only for the plane channel case, since the curved channel results were very similar.

4.1.2. Streamwise Accuracy

To determine the truncation error in the Fourier collocation method used in the streamwise discretization, two results were calculated, cases A and B in Tab. 4.1. Case A was obtained by specifying the steady-state solution given by Eq. (4.2) with coefficients given in Tab. 4.1. This solution is shown in Fig. 4.1. The residual was calculated for Reynolds numbers of 5,000 and 1,000 for a series of values of N_1 and is shown in Fig. 4.2. In this figure, the residual varies almost exponentially with the number of grid points for N_1 greater than approximately 24 (shown by a near-linear relationship on a semi-log plot), until round-off error becomes dominant, which occurs for N_1 around 48 for the momentum equations. This type of truncation error behavior is characteristic of spectral methods. It is important to note that a truncation error of the order of 10^{-10} can be achieved quite feasibly.

The truncation error was independent of the Reynolds number for the cases shown. This is surprising since the Reynolds number significantly changes the nature of the governing equations. However, it indicates that the predominate source of error is the nonlinear term, which is not scaled by the Reynolds number. It is possible that more extreme values of Reynolds number, e.g. $Re = 1$ or 10^6, would show a difference in the residual, but this was not investigated here. Also note that the residual of the continuity equation decreased more quickly than the momentum equations. This is probably due to the linearity of the continuity equation and is consistent with the conclusion that the nonlinear terms in the momentum equation are the primary source of error in the system.

Case	Re	a_1	b_1	k_1	a_3	b_3	k_3	a_t	b_t	k_t
A	1000 5000	1	1	1	1	0	3	0	0	1
B	5000	1	1	1	1	0	3	1	0	1
C	5000	1	1	1	0	1	3	0	0	1
D	5000	1	1	1	0	1	3	1	0	1
E	5000	1	1	1	0	0	3	1	1	1

Table 4.1. Test Cases for Analytical Function Tests. For each case, the values of the constants in Eq. (4.1) are given in the table.

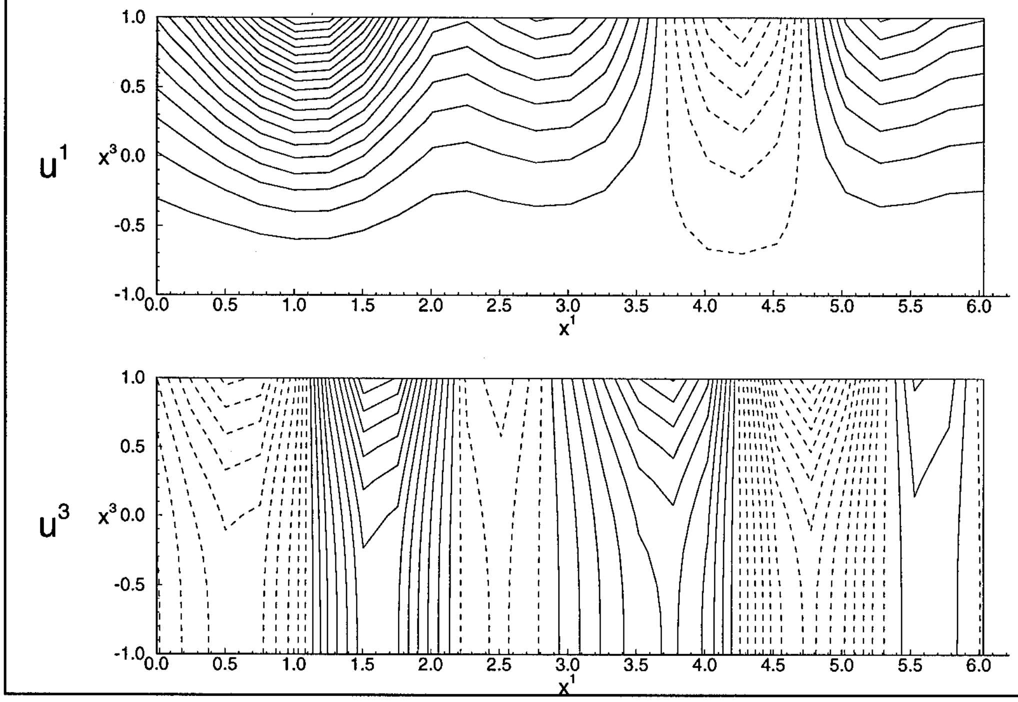

Figure 4.1. Contours of the Prescribed Solution for Streamwise Discretization Analysis of Plane Channel Flow, Case A.

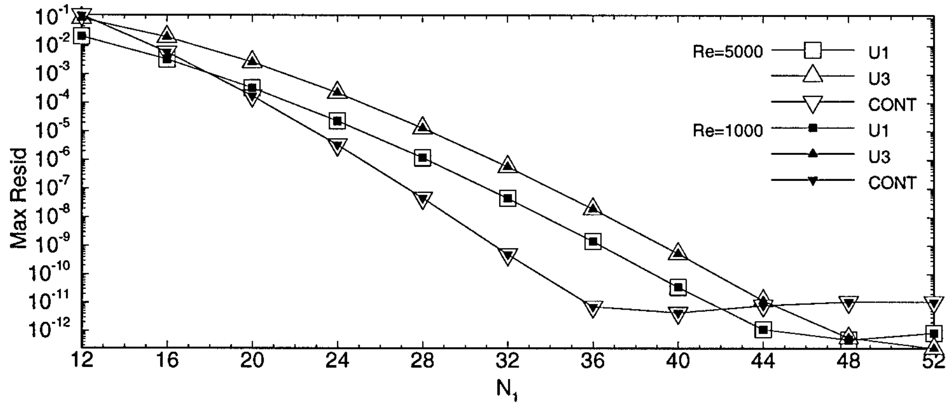

Figure 4.2. Demonstration of Spectral Accuracy in the Streamwise Discretization for Plane Channel, Case A.

The solution for Case B increases linearly with time from the initial state and can therefore be integrated in time without truncation error. For this case, the error in the solution computed after 10 time steps, with Δt=0.001, was calculated. These results are shown in Fig. 4.3. They are qualitatively the same as in Fig. 4.2. That is, the truncation error of the solution achieves spectral accuracy as the number of grid points is increased. It is useful to verify that the residual of the numerical discretization is a good indicator of the error in the computed solution, since the maximum value of the residual is needed to determine convergence at each time step. This result shows the direct correspondence. When the residual is below 10^{-10}, the error in the solution is well below 10^{-9}. As an example of the spatial structure of the error in the solution, the error is shown in Fig. 4.4 for a fairly coarse grid of N_1=12, N_3=12. The oscillatory error in the x^1-direction shows that the error in the solution is associated with missing higher-order terms in the Fourier representation of the solution.

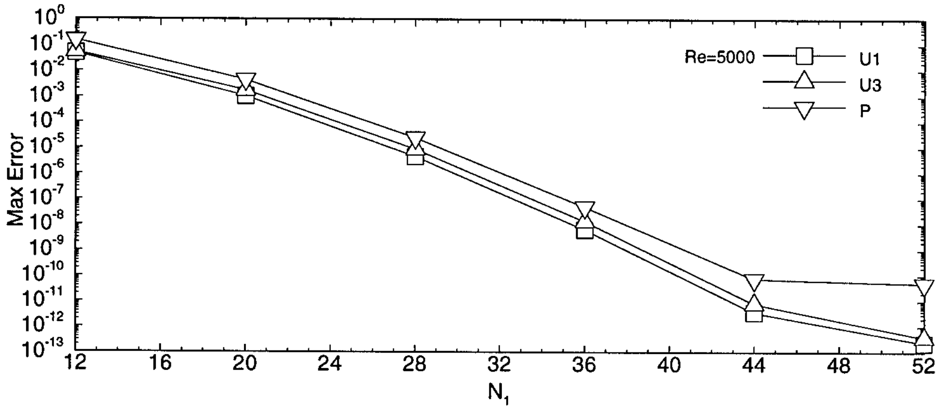

Figure 4.3. Demonstration of Spectral Accuracy in the Streamwise Discretization for Plane Channel, Case B. The maximum error in the solution quantities at time t=0.01 are shown.

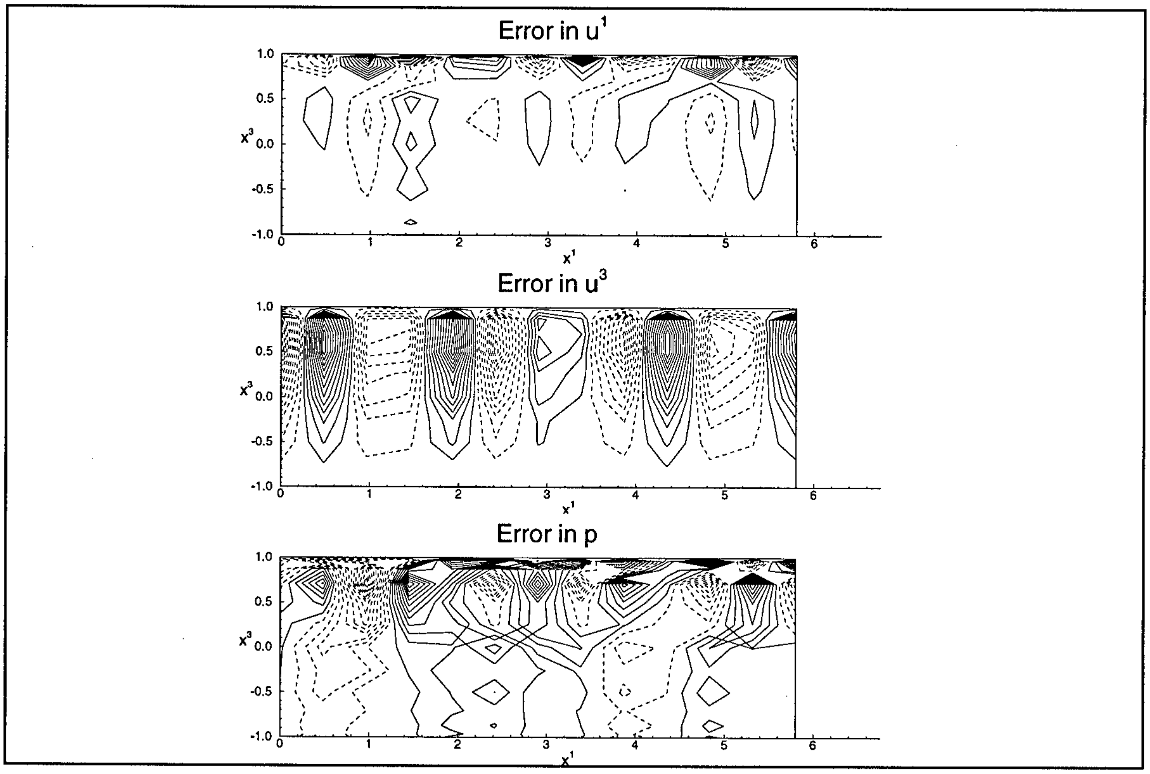

Figure 4.4. Contours of Error in Solution at t=0.01 for Plane Channel, Case B, with N_1=12, N_3=12. The error consists of higher-order Fourier modes neglected in the discretization.

4.1.3. Wall-Normal Accuracy

To determine the truncation error in the Chebyshev collocation method used in the wall-normal discretization, a similar analysis was performed. The steady-state result was obtained by specifying the Case C solution of Tab. 4.1. Contours of this solution are shown in Fig. 4.5. The numerical residual was calculated for a series of values of N_3. Fig. 4.6 shows that spectral accuracy behavior is observed again above N_3 of about 24 and decreases until round-off error becomes dominant, around N_3=44. Increasing the number of grid points above this level begins to introduce increased round-off error.

Again the Reynolds number had no noticeable effect on the truncation error.

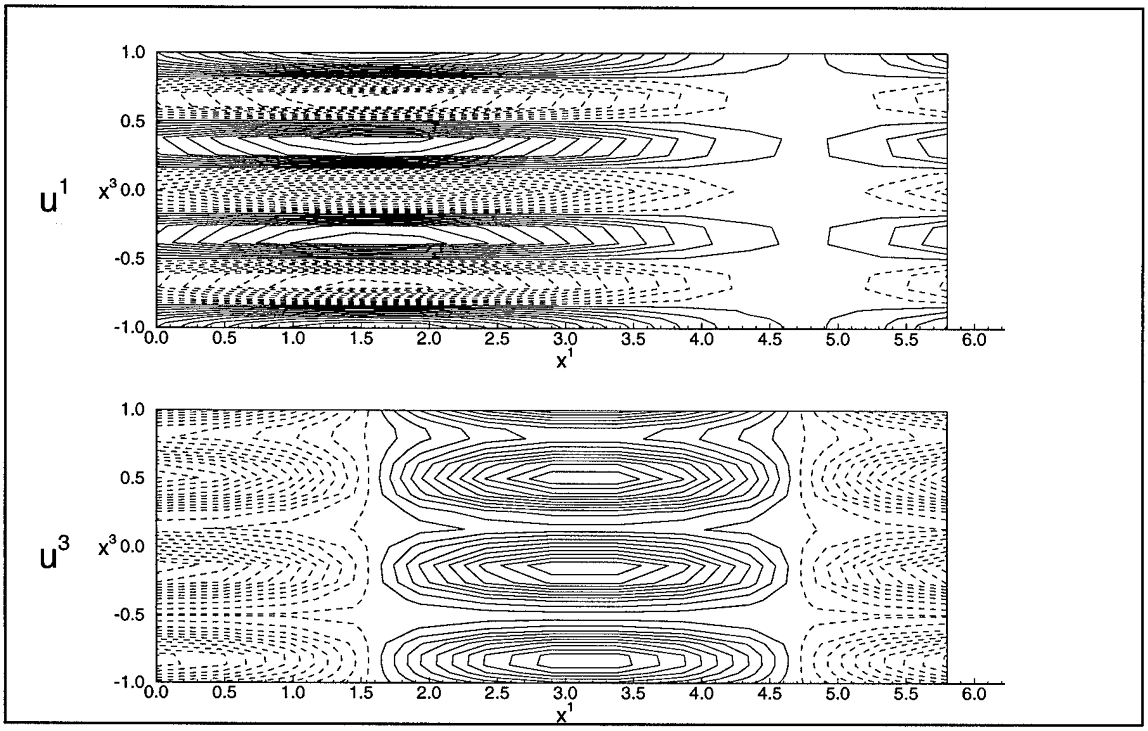

Figure 4.5. Prescribed Solution for Wall-Normal Discretization Analysis of Plane Channel Flow, Case C.

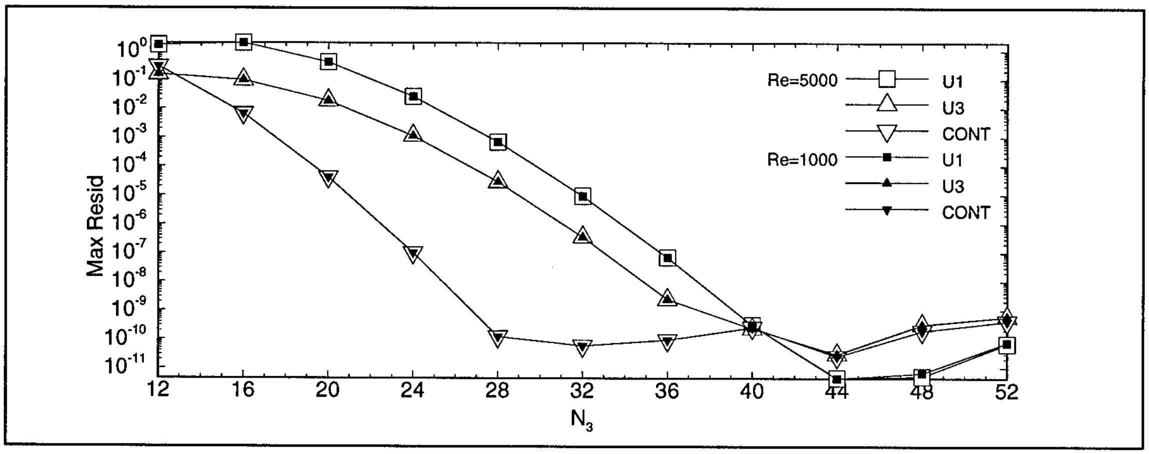

Figure 4.6. Spectral Accuracy is Obtained in the Wall-Normal Discretization for Plane Channel, Case C.

Again, a second result was obtained by specifying a time-dependent solution, shown as Case D in of Tab. 4.1. The error in the solution computed after 10 time steps, with Δt=0.001, is shown in Fig. 4.7. The error in the solution is shown in Fig. 4.8 and demonstrates that discretization error in the wall-normal direction is composed of higher-order polynomial modes. The increased round-off error in the residual for N_3 above 44 results in a slight increase in the error of the solution.

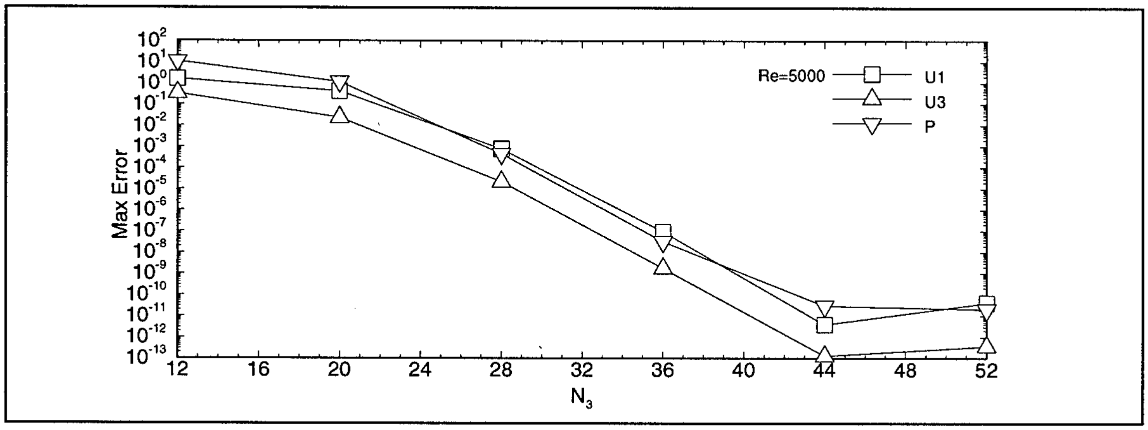

Figure 4.7. Solution Error Due to Wall-Normal Discretization for Plane Channel, Case D.

Cases C and D demonstrate that the Chebyshev discretization has similar truncation error properties as the Fourier discretization. One question that these cases helps to answer is whether or not the interpolation in the wall-normal direction has an adverse effect on the error. The interpolation reduces the accuracy of the continuity equation and the pressure, both of which are staggered with respect to the momentum equation and velocity field. The continuity equation actually had much lower residual than the momentum equations as in the streamwise case, and this is probably due to the fact that the continuity equation is linear. The pressure error is about the same as the error in the streamwise velocity. Therefore, it seems that the interpolation has no noticeable effect on the wall-normal accuracy.

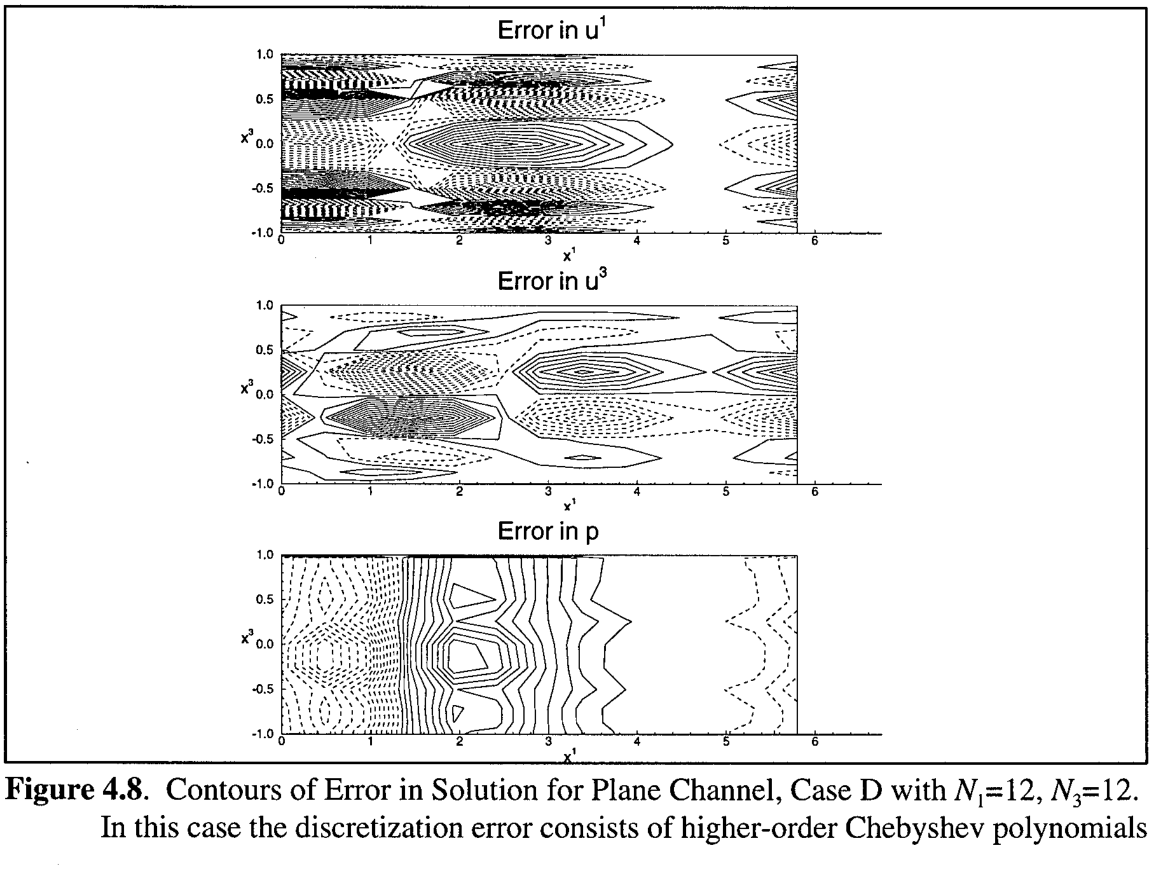
Error in u^1

Error in u^3

Error in p

Figure 4.8. Contours of Error in Solution for Plane Channel, Case D with N_1=12, N_3=12. In this case the discretization error consists of higher-order Chebyshev polynomials

4.1.4. Temporal Accuracy

To assess the accuracy in the temporal discretization, a solution with exponential temporal growth was used. This is Case E. The error in the solution was computed at a time of t=0.01 for a family of time step values. Naturally, the number of time steps required for each test was 0.01/Δt. The grid size used was N_1=12, N_3=12. The prescribed solution at t=0.01 is shown in Fig. 4.9. The solution error at t=0.01 for various values of Δt is shown in Fig. 4.10. The results for error in velocity show that the temporal discretization is second-order accurate, as it should be; the error is linear with a slope of approximately 2 on a log-log plot (two decades of error reduction per decade of time step reduction) down to a time step of 10^{-4}, at which the error was of the order of 10^{-10}.

The analysis yielded erroneous results for pressure for this case, due to an accumulation in the pressure error in the implementation of the forcing function analysis. Therefore the pressure is not shown. This error was noticeable only when a large number of time steps were used, as in the smaller Δt runs in Fig. 4.10. However, the pressure did not show this behavior in other tests, so it is assumed that an inconsistency in the treatment of pressure in the forcing function analysis caused the error accumulation. In any case, this error did not affect the velocity errors, possibly because only the gradient of the pressure is used in the calculations.

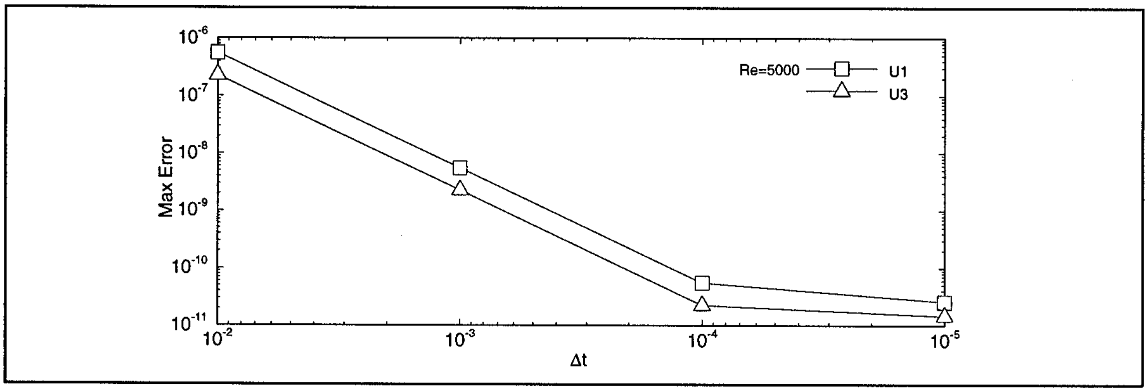

Figure 4.9. Demonstration of Second-Order Accuracy in Time for Plane Channel, Case E.

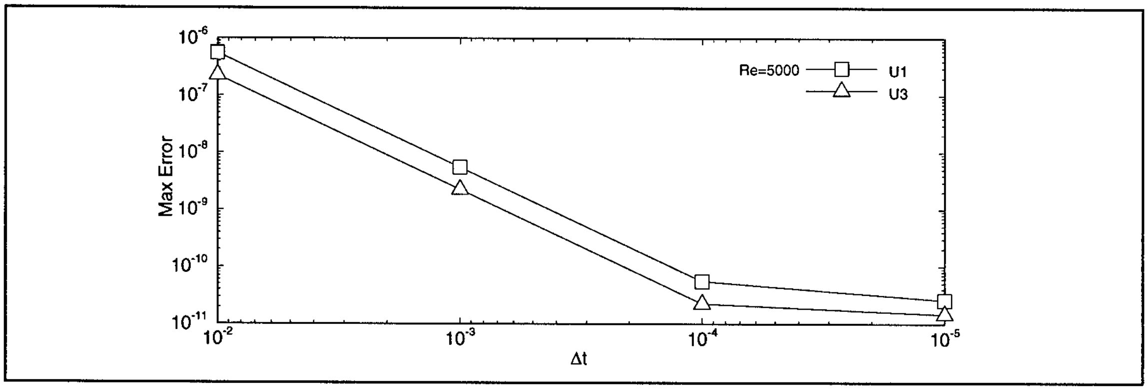

Figure 4.10. Demonstration of Second-Order Accuracy in Time for Plane Channel, Case E.

The temporal error is distributed spatially over the entire domain. To demonstrate this, contours of the error in the solution are shown for Δt=0.001 at t=0.01 in Fig. 4.11. This shows that even if high accuracy is obtained in the spatial discretization, the solution will contain large scale spatially-distributed temporal errors.

This analysis suggests that the second-order accurate time derivative will be sufficient for stability simulations, but could be improved. A reasonable time step for obtaining a solution to a flow problem is of the order of $\Delta t = 0.001$, and many of the

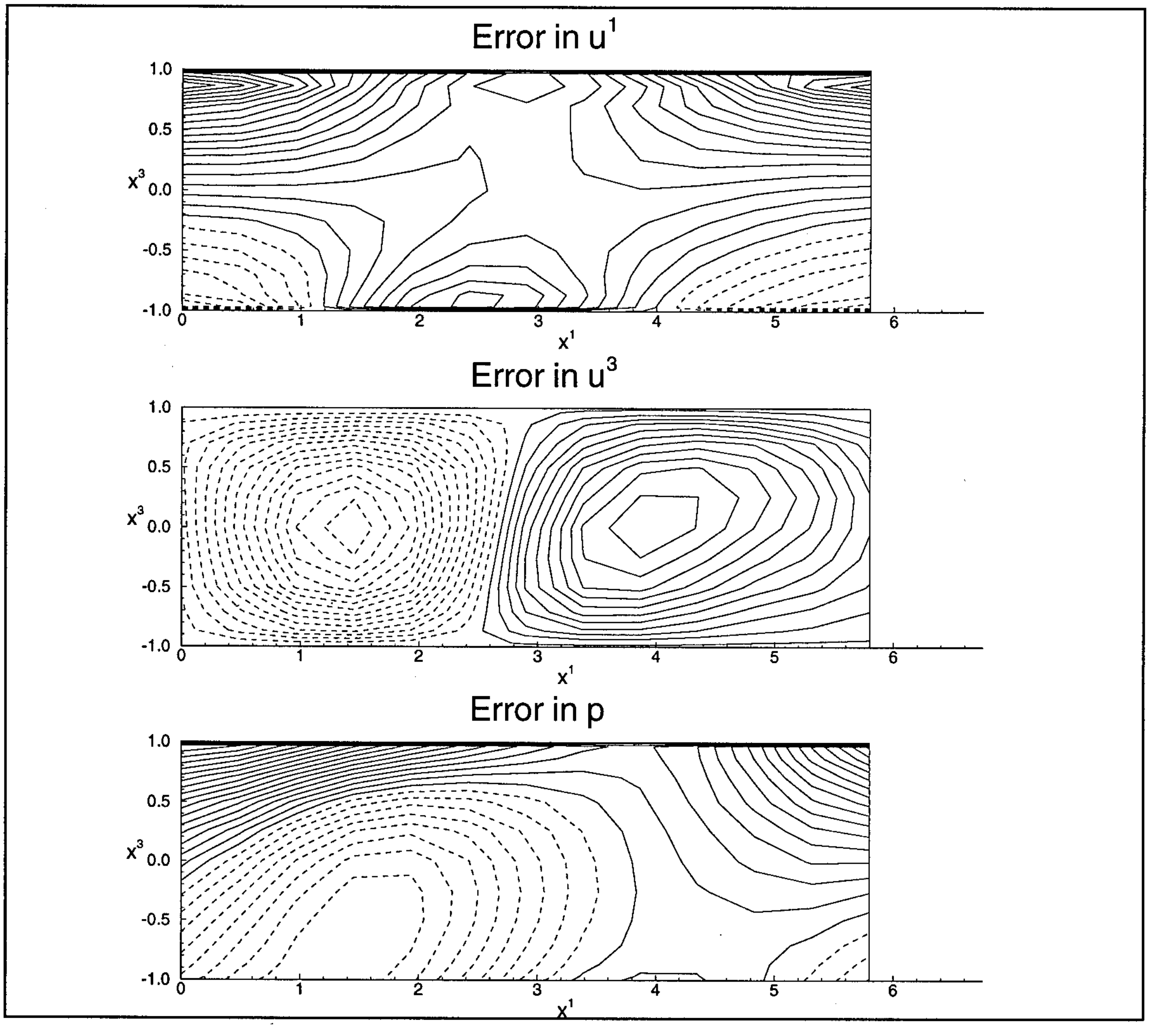

Figure 4.11. Contours of Solution Error at t=0.01 for Plane Channel, Case E. This error is caused solely by the second-order temporal discretization, and demonstrates how temporal errors are distributed spatially.

simulations performed in this study used Δt of 0.01 to 0.025. This study shows that for the temporal error to be as low as the spatial discretization error, a time step on the order of $\Delta t = 10^{-4}$ should be used. However, this proved to require an impractically large number of time steps. With a higher-order method the error properties would probably improve to the level at which the temporal errors matched the spatial errors for reasonable values of Δt. A higher-order method could be implemented by replacing the second-order trapezoidal integration with a fourth-order implicit integration, but it would require the storage of a total of five levels. This modification was not implemented in this study, but is recommended for future work. Though the temporal error is quite small, the fact that it is so larger than the spatial error has some small but noticeable effects on the stability results later in this chapter.

4.1.5. Condition Number Issues

As was seen in the above studies, the accuracy in the spatial discretization can be reduced to the level of machine accuracy (64-bit precision) for a relatively small number of grid points, approximately N=44 for these test cases, compared to other numerical discretization schemes. However, the spectral collocation derivative matrices used in this method are ill-conditioned, and the condition number increases with N^4 (Canuto *et al.* 1988). In addition, in the temporal discretization, all terms except the time derivative term are multiplied by $1/\Delta t$. Thus the condition number of the temporally discrete system also increases with $1/\Delta t$. In the remainder of this study, the number of points used does not exceed $N_1=8$, $N_3=64$, and the smallest time step used for the cases studied was of the order of 10^{-3}. The previous results suggest that for these values, the ill-conditioning of the discrete system will not adversely affect the solutions obtained. However, in future phases of this study, more than 64 points may be needed in the wall-normal direction, as highly nonlinear interactions lead to breakdown of the flow structures. It would be desirable to remedy the round-off error growth problems to a level at which 128 points could be used in the wall-normal direction.

The condition number of the implicit coefficient matrix, $\boldsymbol{B}$, in Eq. (3.40) simply reflects the stiffness of the spectral discretization. A new method of solving the same discrete system would have the same difficulties with ill-conditioning. The only solution is to find ways to reduce the round-off error accumulation in the solution through the use of higher precision computations. It is possible to reduce round-off error in the computation of the coefficient matrix and in obtaining the linear algebra solution at each iteration by rearranging terms and operations to minimize loss of precision. However, once this has been done, higher precision arithmetic must be used in key areas in which precision is being lost. The key sources of round-off error should be sought out, and selective use of higher precision arithmetic should be used when necessary to reduce round-off error accumulation.

4.2. Comparison to Linear Stability Theory for Plane Channel Flow

The analysis in §4.1 served to validate and examine the numerical formulation and its implementation in the two-dimensional code. Subsequently, the ability of the code to reproduce linear stability results for the plane channel case was examined. A Tollmien-Schlichting wave was generated for the initial condition as described in §3.4.1. The amplitude of the wave was selected as $A_1=10^{-5}$. For this small amplitude, it was expected that linear stability theory would correctly predict the time evolution of the wave as the solution was integrated forward in time from the initial condition. Two plane channel cases were considered and are shown as Case 1 and Case 2 in Tab. 4.2. Case 1, with a streamwise wavenumber of $\alpha=1.0$ and a Reynolds number of $Re=8{,}000$, has a small positive growth rate and is therefore slightly unstable. Case 2, on the other hand, with $\alpha=1.25$ and $Re=4{,}000$ has a negative growth rate and is stable.

Case	*Re*	α	R_c	ω_R	ω_Ix1,000	*T*
1	8,000	1.0	plane	0.247075	2.66417	25.4302
2	4,000	1.25	plane	0.381718	-10.9228	16.4603
3	5,000	100	100	0.374757	3.28679	16.7660
4	4,000	5,000	10,00	0.530779	-16.5727	11.8376

Table 4.2. Temporal Stability Simulation Test Cases. The linear stability results were obtained from Herbert (1988a) and gives the complex eigenvalue $\omega=\omega_R+i\omega_I$, where ω_R is the temporal frequency and ω_I is the temporal growth rate. The period *T* is $2\pi/\omega_R$.

The solution was then obtained for a single period of the Tollmien-Schlichting wave and compared with linear stability theory. In addition, the grid resolution in the wall-normal direction, the time step, and the amplitude of the initial disturbance were varied parametrically, and the results were compared with linear stability theory.

4.2.1. Linear Stability Theory Results

The Tollmien-Schlichting wave is an eigenmode of the linearized governing equations expanded in a Fourier series in the streamwise direction. For a particular set of flow parameters *Re* and α, a finite number of discrete eigenmodes and eigenvalues of the linearized system exist. The eigenmode with the least stable eigenvalue (with the maximum imaginary part) is selected as the primary mode. Using the linear stability code of Herbert (1988a) with N_3=64, the most stable eigenmode was determined for Case 1 and Case 2. The resulting eigenvalues are shown in Tab. 4.2. The eigenvalue $\omega=\omega_R + i\omega_I$ consists of the temporal frequency, ω_R, and the growth rate ω_I. The complex mode shapes are shown in Fig. 4.12 and Fig. 4.13 for Case 1 and Case 2, respectively. To obtain the Tollmien-Schlichting wave initial condition, the mode profiles were used in conjunction with Eq. (3.53). Contours of Cartesian velocity components and pressure are shown in Fig. 4.14 for Case 1 and Fig. 4.15 for Case 2. All solutions shown in this chapter are for disturbance quantities only, unless otherwise stated. The solution was computed, using N_3=64, Δt=$10^{-3}\,T$, for a single period of the Tollmien-Schlichting wave. Results are shown at t=0.1T and t=T for Case 1 in Figs. 4.16 and 4.17. The kinetic energy of the disturbance was computed using Eq. (3.63). In Fig. 4.18 this is compared with the growth predicted by linear theory, which is given by:

$$\frac{E_1(t)}{E_1(0)} = e^{2\omega_I t} \tag{4.4}$$

These results show the 2-D structure of Tollmien-Schlichting waves in plane channel flow. As time progresses, the entire wave solution convects through the domain. After one period, the disturbance contours look exactly the same as the initial Tollmien-Schlichting wave disturbance. However, the amplitude of the wave has grown a small amount as is evident in the increase of kinetic energy. The solution closely matches the predictions of linear theory, as can be seen in Fig. 4.18. The slight error in the numerical solution can be resolved by using a smaller time step; however, a time step of Δt=$10^{-3}\,T$ is already being used, and using a lower time step would be prohibitively expensive in computer time. This problem is was also observed in the forcing function analysis of §4.1. To improve the accuracy of the temporal resolution without reducing the time step, a higher-order discretization in time should be used.

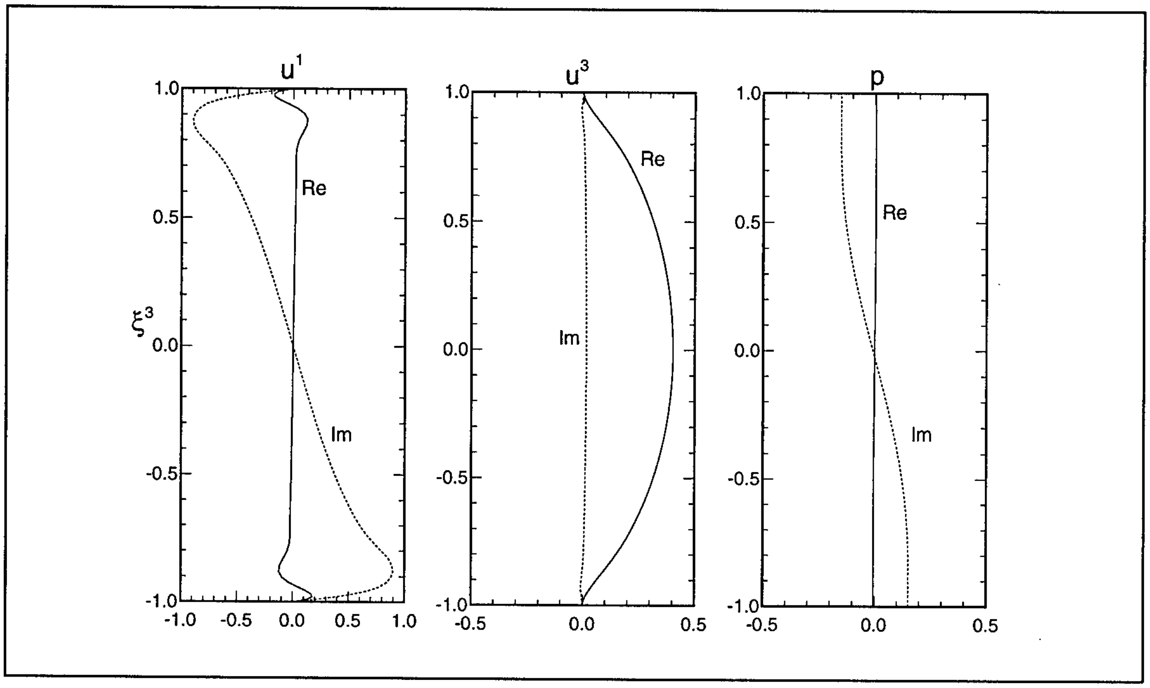

Figure 4.12. Mode Shapes for Plane Channel, Case 1.

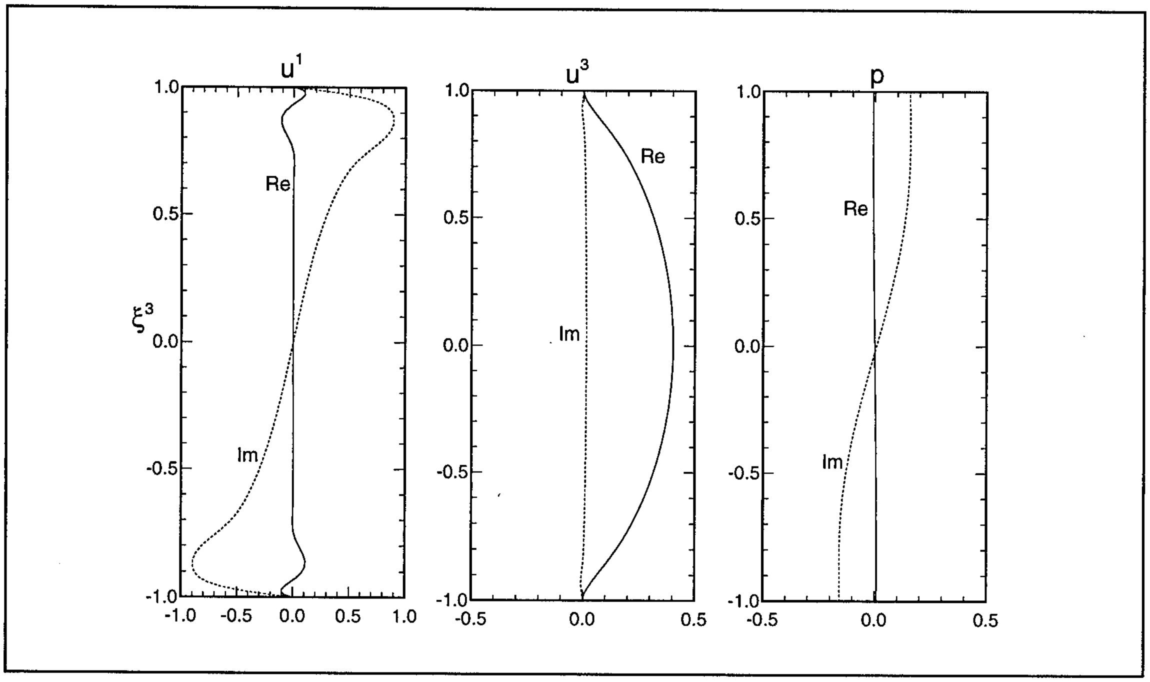

Figure 4.13. Mode Shapes for Plane Channel, Case 2.

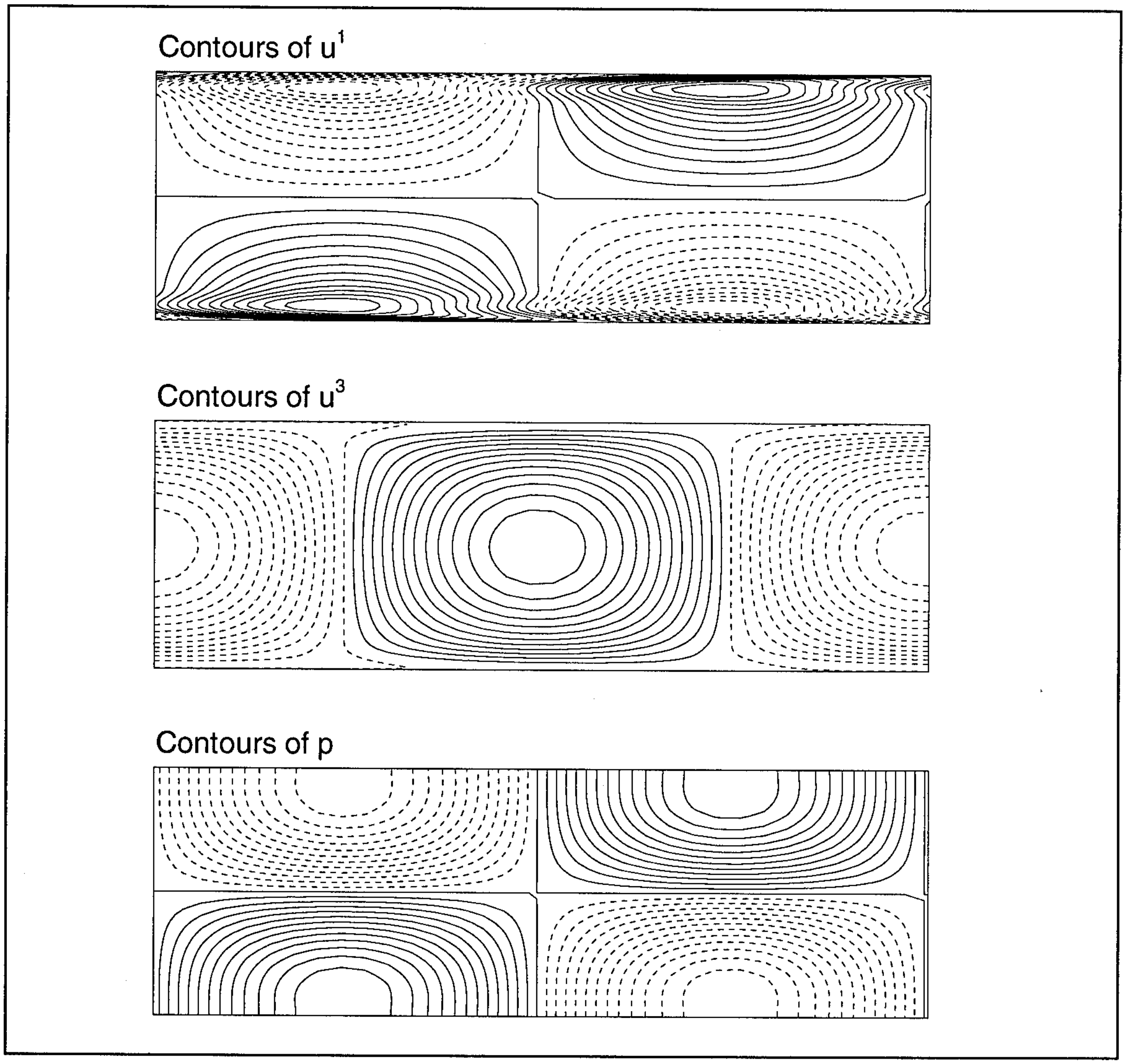

Figure 4.14. Contours of Disturbance Quantities for Plane Channel, Case 1.

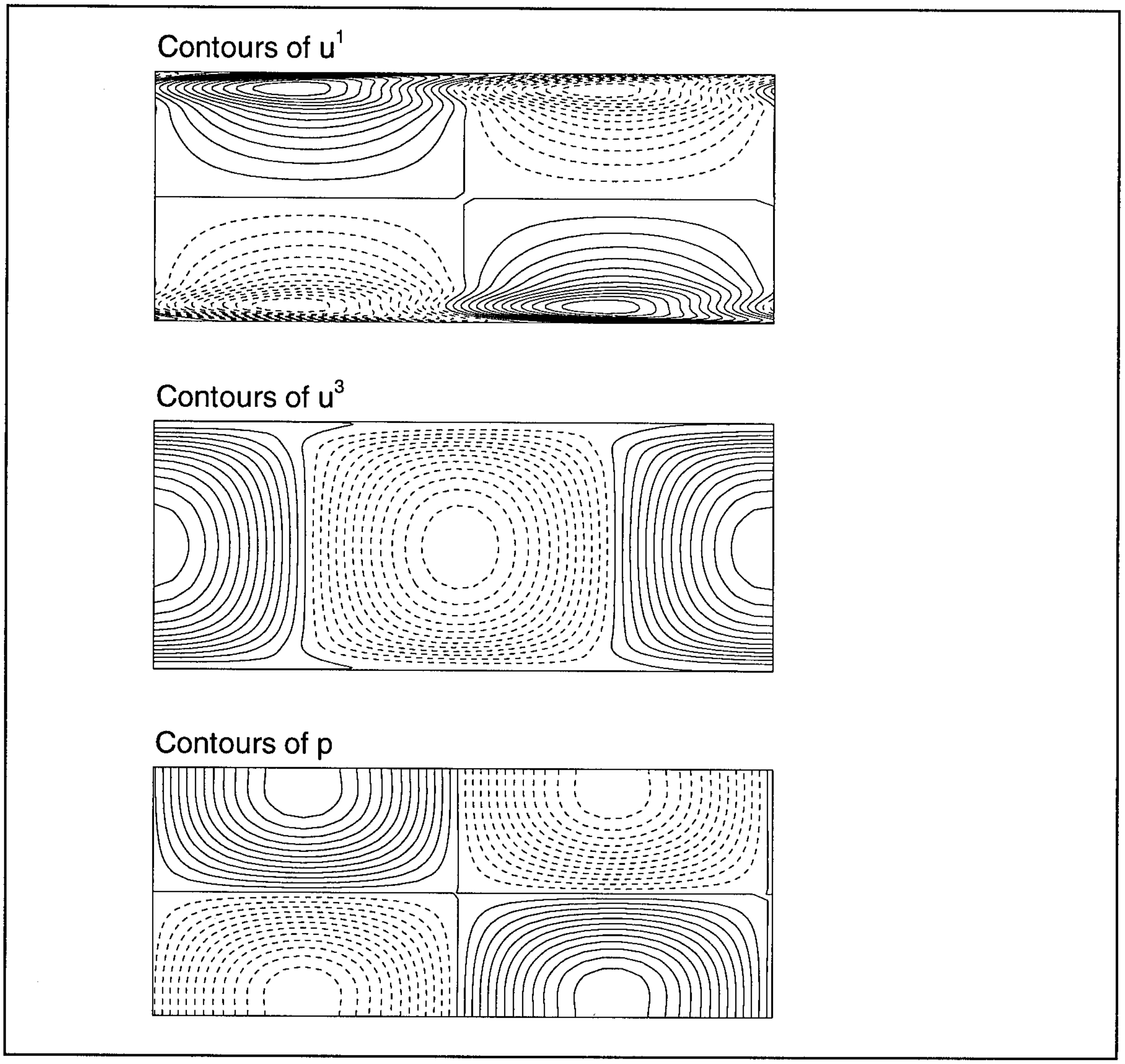

Figure 4.15. Contours of Disturbance Quantities for Plane Channel, Case 2.

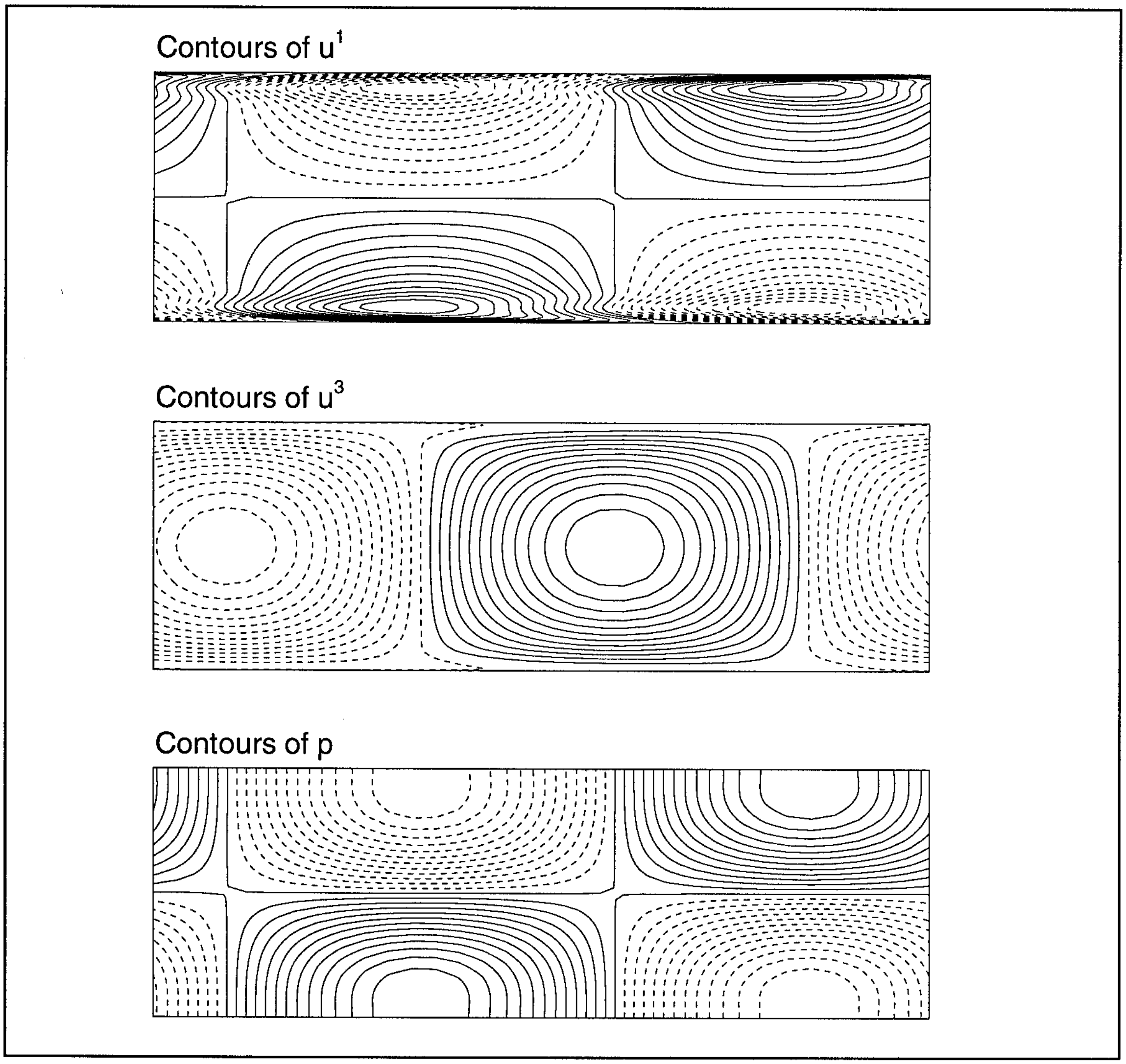

Figure 4.16. Contours of Disturbance u^3 for Plane Channel, Case 1, t=0.1T.

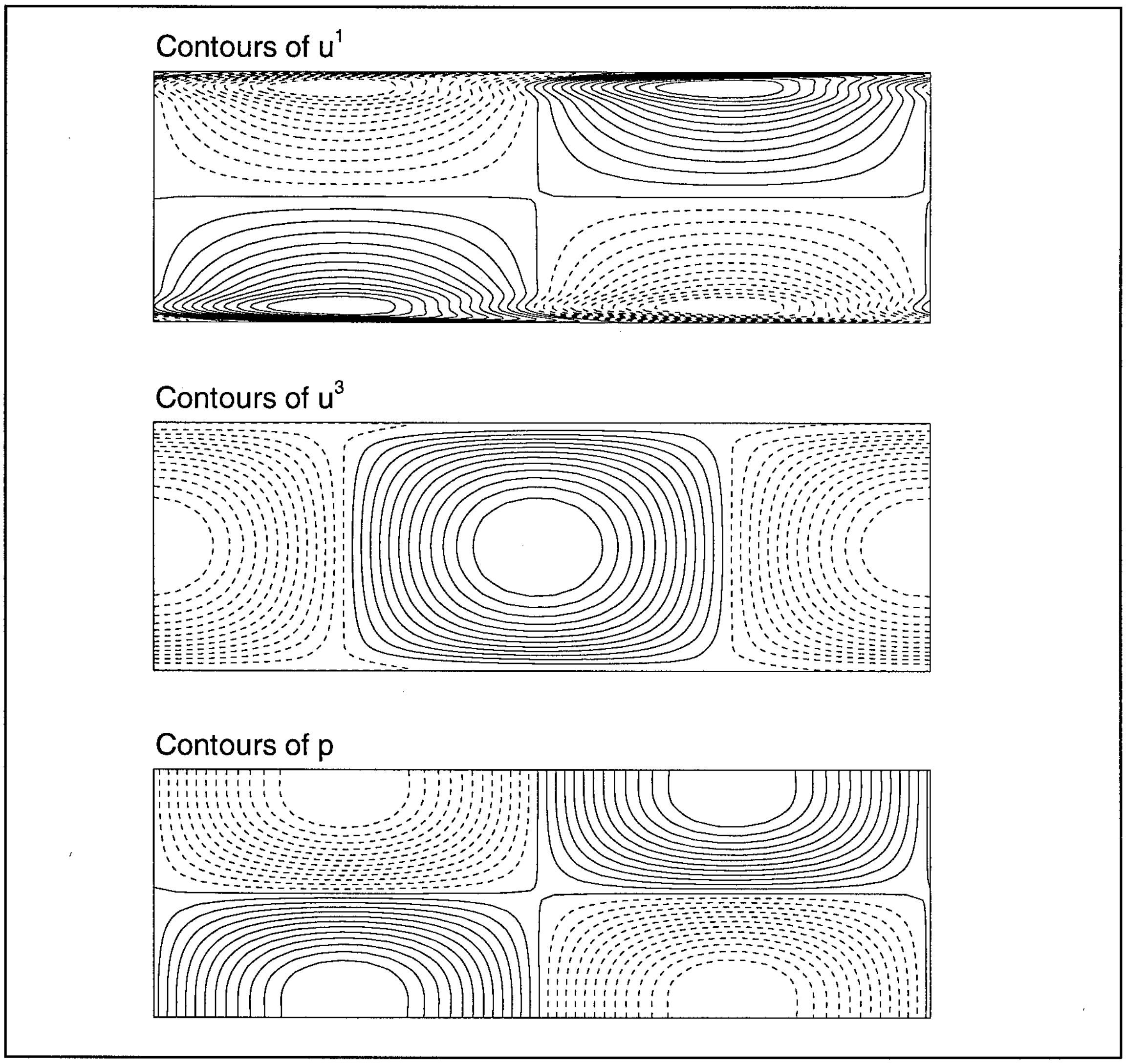

Figure 4.17. Contours of Disturbance u^3 for Plane Channel, Case 1, t=1.0T.

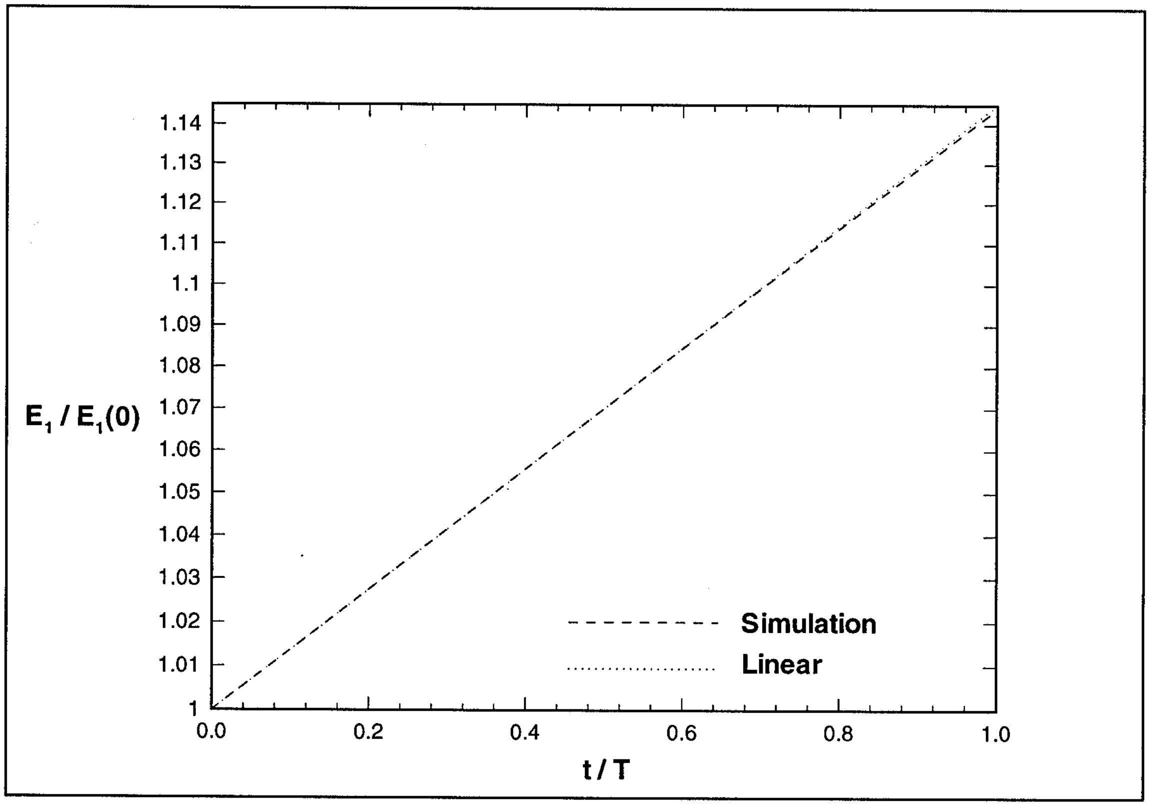

Figure 4.18. Growth of Disturbance Mode Kinetic Energy Compared to Linear theory, Plane Channel, Case 1.

4.2.2. Temporal Analysis Results

The computed solution was analyzed to determine the numerical values of the temporal frequency ω_R and growth rate ω_I using the method of §3.5. In this method, the solution velocity field is transformed into Fourier space in the streamwise direction. Then the kinetic energy and the integrated normal velocity component are used to determine the growth rate and rate of oscillation of each Fourier component. Below, the growth rate and rate of oscillation of the primary mode are compared to linear theory. The analysis was repeated for a family of values of N_3, with Δt=0.001 and with amplitude of the primary mode, $A_1=10^{-5}$. These results are shown in Figs. 4.19 and 4.20 and are summarized in Tab. 4.3.

A similar study was performed with varying values of Δt. These results are shown in Figs. 4.21 and 4.22 and are summarized in Tab. 4.4. They show that the temporal frequency and growth rate are not sensitive to the time step. The exception is that the growth rate computation based on kinetic energy loses precision for Δt of 10^{-5} or smaller. This is due to the fact that the kinetic energy growth rate is computed from the square of a small number and loses digits of precision.

Finally, a study was performed to determine the effect of disturbance amplitude on the predicted linear growth. A family of initial disturbance amplitudes was used with $\Delta t=0.001$ and $N_3=48$. The results are shown in Figs. 4.23 and 4.24 and are summarized in Tab. 4.4. They demonstrate that amplitudes of 0.1 or higher are needed before the initial growth of the wave deviates from the prescription of linear theory.

These results are significant in that they demonstrate the limits of the numerical scheme. Spatial resolution in the wall-normal direction is critical; at least $N_3=48$ points are needed. A time step of $\Delta t=0.01$ or smaller should be used. Finally, a disturbance of amplitude $A_1=10^{-2}$ or smaller should be used. Using very small amplitudes ($A_1=10^{-5}$) did not seem to cause any numerical problems. Finally, it is observed that the eigenvalue results from linear theory can be matched very closely with the present numerical scheme, when the simulation proceeds within the ranges demonstrated in this analysis.

	Case 1, Re=8,000			Case 2, Re=4,000		
N_3	ω_R	$\omega_I\ (f_1)$ x1,000	$\omega_I\ (E_1)$ x1,000	ω_R	$\omega_I\ (f_1)$ x1,000	$\omega_I\ (E_1)$ x1,000
24	0.247146	2.74013	2.66176	0.381416	-10.6454	-10.9411
32	0.247118	2.66204	2.66512	0.381698	-10.8633	-10.9232
40	0.247080	2.66077	2.66448	0.381715	-10.9185	-10.9228
48	0.247076	2.66407	2.66445	0.381718	-10.9228	-10.9228
56	0.247075	2.66449	2.66443	0.381718	-10.9229	-10.9228
exact	0.247075	2.66417	2.66417	0.381718	-10.9228	-10.9228

Table 4.3. Effect of Spatial Resolution on Computed Temporal Frequency ω_R and Temporal Growth Rate ω_I for Plane Channel. Note that two different methods of computing the temporal growth rate were used. The first method uses the integral of the normal velocity component, while the second uses the kinetic energy. See §3.5 for details.

	Case 1, Re=8,000			Case 2, Re=4,000		
Δt	ω_R	$\omega_I\ (f_1)$ x1,000	$\omega_I\ (E_1)$ x1,000	ω_R	$\omega_I\ (f_1)$ x1,000	$\omega_I\ (E_1)$ x1,000
10^{-1}	0.247063	2.66400	2.66431	0.381672	-10.9182	-10.9175
10^{-2}	0.247075	2.66412	2.66441	0.381718	-10.9228	-10.9227
10^{-3}	0.247076	2.66407	2.66445	0.381718	-10.9228	-10.9228
10^{-5}	0.247076	2.66407	2.66747	0.381718	-10.9228	-10.9231
exact	0.247075	2.66417	2.66417	0.381718	-10.9228	-10.9228

Table 4.4. Effect of Temporal Resolution on Computed Temporal Frequency ω_R and Temporal Growth Rate ω_I for Plane Channel.

	Case 1, Re=8,000			Case 2, Re=4,000		
A_1	ω_R	$\omega_I\,(f_1)$ x1,000	$\omega_I\,(E_1)$ x1,000	ω_R	$\omega_I\,(f_1)$ x1,000	$\omega_I\,(E_1)$ x1,000
10^{-0}	0.247078	2.64580	2.64174	0.381719	-10.9531	-10.9713
10^{-1}	0.247076	2.66399	2.66419	0.381718	-10.9231	-10.9233
10^{-2}	0.247076	2.66407	2.66441	0.381718	-10.9228	-10.9228
10^{-3}	0.247076	2.66407	2.66441	0.381718	-10.9228	-10.9228
exact	0.247075	2.66417	2.66417	0.381718	-10.9228	-10.9228

Table 4.5. Effect of Disturbance Amplitude on Computed Temporal Frequency ω_R and Temporal Growth Rate ω_I for Plane Channel.

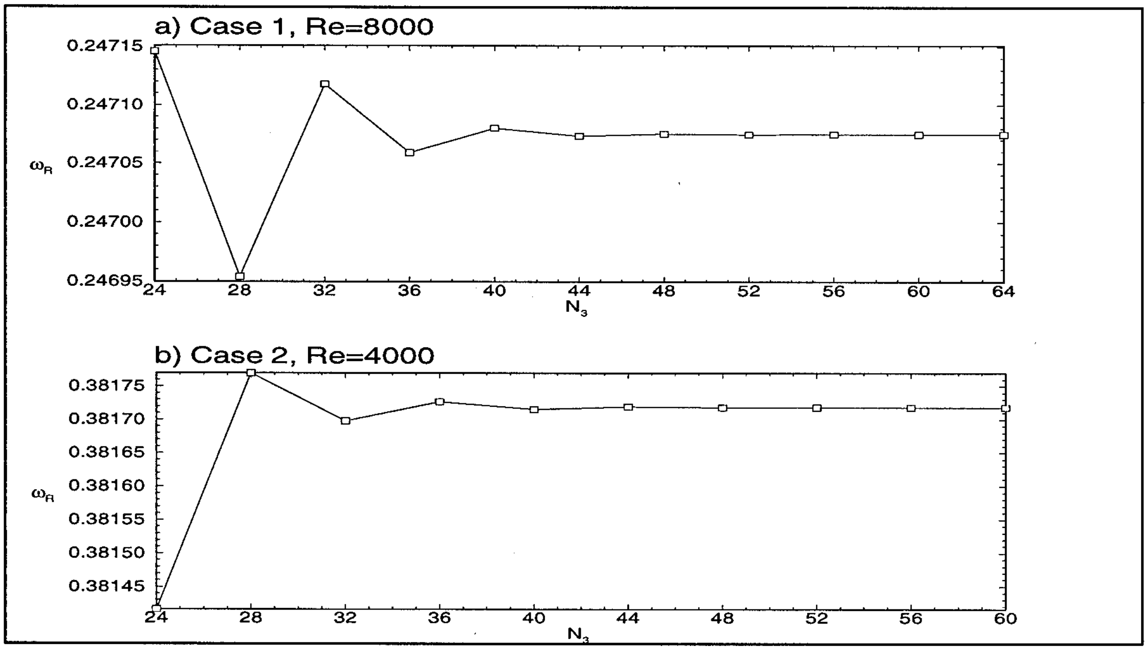
a) Case 1, Re=8000

b) Case 2, Re=4000

Figure 4.19. Effect of Spatial Resolution on Computed Linear Frequency, ω_R, for a) Case 1, and b) Case 2.

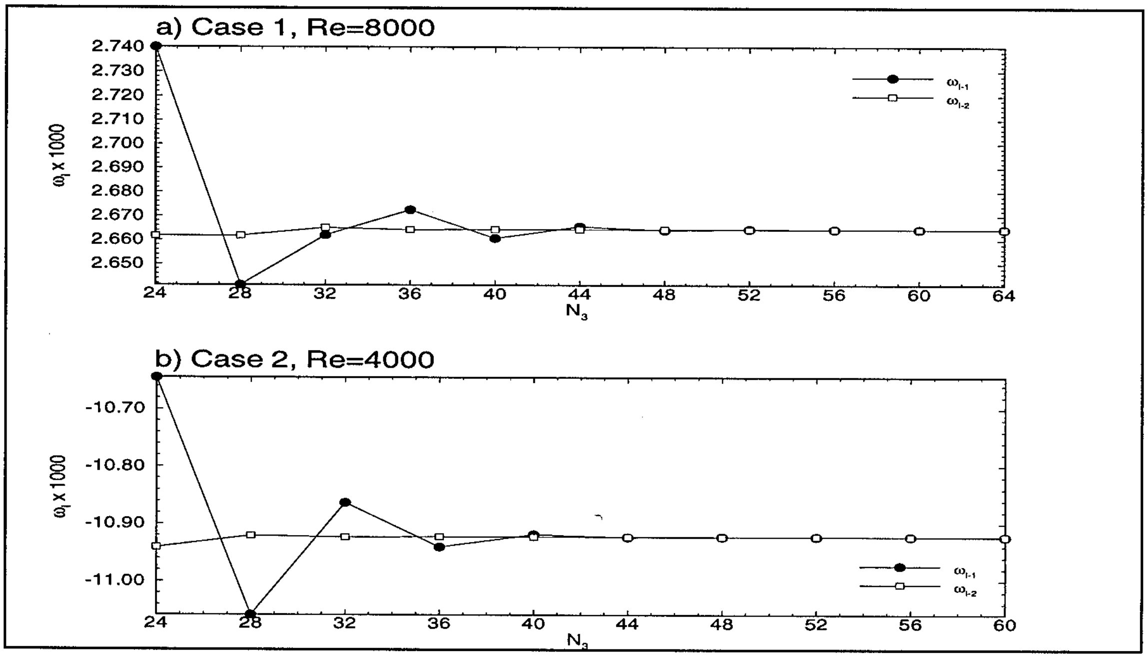

Figure 4.20. Effect of Spatial Resolution on Computed Linear Growth Rate, ω_I, for a) Case 1, and b) Case 2. The solid symbols show values computed from $f_1(\xi^1)$ and the hollow symbols are computed from $E_1(\xi^1)$.

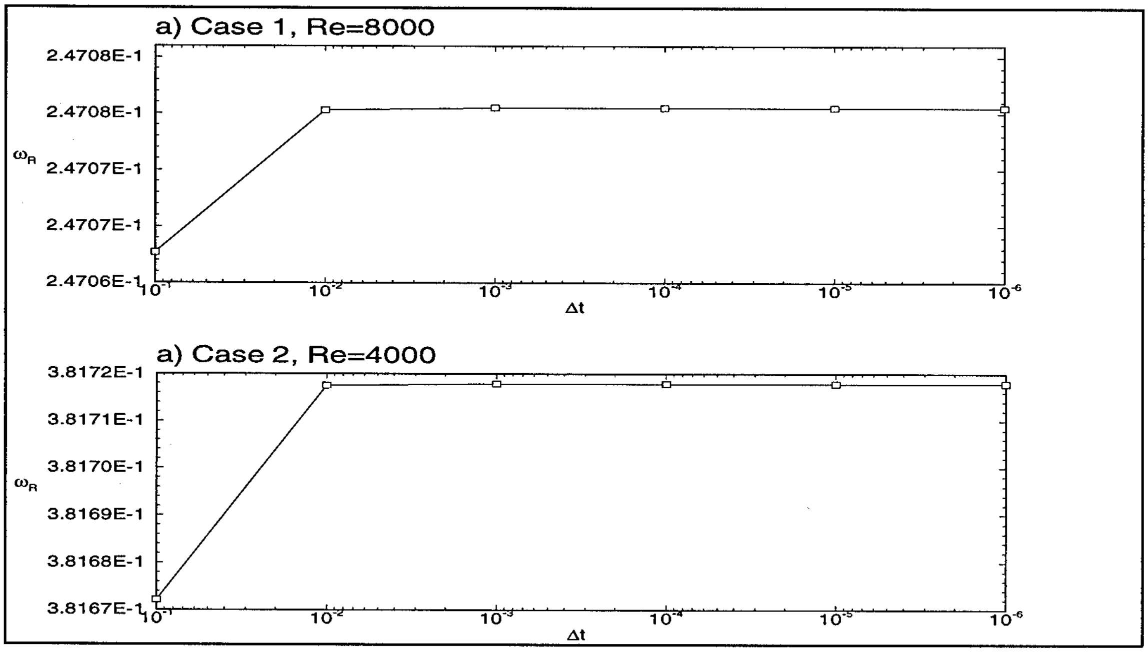

Figure 4.21. Effect of Temporal Resolution on Computed Linear Frequency, ω_R, for a) Case 1, and b) Case 2.

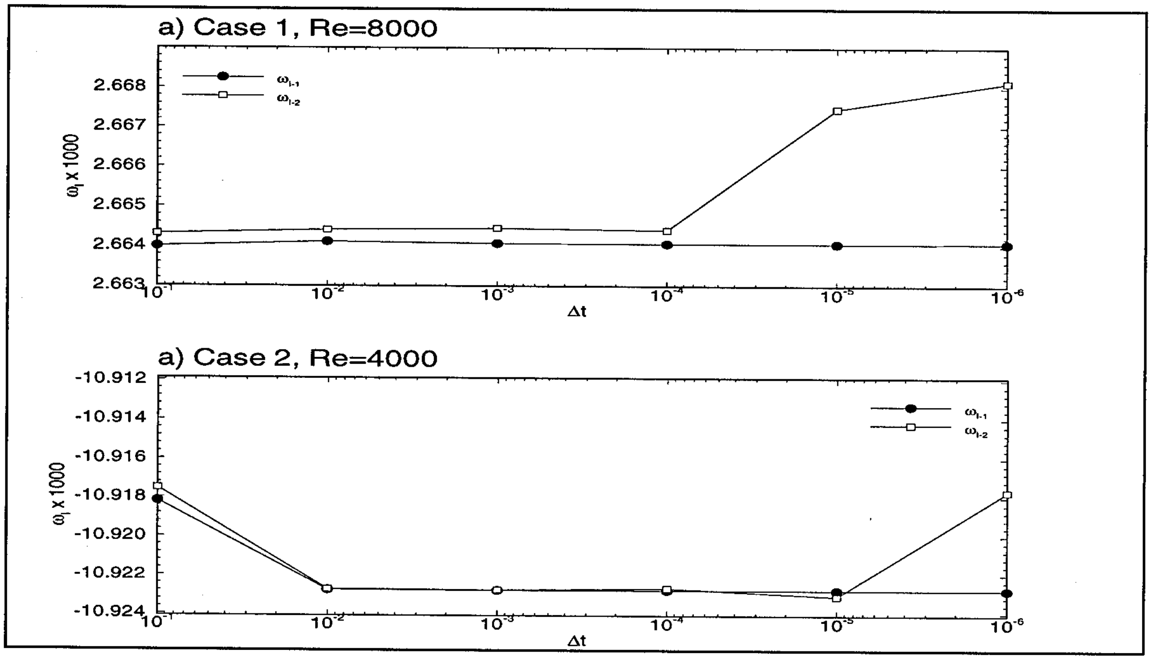

Figure 4.22. Effect of Temporal Resolution on Computed Linear Growth Rate, ω_I, for a) Case 1, and b) Case 2. The solid symbols show values computed from $f_1(\xi^1)$ and the hollow symbols are computed from $E_1(\xi^1)$.

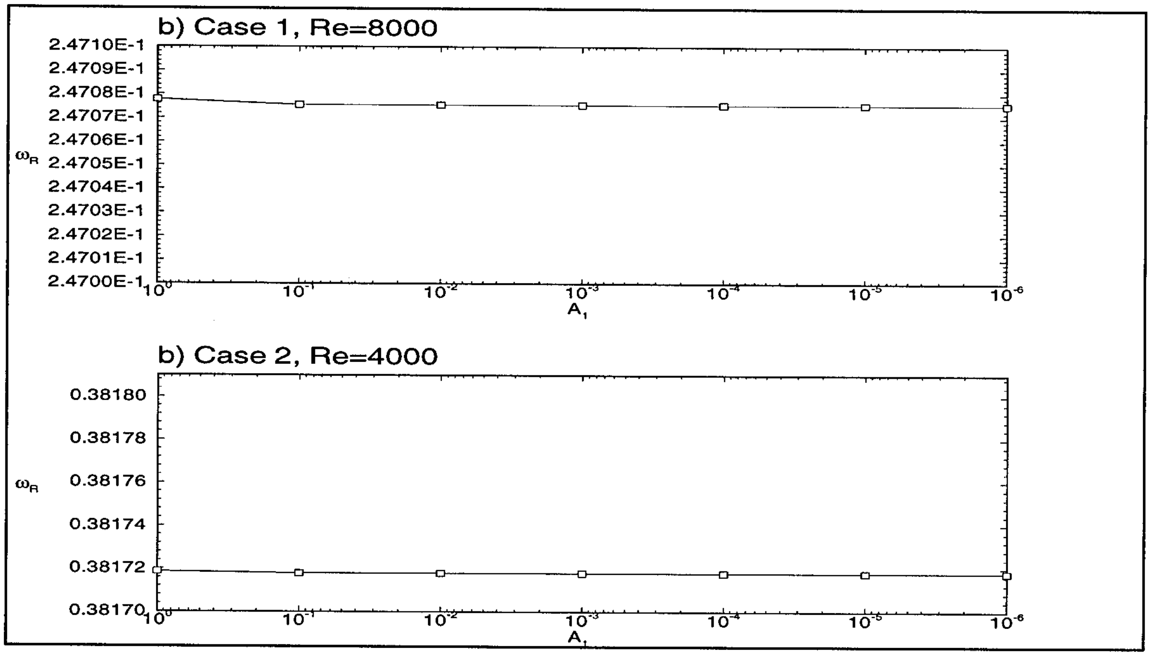

Figure 4.23. Effect of Disturbance Amplitude on Computed Linear Frequency, ω_R, for a) Case 1, and b) Case 2.

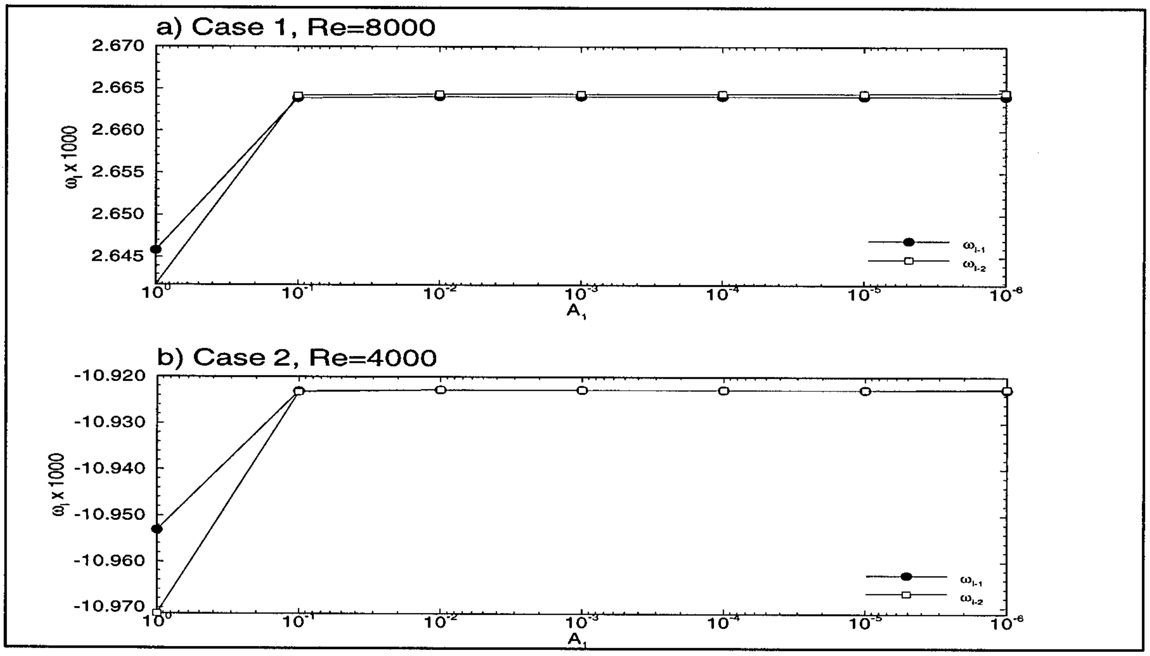

Figure 4.24. Effect of Disturbance Amplitude on Computed Linear Growth Rate, ω_I, for a) Case 1, and b) Case 2. The solid symbols show values computed from $f_1(\xi^1)$ and the hollow symbols are computed from $E_1(\xi^1)$.

4.3. Comparison to Linear Stability Theory for Curved Channel Flow

Linear stability results were also obtained for curved channel flows. Cases 3 and 4, summarized in Tab. 4.2, were used to determine the accuracy of the linear stability calculations for the curved channel geometry. Case 3, with *Re*=5,000 and R_c =100 is unstable due to the curvature of the geometry (the plane channel case with the same parameters is stable). Case 4, with *Re*=4,000 and R_c =1,000 is stable. It is similar to Case 2 and will serve as a useful demonstration of the effects of slight curvature. The results are similar to those for the plane channel.

4.3.1. Linear Stability Theory Results

The eigenvalues for Cases 3 and 4 are shown in Tab. 4.2. The polar velocity component and pressure mode shapes are shown in Fig. 4.25 for Case 3 and in Fig. 4.26 for Case 4. The mode profiles were used to calculate the curved channel Tollmien-Schlichting waves using Eq. (3.56). Contours of the disturbance polar velocity components, u^θ and u^r, along with the pressure p, are shown in Fig. 4.27 for Case 3 and Fig. 4.28 for Case 4. Again, the solution was computed, using N_3=64, Δt=$10^{-3}T$, for a single period of the Tollmien-Schlichting wave. The kinetic energy of the disturbance mode was also calculated and is compared to the kinetic energy predicted by linear theory. This is shown in Fig. 4.29.

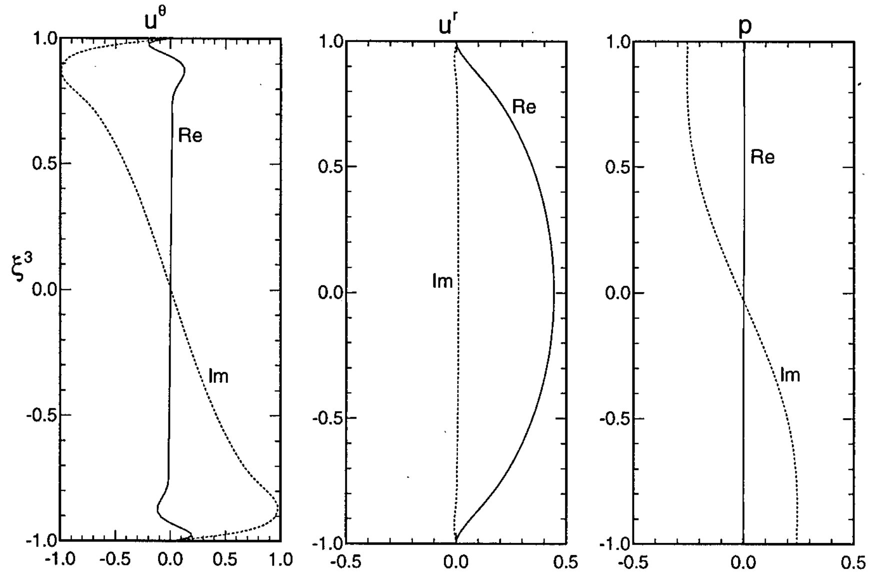

Figure 4.25. Mode Shapes for Curved Channel, Case 3.

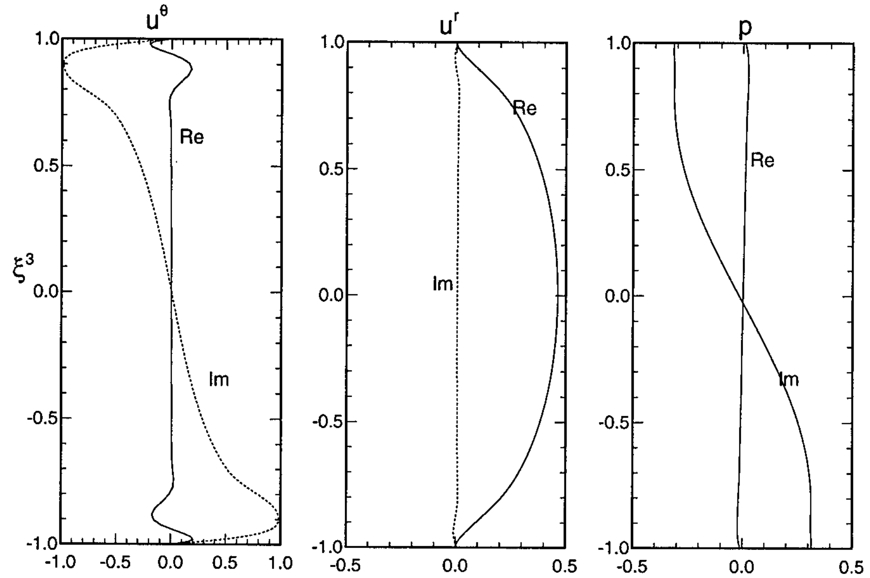

Figure 4.26. Mode Shapes for Curved Channel, Case 4.

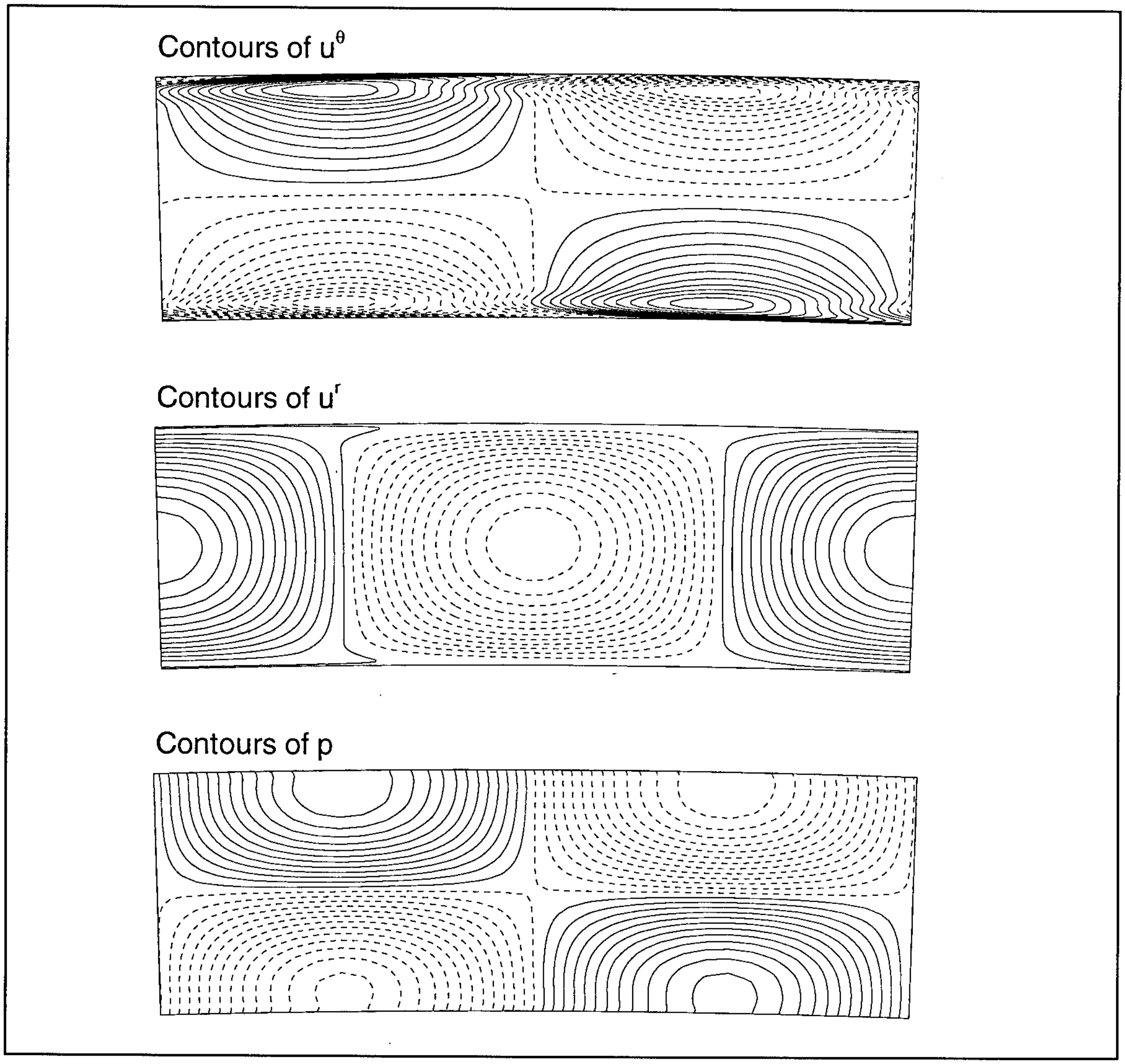

Contours of u^θ

Contours of u^r

Contours of p

Figure 4.27. Disturbance Quantities for the Tollmien-Schlichting Wave Initial Condition for the Curved Channel, Case 3.

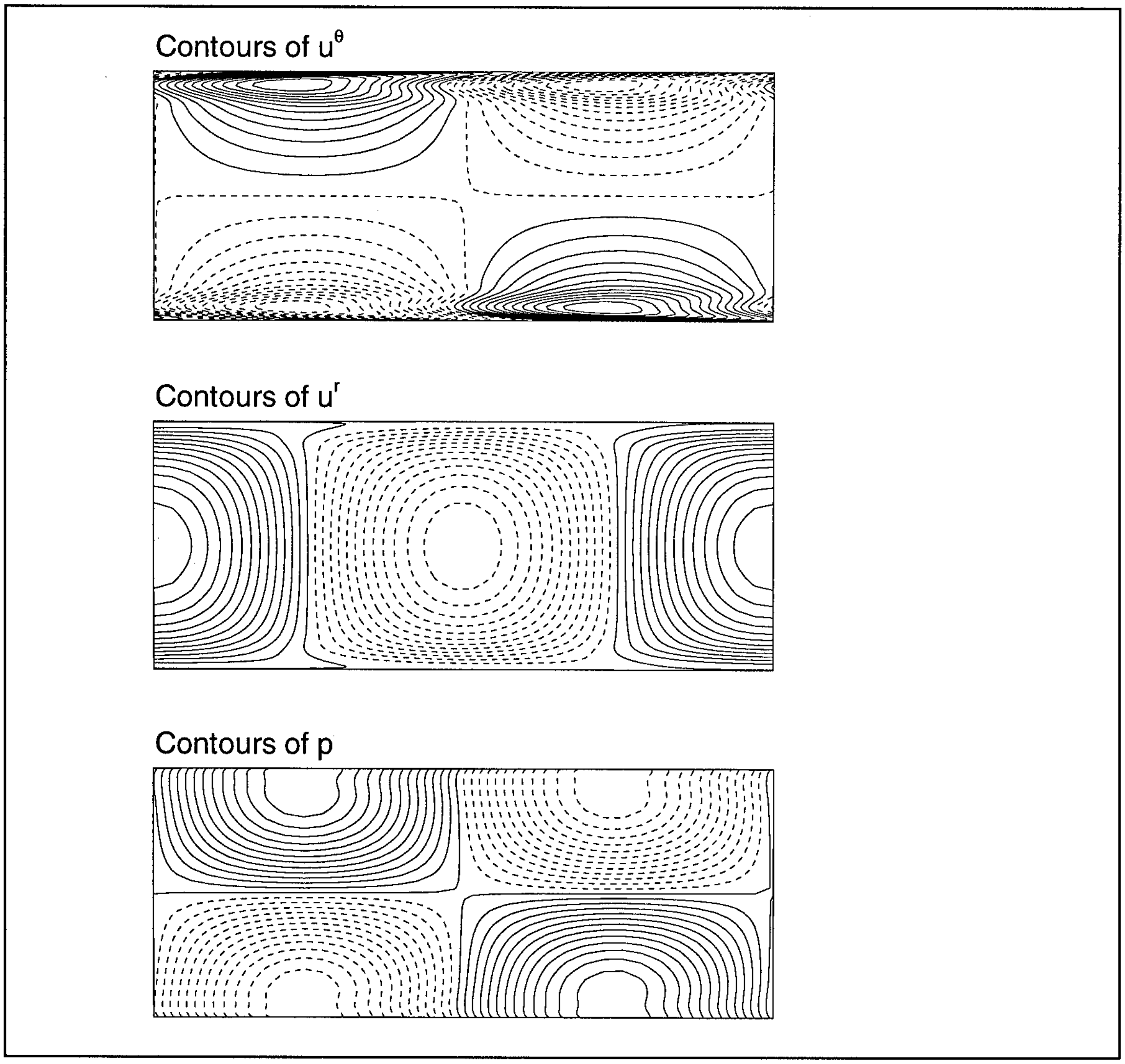

Contours of u^{θ}

Contours of u^{r}

Contours of p

Figure 4.28. Disturbance Quantities for the Tollmien-Schlichting Wave Initial Condition for the Curved Channel, Case 4.

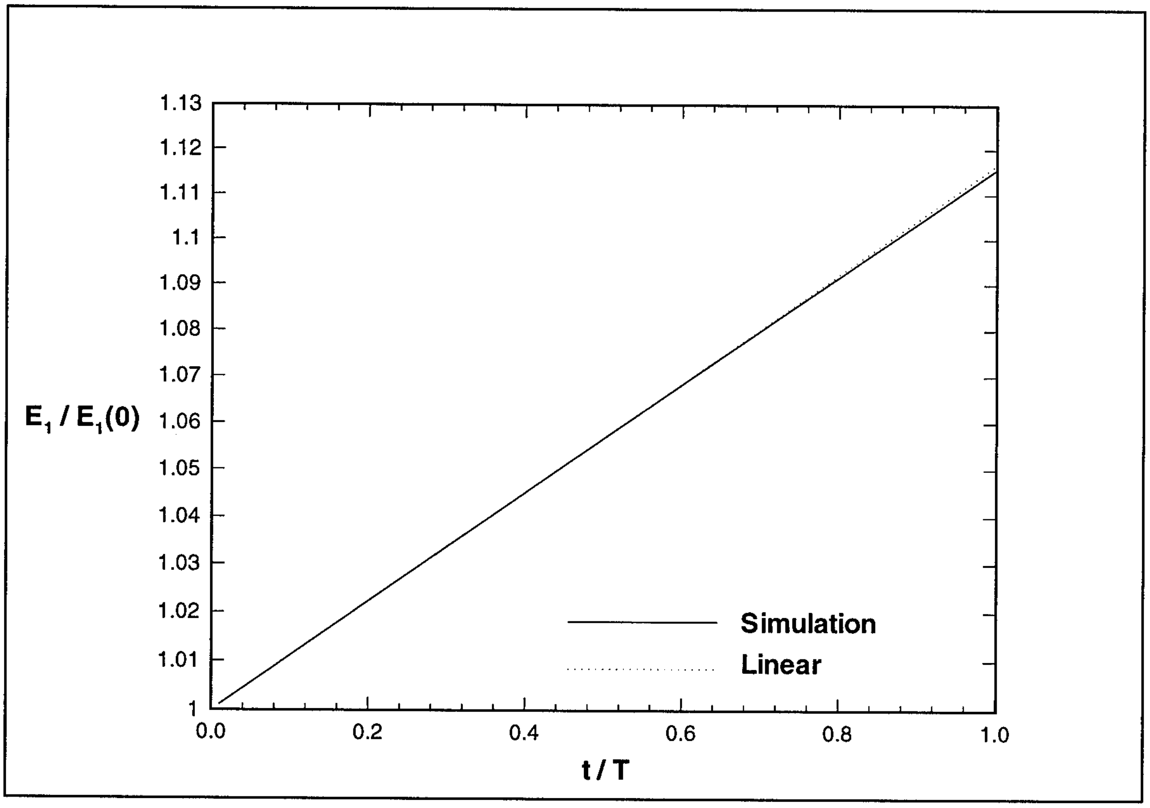

Figure 4.29. Disturbance kinetic energy for one period *T* for Curved Channel, Case 3. Numerical simulation is shown as dashed line, linear stability solution shown as dotted line.

4.3.2. Temporal Analysis Results

The computed solution was analyzed to determine the numerical values of the temporal frequency ω_R and growth rate ω_I for the curved channel as was done for the plane channel in §4.2.2. The spectral analysis of §3.5 was used to obtain results for a family of values of N_3 with Δt=0.001, A_1=10^{-3}. These results are shown in Figs. 4.30 and 4.31 and are summarized in Tab. 4.6.

The results were also obtained for varying values of Δt with N_3=48, A_1=10^{-3}. These results are shown in Figs. 4.32 and 4.33 and are summarized in Tab. 4.7. Again the growth rate ω_I is more sensitive to resolution than the temporal frequency ω_R.

Finally, a family of initial disturbance amplitudes was used with N_3=48, Δt=10^{-3}. The results are shown in Figs. 4.34 and 4.35 and are summarized in Tab. 4.8.

These studies confirm that the stability solutions for curved channel flow behave much the same as those for plane channel flow. However, in some cases, as few as three four digits of accuracy are obtained in either the temporal frequency and growth rate when the normal-velocity integral was used to compute the evolution of the wave. The results based on kinetic energy are correct to at least five decimal places in comparison to the linear theory for the cases shown. Again the results suggest that the discretization requires at least a wall-normal resolution of N_3=48 points, a temporal resolution of Δt=10^{-2} or smaller, and an amplitude of A_1=10^{-2} or smaller. Note that in the curved channel case, however, disturbances amplitudes of A_1=10^{-5} or smaller began to cause numerical difficulties for Case 4. It was observed that for radii of curvature even larger than R_c = 1,000, numerical errors began to arise in all calculations. The metric terms defining the curved channel geometry lose precision for high R_c. To simulate very large radii of curvature, the curved channel geometry needs to be reformulated so that distances are non-dimensionalized with the channel height, h, instead of the radius of curvature, R_c.

	Case 3, Re=5,000, R_c=100			Case 4, Re=4,000, Rc=1,000		
N_3	ω_R	$\omega_I\ (f_1)$ x1,000	$\omega_I\ (E_1)$ x1,000	ω_R	$\omega_I\ (f_1)$ x1,000	$\omega_I\ (E_1)$ x1,000
24	0.374860	3.44599	3.28135	0.530855	-16.1705	-16.5948
32	0.374845	3.29589	3.28771	0.530914	-16.5031	-16.5704
40	0.374790	3.28305	3.28685	0.530800	-16.5703	-16.5726
48	0.374782	3.28548	3.28680	0.530781	-16.5723	-16.5728
56	0.374782	3.28550	3.28679	0.530779	-16.5727	-16.5728
exact	0.374757	3.28679	3.28679	0.530779	-16.5727	-16.5727

Table 4.6. Effect of Spatial Resolution on Computed Temporal Frequency ω_R and Temporal Growth Rate ω_I for Curved Channel.

	Case 3, Re=5,000, R_c=100			Case 4, Re=4,000, R_c=1,000		
Δt	ω_R	$\omega_I\ (f_1)$ x1,000	$\omega_I\ (E_1)$ x1,000	ω_R	$\omega_I\ (f_1)$ x1,000	$\omega_I\ (E_1)$ x1,000
10^{-1}	0.374738	3.28598	3.28674	0.530655	-16.5602	-16.5581
10^{-2}	0.374817	3.28564	3.28680	0.530779	-16.5723	-16.5726
10^{-3}	0.374822	3.28548	3.28680	0.530781	-16.5723	-16.5728
10^{-4}	0.374823	3.28546	3.28680	0.530781	-16.5723	-16.5728
10^{-5}	0.374823	3.28546	3.28681	0.530781	-16.5723	-16.5728
exact	0.374757	3.28679	3.28679	0.530779	-16.5727	-16.5727

Table 4.7. Effect of Temporal Resolution on Computed Temporal Frequency ω_R and Temporal Growth Rate ω_I for Curved Channel.

	Case 3, *Re*=5,000, R_c=100			Case 4, *Re*=4,000, R_c=1,000		
A_1	ω_R	$\omega_I\,(f_1)$ x1,000	$\omega_I\,(E_1)$ x1,000	ω_R	$\omega_I\,(f_1)$ x1,000	$\omega_I\,(E_1)$ x1,000
10^{-0}	0.374785	3.26480	3.25982	0.530782	-16.6130	-16.6415
10^{-1}	0.374782	3.28537	3.28653	0.530781	-16.5727	-16.5735
10^{-2}	0.374782	3.28549	3.28679	0.530781	-16.5723	-16.5728
10^{-3}	0.374782	3.28548	3.28680	0.530781	-16.5723	-16.5728
10^{-5}	0.374782	3.28548	3.28681	0.530781	-16.5721	-16.5727
exact	0.374757	3.28679	3.28679	0.530779	-16.5727	-16.5727

Table 4.8. Effect of Initial Amplitude on Computed Temporal Frequency ω_R and Temporal Growth Rate ω_I for Curved Channel.

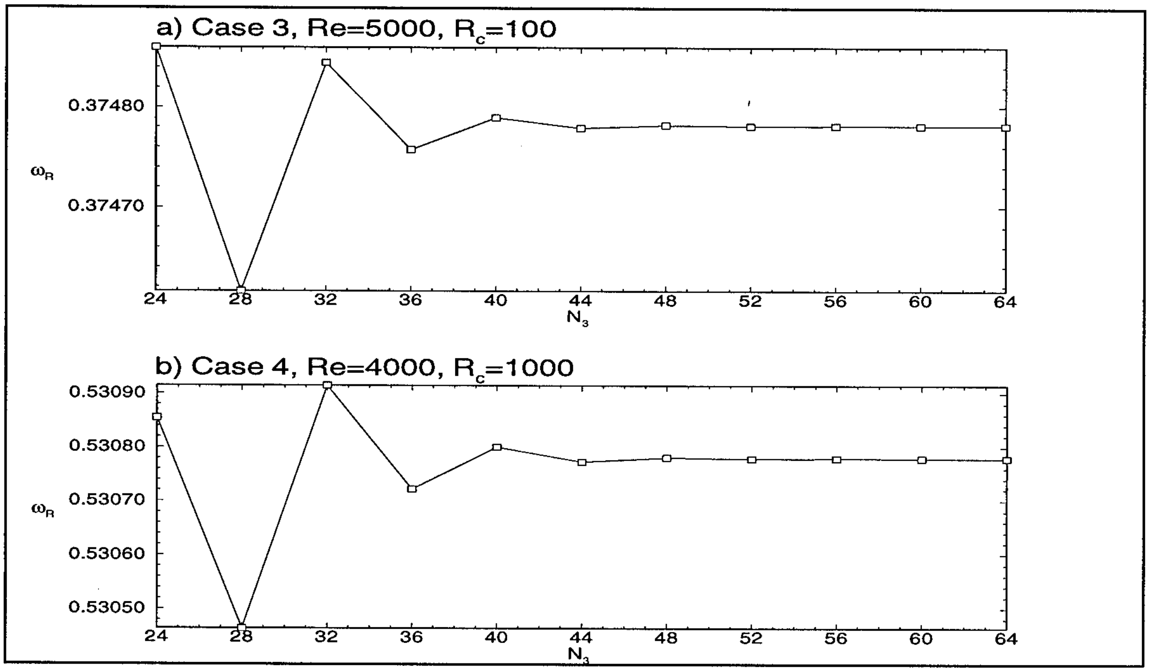

Figure 4.30. Effect of Spatial Discretization on Computed Linear Frequency for Curved Channel, a) Case 3, and b) Case 4.

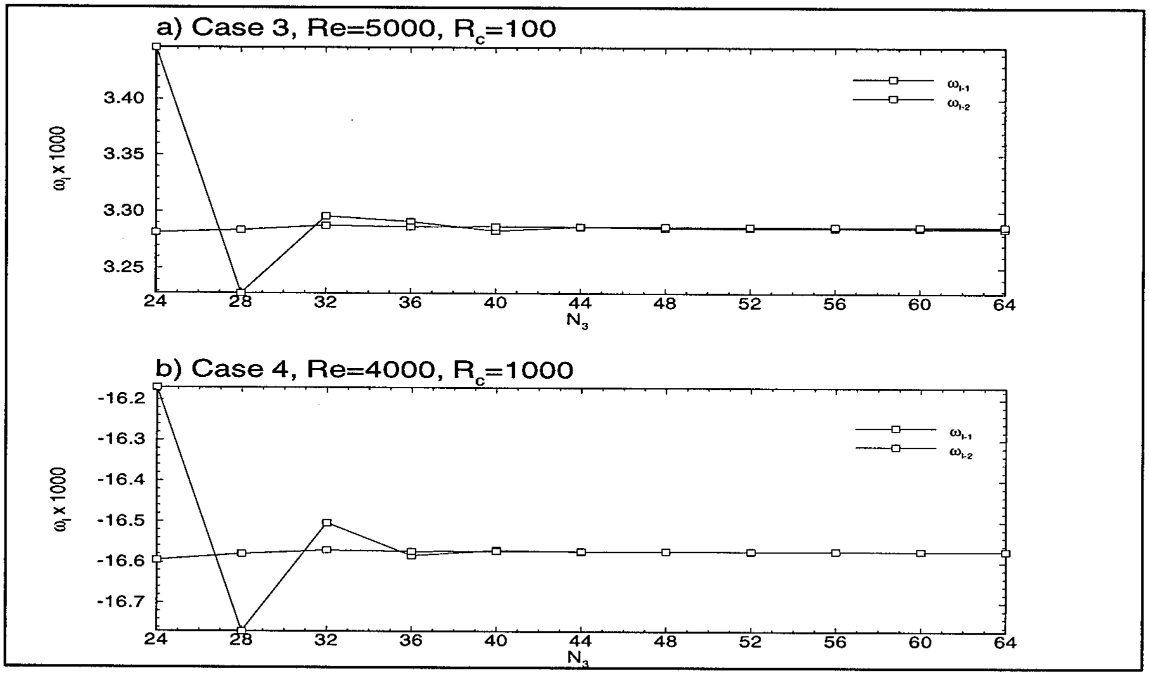

Figure 4.31. Effect of Spatial Discretization on Computed Linear Growth Rate, ω_I, for a) Case 3, and b) Case 4. The solid symbols show values computed from $f_1(\xi^1)$ and the hollow symbols are computed from $E_I(\xi^1)$.

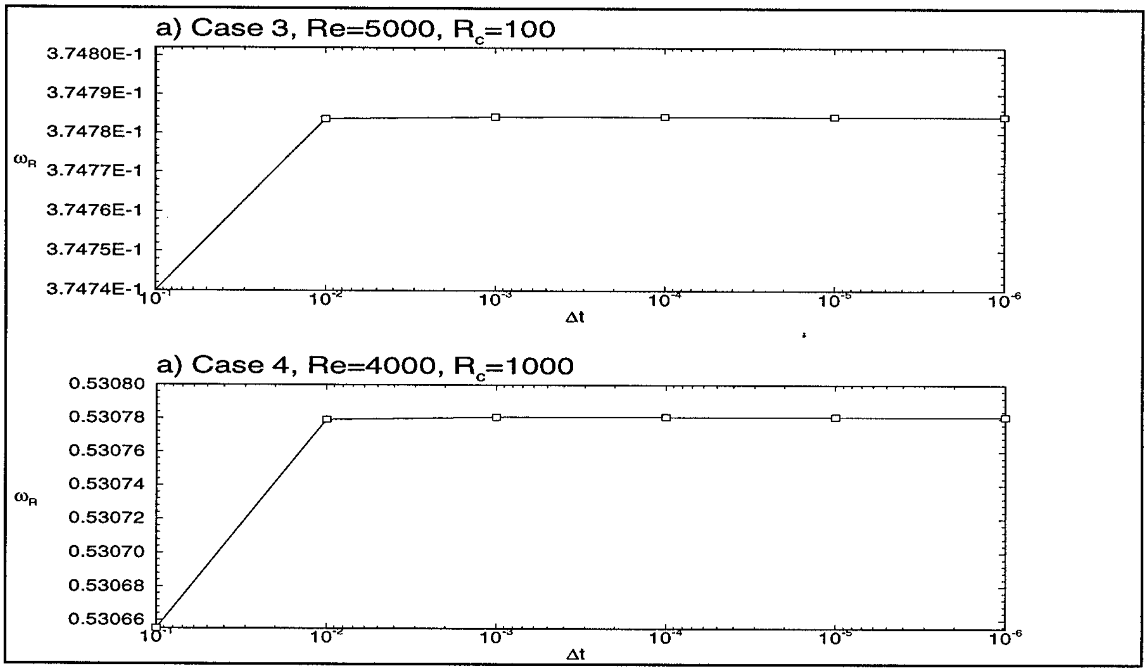

Figure 4.32. Effect of Temporal Discretization on Computed Linear Frequency for Curved Channel, a) Case 3, and b) Case 4.

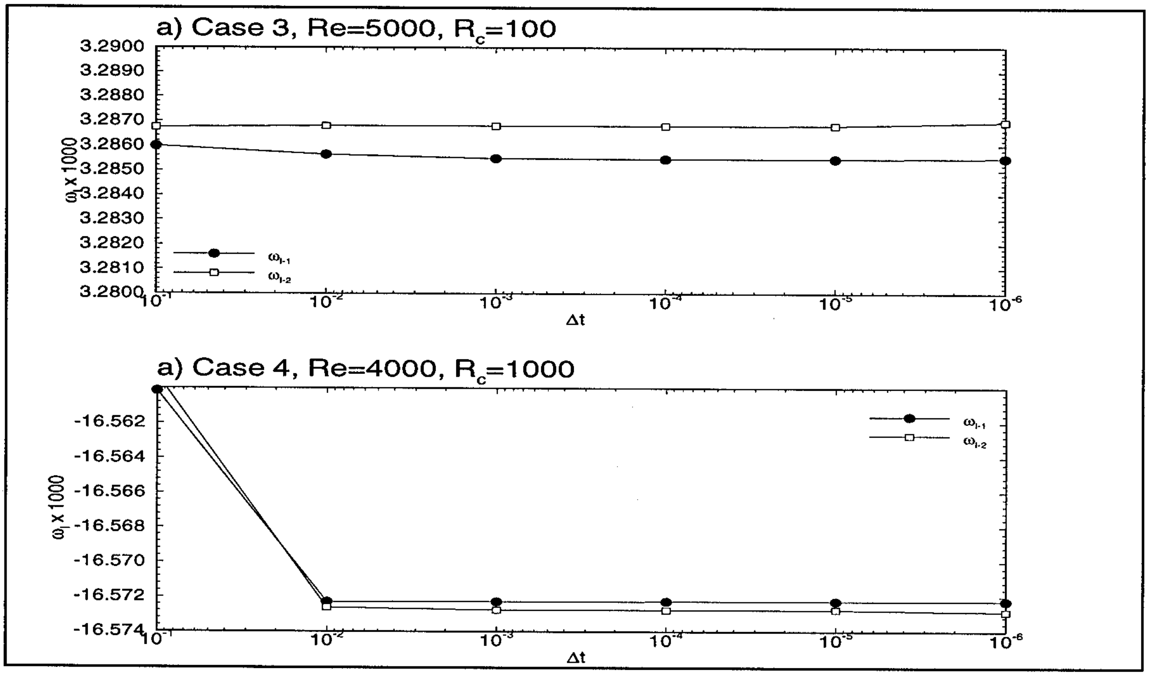

Figure 4.33. Effect of Temporal Discretization on Computed Linear Growth Rate, ω_I, for a) Case 3, and b) Case 4. The solid symbols show values computed from $f_1(\xi^1)$ and the hollow symbols are computed from $E_1(\xi^1)$.

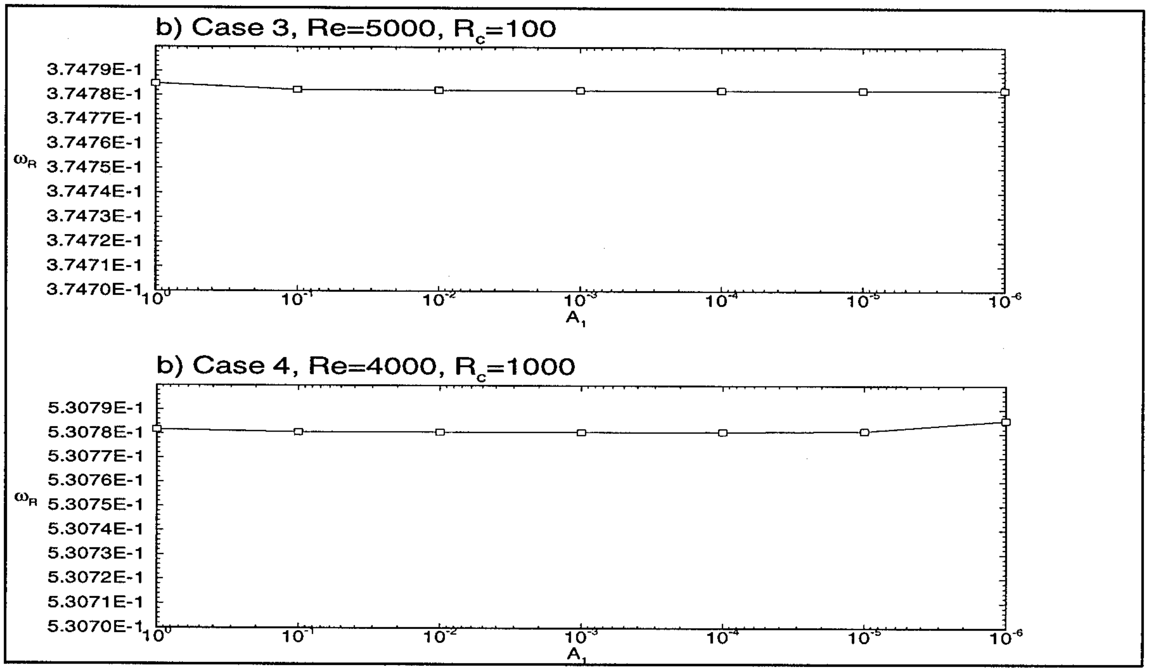

Figure 4.34. Effect of Disturbance Amplitude on Computed Linear Frequency for Curved Channel, a) Case 3, and b) Case 4.

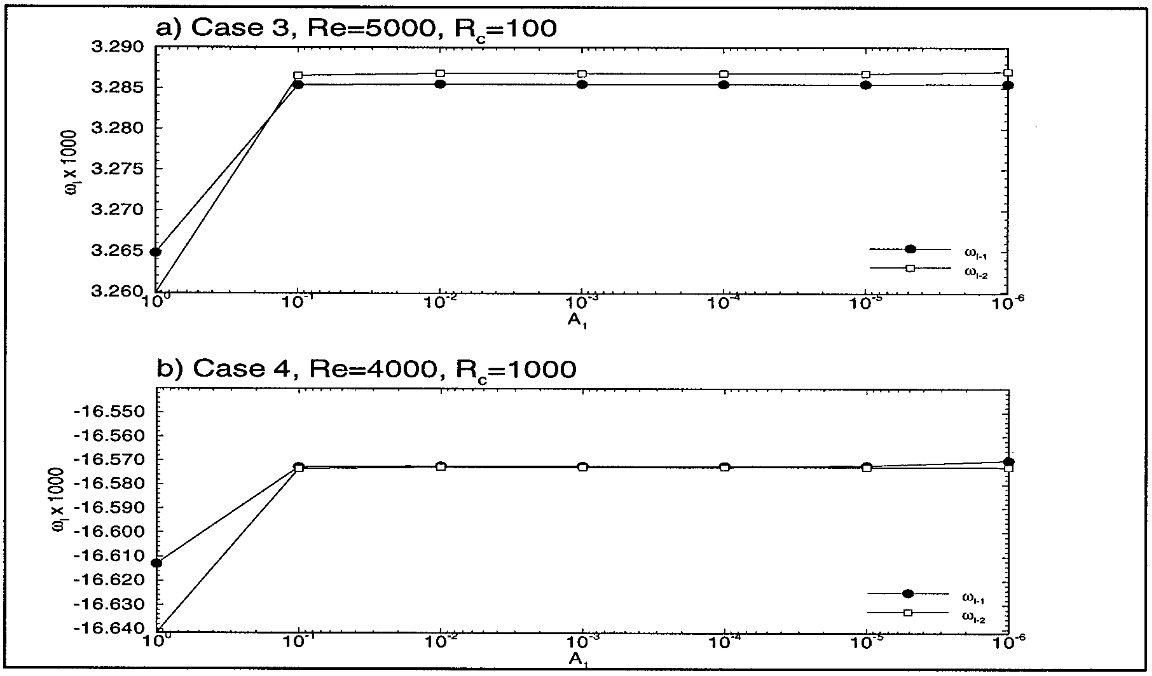

Figure 4.35. Effect of Disturbance Amplitude on Computed Linear Growth Rate, ω_I, for a) Case 3, and b) Case 4. The solid symbols show values computed from $f_1(\xi^1)$ and the hollow symbols are computed from $E_1(\xi^1)$.

4.4. Nonlinear Stability Results for Plane Channel Flow

In addition to the forcing function tests and linear stability validations, a limited number of runs were performed to validate the code for nonlinear stability calculations and to study the effects of nonlinearity on the solution. Plane channel results were obtained for Cases 1 and 2 in Tab. 4.2. In addition, a few curved channel results were obtained, but they showed few qualitative differences from the plane channel results and will not be shown here.

The results show the effects of nonlinearity on the early flow evolution of the primary mode. The threshold initial amplitude above which nonlinear behavior occurs is explored. In addition, for Case 2, it appears that an equilibrium state is being approached in the long time evolution. Plots of the flow field after twenty periods of the Tollmien-Schlichting wave show that the flow resembles the finite-amplitude states observed in experiments and simulations.

Two validations were available for the nonlinear results for the plane channel. The direct simulation code of Zang (1984) was used to obtain results for the conditions of Case 1. These results compared well with the results obtained in this study. In addition, a finite-amplitude state was computed in Orszag and Patera (1983) for the conditions of Case 2. These results also compare well.

4.4.1. Early Time Results

Results were obtained for Case 1 and Case 2 for varying values of initial amplitude, A_1. The kinetic energy of the primary mode is shown as a function of time for these cases in Figs. 4.36 and 4.37, respectively. The results show several interesting trends. In all cases, the initial evolution closely matches linear stability theory, which predicts exponential growth (which appears as linear on a log plot). However, during the first period of the Tollmien-Schlichting wave, the high amplitude cases begin to deviate from linear evolution. For Case 1, the high amplitude result, with $A_1 = 0.1$, is amplified super-exponentially, through the nonlinear interactions between the fundamental mode and its harmonics. In contrast, the energy for $A_1 = 0.01$ grows exponentially, though the growth rate is slightly higher than the linear stability result.

For Case 2, the flow is linearly stable, and the disturbances initially decay according to linear theory. However, about half-way through the first period, the kinetic energy of the primary mode for initial amplitudes higher than $A_1 = 0.01$ begins to slow its decay. For cases with initial amplitudes of $A_1 = 0.05$ and higher, the wave begins to grow.

In both of these cases, the effect of nonlinear interactions is to destabilize the primary mode, causing it to increase super-exponentially for the linearly unstable case, and to reverse its growth in the linearly stable case. Referring to the weakly nonlinear theory of §1.1.3, these effects confirm that the Landau coefficient, ℓ, is positive for the plane channel. In this context, Case 2 is a case of subcritical instability. Though the flow is linearly stable, it is unstable to disturbances of a finite size. However, note that the evolution predicted by the Landau equation, Eq. (1.1), differs from these results in a significant way. The Landau equation does not predict that the mode will first grow or decay according to linear theory, and then deviate from this after some time. Rather it predicts monotonic growth for an intial amplitude above a threshold amplitude, A_e. In the present results, A_e is approximately 0.06. For initial amplitudes above A_e, the disturbance first decays, and then grows. This suggests that other mechanisms are at work during the early transient which do not allow the primary mode to follow the evolution equation obtained from weakly nonlinear stability theory. One possible mechanism that could explain this behavior is that for large amplitudes, the least stable mode selected from linear stability theory, may not be the only mode which is being triggered by the nonlinear interactions. The effect of this is the modification of the shape of the primary disturbance during the early transient. After the transient, the mode shape remains fixed in shape and then evolves nonlinearly.

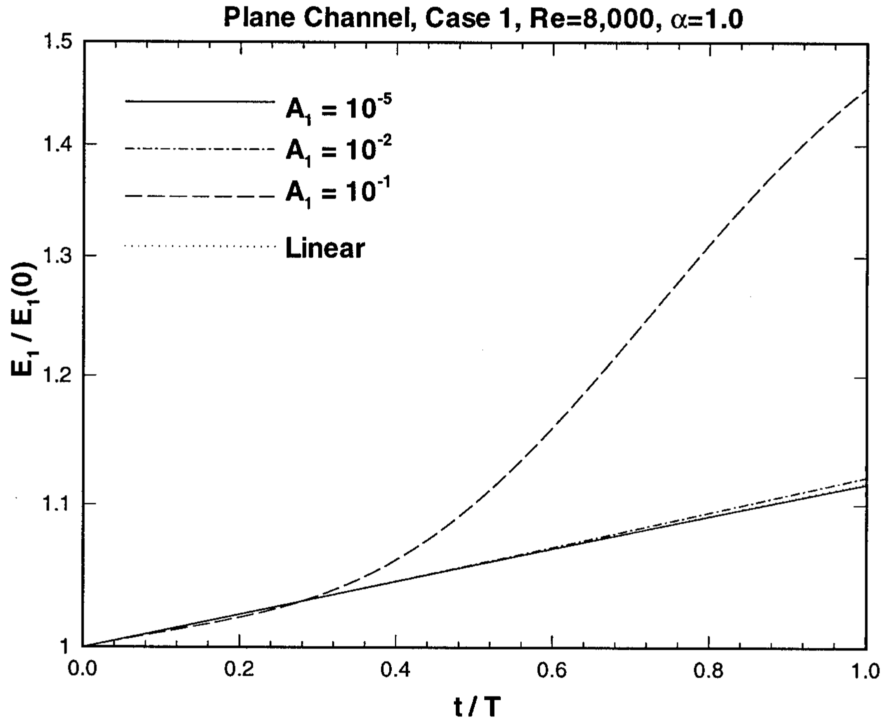

Figure 4.36. Growth of the primary disturbance mode for one period, *T*, of the Tollmien-Schlichting wave, for the plane channel, Case 1, with Re = 8,000 and α = 1.0. The results for A_1 = 0.1 show significant nonlinearity.

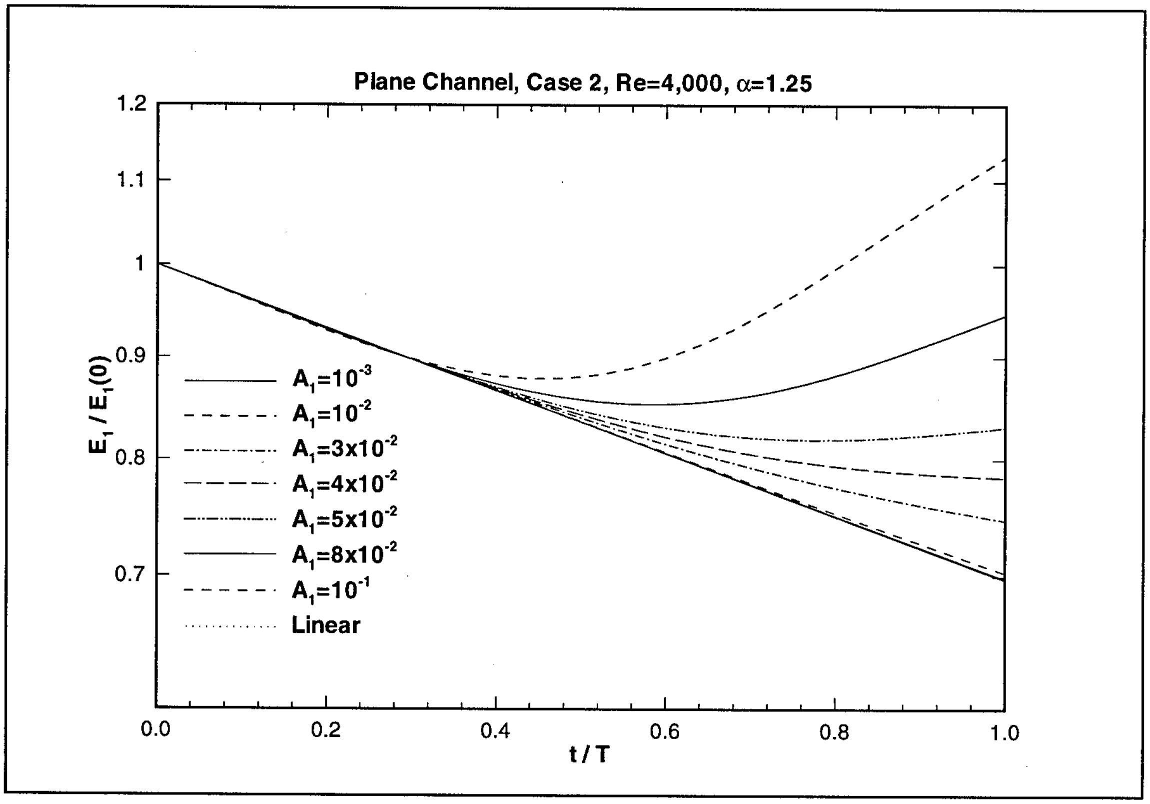

Figure 4.37. Growth of the primary disturbance mode for one period, T, of the Tollmien-Schlichting wave, for the plane channel, Case 2, with Re = 4,000 and α = 1.25. The results for $A_1 > 0.01$ show significant nonlinearity. In particular, the growth rate becomes positive for $A_1 > 0.04$.

4.4.2. Long Time Growth of the Primary Mode

The early time results suggest nonlinear evolution according to weakly nonlinear stability theory after a transient of about half of a period of the Tollmien-Schlichting wave. The next question to investigate is whether or not the early time evolution is indicative of the long time behavior. Fig. 4.38 shows the nonlinear growth of the high amplitude result from Case 1. The super-exponential growth during the first period does not continue. The growth rate decreases as the disturbance continues to grow. This is consistent with the notion that weakly-nonlinear ideas only apply for small amplitude disturbances. Once disturbances grow beyond this range, higher-order terms would be needed to predict the evolution of the disturbance. In the extreme, as the disturbance becomes of order 1, the asymptotic series approach completely breaks down, and an infinite number of terms would be needed to predict the fully nonlinear behavior.

Fig. 4.39 shows the evolution for Case 2 for the first five periods. The case with initial amplitude $A_1 = 0.05$ first decays, then grows, then decays. Eventually it will decay to zero amplitude. The energy for initial amplitude $A_1 = 0.08$ is growing slightly after 2 periods. After some additional investigation, not shown in these figures, the threshold amplitude, A_e, for Case 2 was determined to be approximately 0.06. The flow is stable to initial disturbances below this amplitude, and is unstable to disturbances above this amplitude.

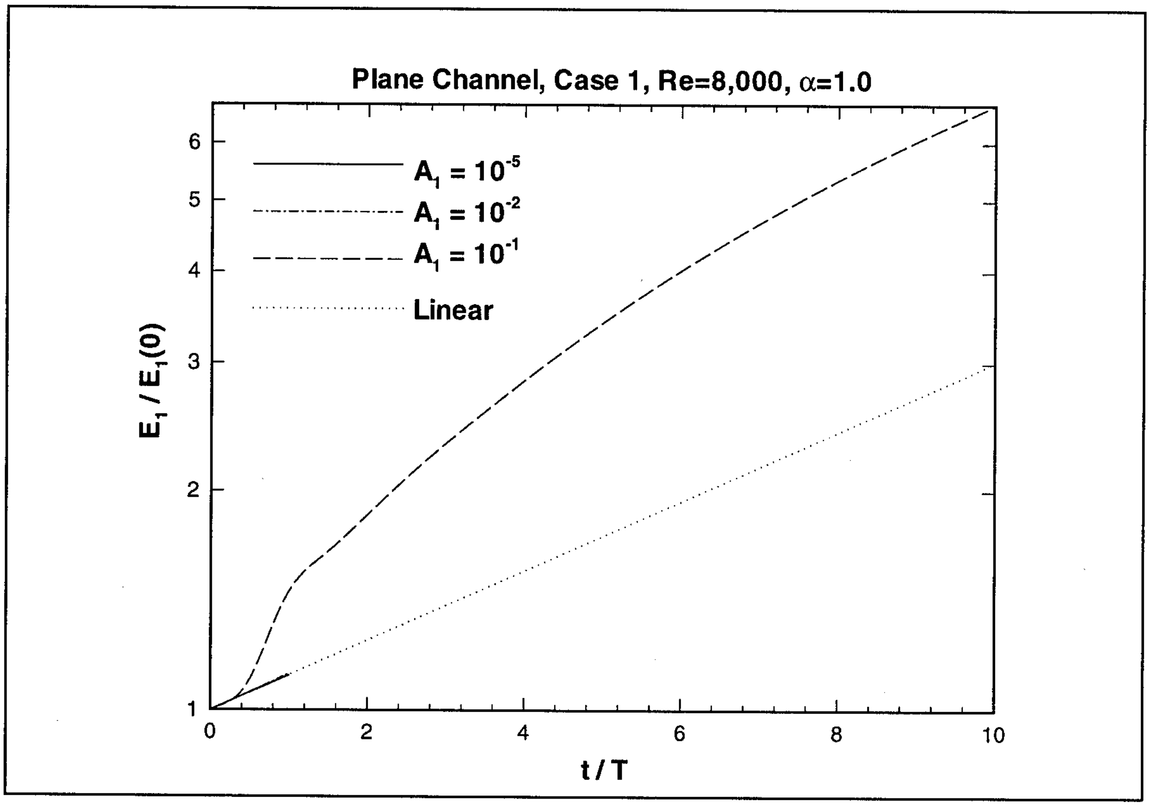

Figure 4.38. Growth of the primary disturbance mode for 10 periods of the Tollmien-Schlichting wave, for the plane channel, Case 1, with *Re* = 8,000 and $\alpha = 1.0$. The growth of the $A_1 = 0.1$ result slows significantly after the first period. Note that the $A_1 = 10^{-2}$ and $A_1 = 10^{-5}$ solutions were obtained for only one period.

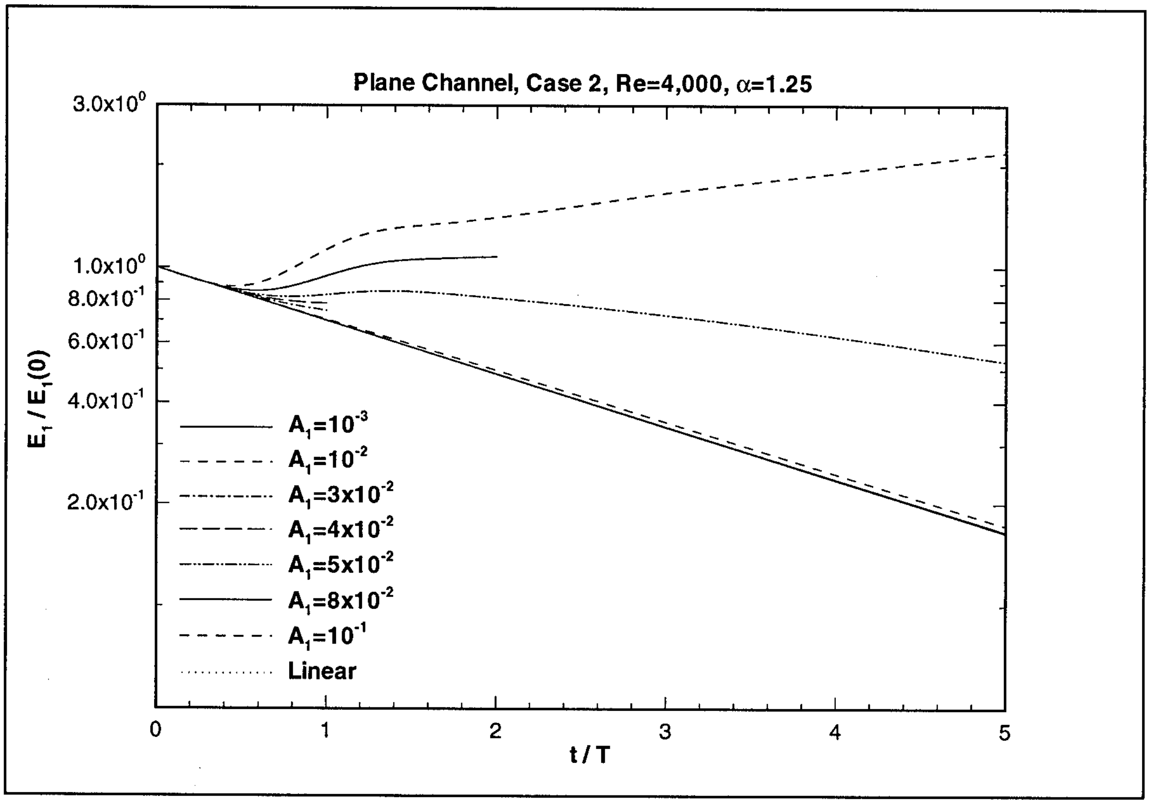

Figure 4.39. Growth of the primary disturbance mode for 5 periods of the Tollmien-Schlichting wave, for the plane channel, Case 2, with *Re* = 4,000 and $\alpha = 1.0$. The critical value of A_1 for long term growth is approximately 0.06. Initial disturbances above this amplitude will not decay.

4.4.3. Evolution of Harmonic Modes

Results are shown for Cases 1 and 2 to demonstrate the nonlinear behavior of the first three harmonic modes. The modes are designated in the manner commonly used in the literature. The mode number (k,ℓ) denotes the mode with a streamwise wavenumber, k, and a spanwise wavenumber ℓ. In this case, the primary mode is denoted (1,0), and its harmonics are (2,0), (3,0), (4,0). For Case 1, with $A_1 = 0.001$, the results are shown in Fig. 4.40, and are compared with the results of Zang (1984). The initial conditions were slightly different between the present results and the results of Zang, and this leads to an interesting observation. The initial conditions for present results were comprised of the base flow, the primary disturbance, and harmonics of the primary disturbance at an amplitude smaller than the primary mode. For the results of Fig. 4.40, the initial condition was obtained with $A_1 = 0.001, A_2 = 0.0001, A_3 = A_4 = 0$. The results of Zang were obtained with $A_1 = 0.001, A_2 = A_3 = A_4 = 0$. After a short-time transient, the two results match fairly well, indicating that the initial amplitude of the harmonics is irrelevant for determining the evolution of the flow. Only the amplitude of the primary mode is important, as it will quickly force the harmonic modes at certain amplitudes independent of their initial amplitudes. This observation was reinforced by many other results not shown here.

The harmonics are shown for Case 2, with $A_1 = 0.001$, for twenty periods of the Tollmien-Schlichting wave. Fig. 4.41 shows that the primary mode decays exponentially. The second mode also decays exponentially. However, the third mode stops its decay after several periods, and then stabilizes at a fixed amplitude. This behavior leaves the issue of the long-time behavior of this flow a mystery. When the primary mode decays to the level of the (3,0) mode, it is possible that it will also stabilize, through interactions with this harmonic. It is also possible that the nonlinear interactions will cause the primary to begin growing again. This suggests that in the case of subcritical instability, the threshold amplitude for long-time stability may be quite small. Though a much larger disturbance was required in order to observe nonlinear growth (and therefore subcritical instability) in the early time evolution, it is possible that the actual threshold amplitude for stability is much smaller.

The long time behavior of Case 2, with $A_1 = 0.1$, is shown in Fig. 4.42. The harmonics in this case all behave nonlinearly, as does the primary mode. After 20 periods of the Tollmien-Schlichting wave, the growth rate decreased significantly from the initial nonlinear growth. The harmonics behave in a similar manner as the primary mode. The evolution of these modes seems to suggest that the primary mode and its harmonics are approaching an equilibrium state. This state, called a finite-amplitude state, is one in which the nonlinear interactions between the primary mode and its harmonics reaches an equilibrium. This represents a bifurcation of the flow to a new state, which is stable to streamwise disturbances (note that the secondary instability of this state to spanwise disturbances will cause it to break down as discussed in Section 1.) The long time evolution of subcritical instability, therefore, is to a stable equilibrium, given a large enough disturbance. As was mentioned above, it is possible that smaller initial disturbances may also eventually lead to growth, in which case, the same equilibrium should be achieved as for the high amplitude case.

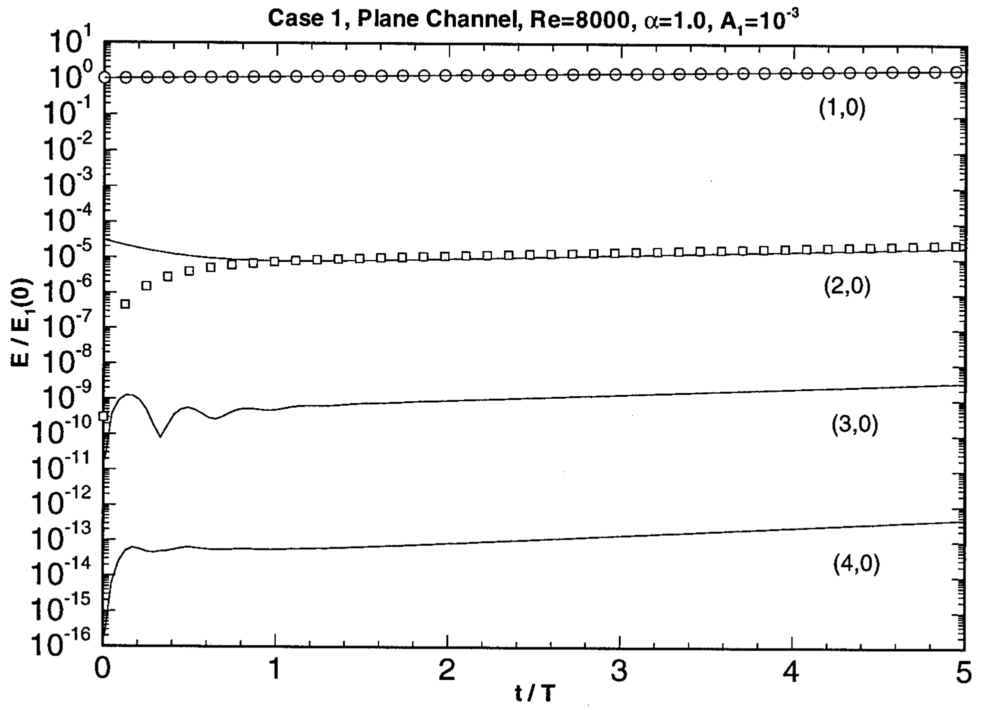

Figure 4.40. Growth of the primary disturbance mode (1,0) and its harmonics (2,0), (3,0), and (4,0) for 5 periods of the Tollmien-Schlichting wave, for the plane channel, Case 1. The symbols are the results of Zang (1988a) for similar conditions, but with a different initial amplitude for the harmonic (2,0).

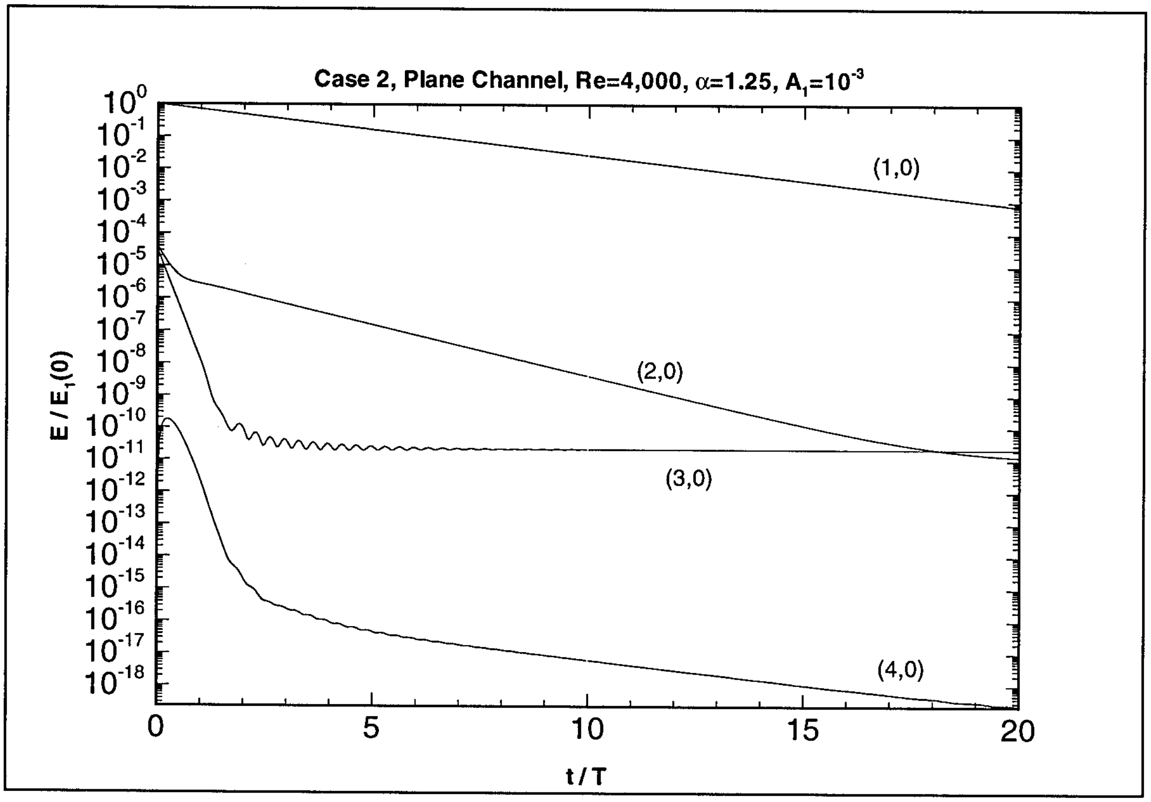

Figure 4.41. Growth of the primary disturbance mode (1,0) and its harmonics (2,0), (3,0), and (4,0) for 20 periods of the Tollmien-Schlichting wave, for the plane channel, Case 2. The initial amplitude is 0.001. The (3,0) modes stops decaying after about 2 periods, suggesting that after a long time nonlinear interactions may force subsequent growth of the primary mode.

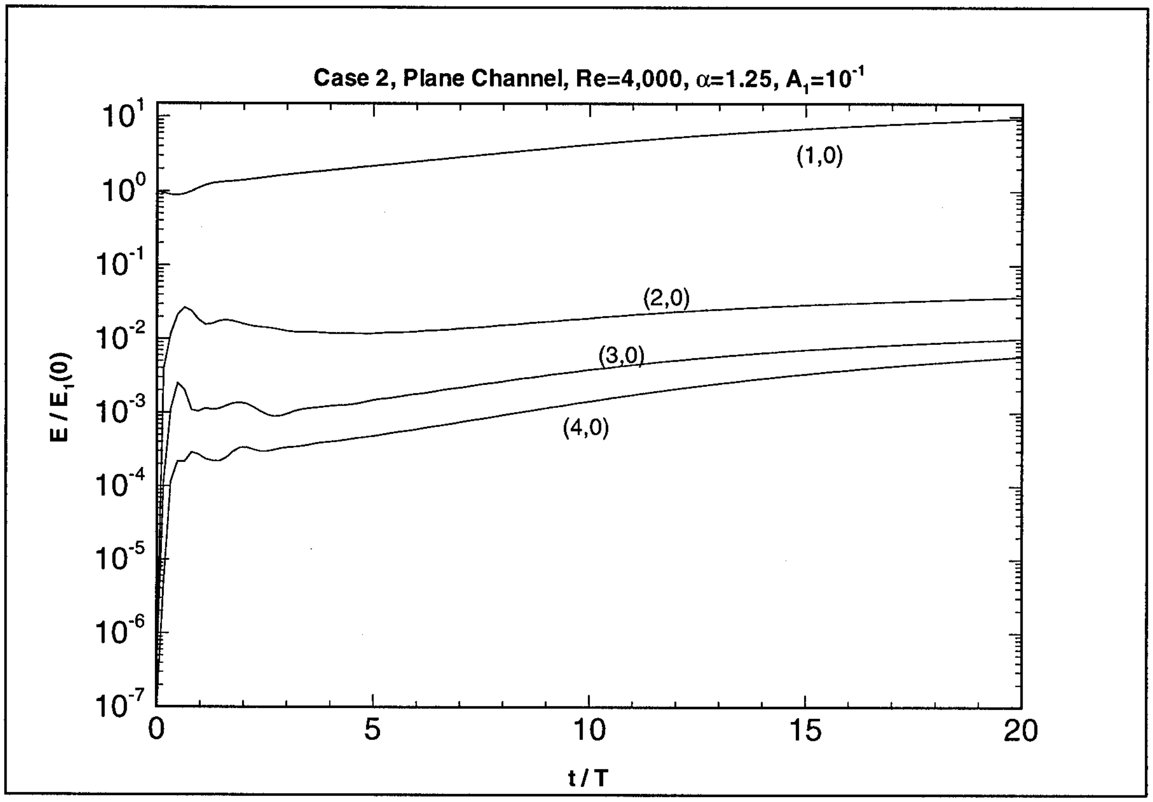

Figure 4.42. Growth of the primary disturbance mode (1,0) and its harmonics (2,0), (3,0), and (4,0) for 20 periods of the Tollmien-Schlichting wave, for the plane channel, Case 2. The initial amplitude is 0.1. Though this case is linearly stable, the disturbances are growing to a large amplitude. This is an example of subcritical instability.

4.4.4. Finite Amplitude State for Plane Channel Flow

The flow field for Case 2, with an initial amplitude $A_1 = 0.1$, was investigated at the time $t = 20\ T$. The results were in good agreement with the computation of a finite-amplitude state performed by Orszag and Patera (1983). Figs. 4.43 and 4.44, respectively, show contours of the disturbance qualities, including vorticity, and the total flow quantities. In addition, Fig. 4.45 shows vectors and streamlines of the disturbance velocity field. The finite-amplitude Tollmien-Schlichting wave is somewhat distorted from its initial shape, but retains its basic structure. Compare with the initial shape given in Fig. 4.15. The disturbance has approximately tripled in amplitude from its initial amplitude, and thus the disturbance is sufficiently large to significantly effect the total streamwise velocity and vorticity, as shown in Fig. 4.44. A pronounced waviness can be seen in the flow. This is consistent with experimental observations of instability waves in shear flows. They are typically sufficiently large to be observed in flow visualizations. The streamlines of Fig. 4.45 appear similar to the finite amplitude state computed by Orszag and Patera (1983) for the same Reynolds number and streamwise wavelength.

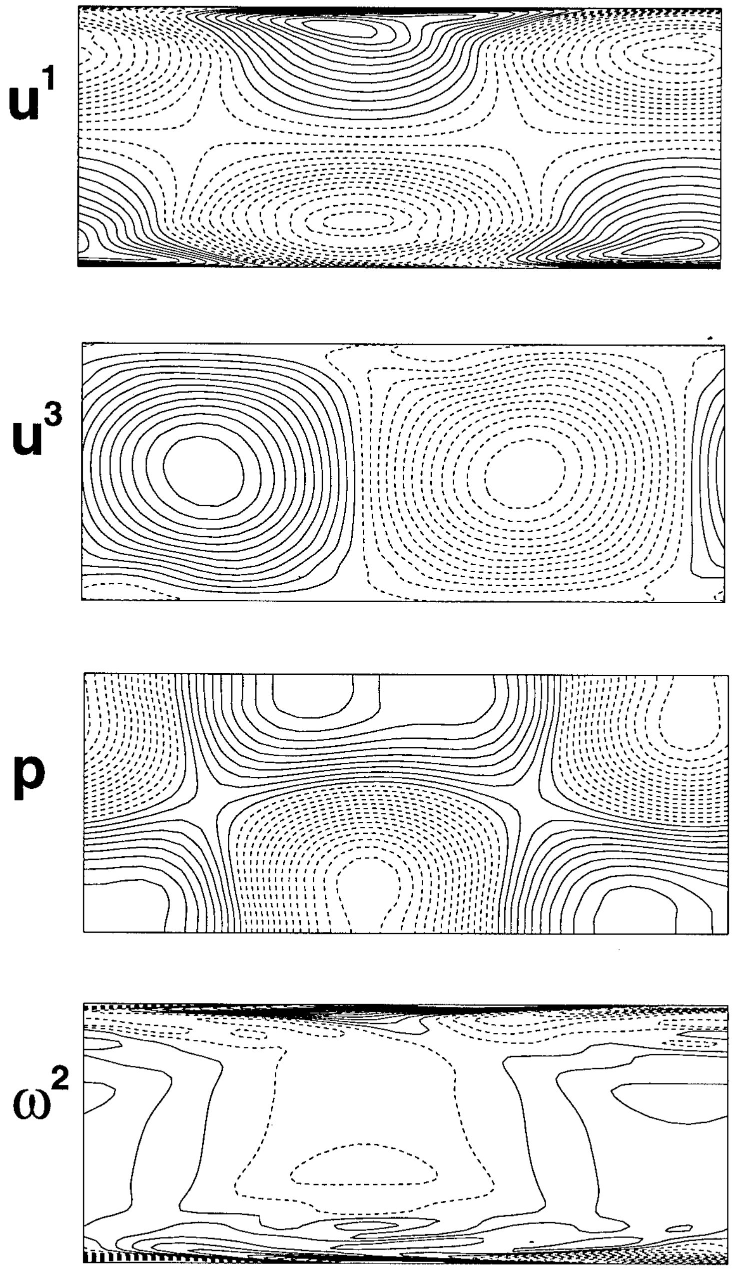

Figure 4.43. Contours of disturbance quantities after 20 periods of the Tollmien-Schlichting wave for the plane channel, Case 2. The flow is approaching a finite-amplitude state. This state is notably different than the original Tollmien-Schlichting wave disturbance.

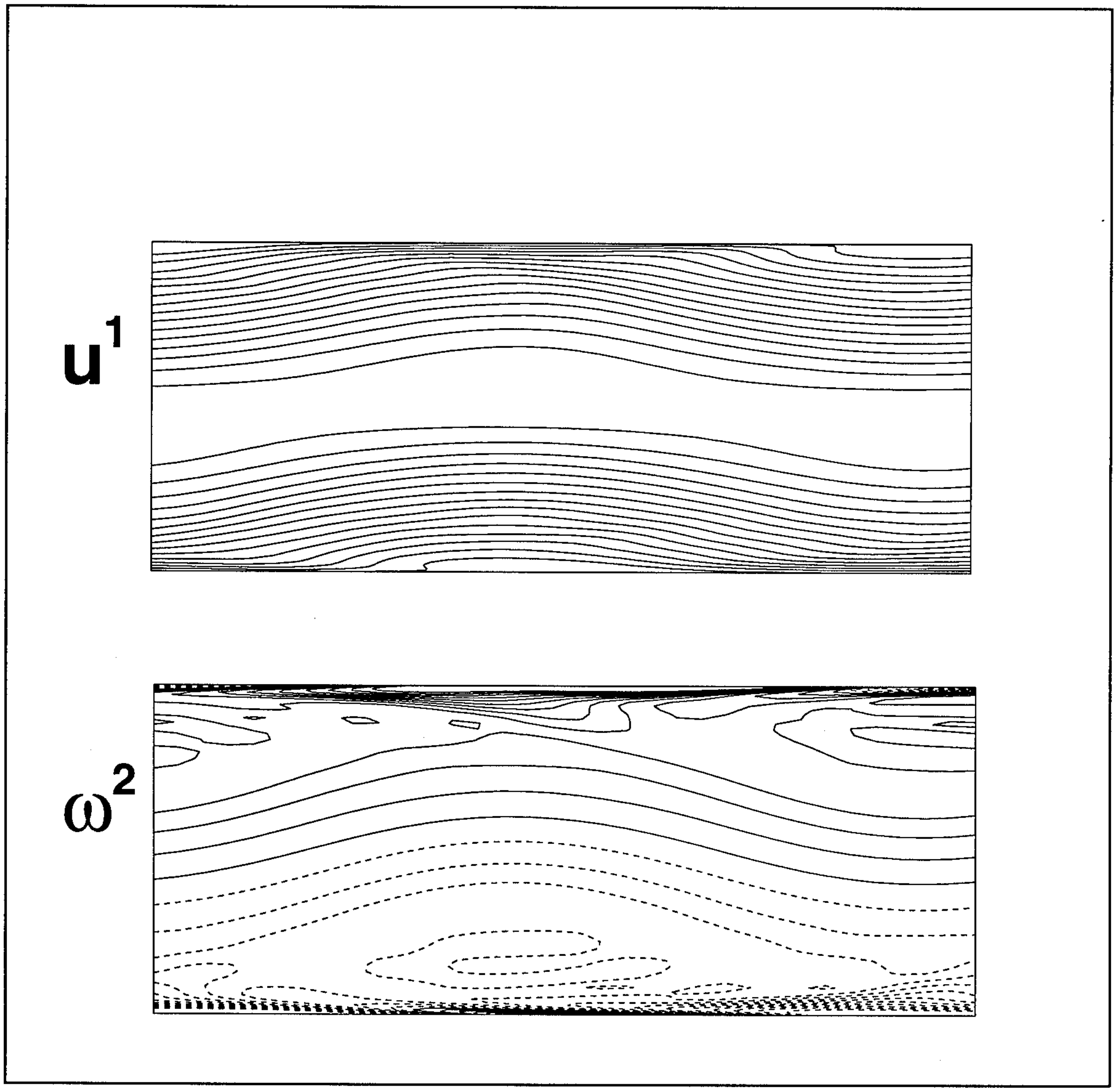

Figure 4.44. Contours of total streamwise velocity and vorticity after 20 periods of the Tollmien-Schlichting wave for the plane channel, Case 2. The growth of the disturbance has significantly altered the appearance of the flow.

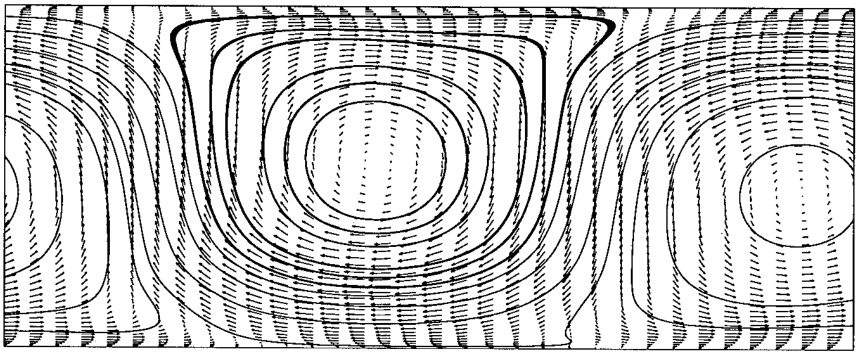

Figure 4.45. Vectors and streamlines of the disturbance velocity after 20 periods of the Tollmien-Schlichting wave for the plane channel, Case 2. The streamlines match the results of Orszag and Patera (1983).

4.5. Summary

The results of this chapter serve first to validate the numerical approach. They demonstrate spectral accuracy both in the overall truncation error, as shown in the analytical function analysis, and in the linear stability results. However, the limitations of the current scheme are also revealed. Round-off error is a potential problem for a large number of grid points, for small time steps, and for small disturbance amplitudes. The only solution for these problems is to use a higher precision level in computing certain terms, as discussed in §4.1.5. These problems have not affected the solutions of interest, however, and will be left for future study.

Secondly, the results obtained thus far have investigated some of the effects of nonlinearity of Tollmien-Schlichting waves in 2-D plane and channel flows. These results show that disturbance amplitudes of the order of 1% of the streamwise mean flow or higher are needed in order to observe nonlinear behavior. This is consistent with the general consensus in the literature that “small amplitude” disturbances are those with amplitude less than 1%, implying that nonlinear behavior begins to occur near 1%. Also, the threshold amplitude for subcritical instability of plane channel flow at a Reynolds number of 4,000 was determined to be approximately 6%, though the actual value may be much lower if nonlinear growth appears only after a long time. For amplitudes above this threshold, the disturbance will eventually cause the flow to bifurcate to a finite amplitude state, at which the amplitude of the primary mode is approximately 30% of the mean flow. These results are just a tiny sample of the nonlinear results that can be obtained using the numerical approach developed in this study. Much work remains to be done to employ the numerical tool which has been developed to further investigate the nonlinear evolution of instabilities.

Section 5. Conclusions and Recommendations

The purpose of this work was achieved not only in the final outcome, represented by the plots and tables of results, but by the development of a methodology for studying the stability of shear flows. Further development and validation is needed to complete the 3-D version of the computer code. In addition, more-complex channel flow geometries need to implemented. Both of these additions to the current code must be carefully validated. These are the next steps of this study. Looking beyond these steps, however, recommendations can be made for the future use of the methodology described in this study. This methodology should be used for the investigation of current nonlinear stability problems. Three major areas of investigation are discussed below, along with the recommendations for study using the 3-D generalized channel code.

5.1. Nonlinear Wave Interactions

The recent advances in the field of instability and transition to turbulence have largely focused on the investigation of nonlinear interactions between various instability waves. These interactions have been determined in experiments to be critical to the understanding of many prevalent flow configurations in which different instability mechanisms compete for dominance. Numerous theoretical studies, usually combined with a significant amount of computation, have investigated various types of wave interactions and have attempted to explain experimental observations. Some examples of problems in which wave interactions are important are the flow over a swept wing (Reed and Saric, 1989), the secondary instability of Tollmien-Schlichting waves in a boundary layer (Orszag and Patera, 1983), and the Tollmien-Schlichting wave-Dean vortex interaction in curved channel flows {Singer, Erlebacher and Zang, 1992) Wave interactions are responsible for many of the remaining unanswered questions in the study of transition to turbulence.

Many of the current studies of wave interactions have used either plane or curved channel flows as the geometry of interest. This is due to the fact that plane channels exhibit many of the characteristics of plane boundary layers and can be used to investigate secondary instability and nonlinear breakdown at a lower cost than the comparable boundary layer simulations (Kleiser and Zang, 1989). Also, curved channel flow is one of the simplest settings for the study of curvature-induced instabilities. The 3-D general channel code can be used to further investigate nonlinear wave interactions in plane and curved channels. Results of other authors for secondary instability and Tollmien-Schlichting wave-streamwise vortex interactions in plane and curved channels should be reproduced and advanced. In addition, the generalized coordinate system could be used to provide small perturbations on the channel walls which could alter the wave interactions and lead to a different route to turbulence. This area has been investigated very little in existing literature.

5.2. Linear and Nonlinear Stability of Complex Flows

In flows of engineering interest, many shear layers exist with different spatial scales and different stability characteristics. Recent studies have investigated sample complex flows in which, for example, regions of separated flow occur in addition to the boundary layer or other shear layers. Some of these studies are flow over a cylinder (Tomboulides, Triantafyllou and Karniadakis, 1992), over a backward-facing step (Kaiktsis, Karniadakis and Orszag, 1991), and in the "eddy-promoter" channel, that is a channel with a small cylinder imbedded in it to cause small scale separation (Karniadakis, Mikic and Patera, 1988, and Karniadakis and Triantafyllou, 1992). For these flows, a simple analytical base flow is not available, and consequently, the linear stability characteristics of that base flow are not known. Numerical simulation must be used to determine the base flow, and then to investigate the linear stability. Nonlinear stability results then follow. Recent results have suggested that the Tollmien-Schlichting wave phenomenon is very dominant even in flows which are significantly different from canonical flows. However, the growth rate of the Tollmien-Schlichting wave is significantly influenced by the presence of additional shear layers in the base flow.

The general channel geometry is well-suited to the investigation of complex flows. Though the current spectral method requires a smooth, analytical coordinate transformation, smooth cavities, grooves, and obstacles can be placed on the surface of the channel and can cause flow separation and the occurrence of multiple shear layers of different scales within the flow. A wealth of information can be obtained, even with only a 2-D simulation. The effects of spanwise disturbances can only be investigated after the evolution of the 2-D Tollmien-Schlichting wave is determined. The first step in this direction would be to reproduce the results of Guzmán and Amon (1982) for the flow in a periodic converging-diverging channel. A consistent methodology for computing the base flow and the linear stability characteristics should be determined. Then, other geometries should be investigated. Eventually, 3-D simulations should be performed to study the breakdown of Tollmien-Schlichting waves due to spanwise disturbances in these flows.

5.3. Dynamical Systems Explanations of Turbulence

A third, and somewhat overlapping, area of current research in instability and transition is the application of dynamical systems theory to examine the temporal behavior of flows in transition. These theories look at the temporal evolution of the most unstable eigenvalue of the Navier-Stokes equations, linearized about the current state. The bifurcation of the flow solution from one state to another can be explained as eigenvalues of the solution crossing from the stable regime to the unstable regime.

Currently, several scenarios of bifurcation are thought to pertain to the transition of flows from a laminar state to a turbulent state. The Ruelle-Takens-Newhouse scenario occurs as a sequence of Hopf bifurcations as the Reynolds number is increased slowly in time. That is, a stable flow becomes unstable when the first eigenvalue pair crosses the growth-rate=0 axis. The flow will then bifurcate to a periodic flow with a single frequency. This process is repeated when a second eigenvalue pair becomes unstable and adds a second frequency to the flow, making it quasi-periodic. Dynamical systems theory suggests that when a third frequency appears, incommensurate with either of the first two, the nonlinear interactions will quickly fill in the frequency spectrum and a non-periodic state will occur. This state is called chaos. A second scenario, the Feigenbaum scenario explains an alternate route to chaos through repeated period-doubling bifurcations. This scenario and others are described in Guckenheimer (1986).

These theories can be investigate and/or used to explain the early stages of transition in channel flows. The most notable use of the above explanations is in Taylor-Couette flow, or the flow between two concentric cylinders driven by the motion of one or both of the cylinders. This is not a channel flow due the difference in wall boundary conditions, but could certainly be investigated using the methodology developed in this study by simply applying non-zero wall velocities and by removing the pressure gradient which drives channel flows. See the simulation of Streett and Hussaini (1991). Applications to channel flows induced by a pressure gradient have also been investigated, most notably curved channel flow (Finlay, Keller and Ferziger, 1988). Guzmán and Amon (1994) show that the 2-D flow in their periodic converging-diverging channel follows the Ruelle-Takens-Newhouse scenario as the Reynolds number is increased.

There are many directions to pursue to investigate the applicability of dynamical systems approaches to explanations of transition. Again, the first step is to reproduce some of the results found in the literature showing bifurcations to quasi-periodic flows or demonstrating period doubling. The next step is to search for new flows in which these phenomena occur. The effect of spanwise disturbances on the bifurcation process should also be investigated as it is probable that certain 2-D flows would never arise in a practical flow due to 3-D instability.

5.4. Summary

In summary, the study of the early stages of transition has many areas which need to be pursued. The general code described in this study can be used for a wide variety of problems which can address these areas. The next phase of this study will complete the development of the 3-D code, and then will select one of these areas to investigate in greater depth.

Bibliography

Amon, C.H., and Patera, A.T. 1989. Numerical Calculation of Stable Three-Dimensional Tertiary States in Grooved-Channel Flow. *Physics of Fluids A* **1**:2005-2009.

Bayly, B.J., Orszag, S.A., and Herbert, T. 1988. Instability Mechanisms in Shear-Flow Transition. *Annual Review of Fluid Mechanics* **20**: 359-391.

Bland, S.B., and Finlay, W.H. 1991. Transitions Toward Turbulence in a Curved Channel. *Physics of Fluids A* **3**(1): 106-114.

Blodgett, K. 1995. *A Spectral Multidomain Method in Generalized Curvlinear Coordinates with Application to Leading-Edge Receptivity.* Ph.D. Dissertation, University of Cincinnati.

Canuto, C., Hussaini, M.Y., Quarteroni, A., and Zang, T.A. 1988. *Spectral Methods in Fluid Dynamics.* Springer-Verlag.

Choudhari, M. 1993. Boundary-Layer Receptivity Due to Distributed Surface Imperfections of a Deterministic or Random Nature. *Theoretical and Computational Fluid Dynamics* **4**: 101-117.

Crouch, J.D., and Herbert, T. 1993. Nonlinear Evolution of Secondary Instabilities in Boundary-Layer Transition. *Theoretical and Computational Fluid Dynamics* **4**: 151-175.

Danabasoglu, G., and Biringen, S. 1991. Spatial Simulation of Instability and Control by Periodic Suction and Blowing. *Physics of Fluids A* **3**: 2138-2147.

Drazin, P.G., and Reid, W.H. 1981. *Hydrodynamic Stability.* Cambridge University Press.

Finlay, W.H., Keller, J.B., and Ferziger, J.H. 1988. Instability and Transition in Curved Channel Flow. *Journal of Fluid Mechanics* **194**: 417-456.

Finlay, W.H., Nandakumar, K. 1990. Onset of Two-Dimensional Cellular Flow in Finite Curved Channels of Large Aspect Ratio. *Physics of Fluids A* **2**(7): 1163-1174.

Ghaddar, N.K., Korczak, K.Z., Mikic, B.B., and Patera, A.T. 1986. Numerical Investigation of Incompressible Flow in Grooved Channels: Part 1, Stability and Self-Sustained Oscillations. *Journal of Fluid Mechanics* **163**: 99-127.

Guckenheimer, J. 1986. Strange Attractors in Fluids: Another View. *Annual Review of Fluid Mechanics* **18**: 15-31.

Guo, Y., and Finlay, W.H. 1994. Wavenumber Selection and Irregularity of Spatially Developing Nonlinear Dean and Görtler Vortices. *Journal of Fluid Mechanics* **264**: 1-40.

Guzmán, A.M. and Amon, C.H. 1994. Transition to Chaos in Converging-Diverging Channel Flows: Ruelle-Takens-Newhouse Scenario. *Physics of Fluids A* 6(6): 1994-2002.

Hall, P., and Smith, F.T. 1989. Near-planar TS Waves and Longitudinal Vortices in Channel Flow: Nonlinear Interaction and Focusing. *ICASE Report No. 89-47.*

Henningson, D.S., and Reddy, S.C. 1994. On the Role of Linear Mechanisms in Transition to Turbulence. *Physics of Fluids A* **6**(3): 1396-1398.

Herbert, T. 1988a. Computer Code: Linear.x. Used with Permission.

Herbert, T. 1988b. Secondary Instability of Boundary Layers. *Annual Review of Fluid Mechanics* **20**: 487-526.

Kachanov, Y.S. 1994. Physical Mechanisms of Laminar-Boundary-Layer Transition. *Annual Review of Fluid Mechanics* **26**: 411-482.

Kaiktsis, L., Karniadakis, G.E., and Orszag, S.A. 1991. Onset of Three-Dimensionality, Equilibria, and Early Transition in Flow over a Backward-Facing Step. *Journal of Fluid Mechanics* **231**: 501-528.

Karniadakis, G.E., and Triantafyllou, G.S. 1992. Three-Dimensional Dynamics and Transition to Turbulence in the Wake of Bluff Objects. *Journal of Fluid Mechanics* **238**: 1-30.

Karniadakis, G.E., Mikic, B.B., and Patera, A.T. 1988. Minimum-Dissipation Transport Enhancement by Flow Destabilization: Reynolds' Analogy Revisited. *Journal of Fluid Mechanics* **192**: 365-391.

Kleiser, L., and Zang, T.A. 1991. Numerical Simulation of Transition in Wall-Bounded Shear Flows. *Annual Review of Fluid Mechanics.* **23**: 495-537.

Ligrani, P.M. 1992. Features of Wavy Vortices in a Curved Channel from Experimental and Numerical Studies. *Physics of Fluids A* **4**: 695-709.

Ligrani, P.M., and Niver, R.D. 1988. Flow Visualization of Dean Vortices in a Curved Channel with 40 to 1 Aspect Ratio. *Physics of Fluids* **31**(12): 3605-3617.

Nayfeh, A.H., and Al-Maaitah, A. 1988. Influence of Streamwise Vortices on Tollmien-Schlichting Waves. *Physics of Fluids* **31**: 3543-3549.

Orszag, S. A., and Patera, A. T. 1983. Secondary Instability of Wall-Bounded Shear Flows. *Journal of Fluid Mechanics.* **128**: 347-385.

Reed, H.L., and Saric, W.S. 1989. Stability of Three-Dimensional Boundary Layers. *Annual Review of Fluid Mechanics* **21**: 235-284.

Roberts, E.P.L. 1994. A Numerical and Experimental Study of Transition Processes in an Obstructed Channel Flow. *Journal of Fluid Mechanics* **260**:185-209.

Singer, B.A., Erlebacher, G., and Zang, T.A. 1992. A Weakly Nonlinear Theory for Wave-Vortex Interactions in Curved Channel Flow. *NASA TP-3158.*

Singer, B.A., Reed, H.L., and Ferziger, J.H. 1989. The Effects of Streamwise Vortices on Transition in the Plane Channel. *Physics of Fluids A* **1**: 1960-1971.

Sobey, I.J., and Drazin, P.G. 1986. Bifurcations of Two-Dimensional Channel Flows. *Journal of Fluid Mechanics* **171**: 263-287.

Streett, C.L., and Hussaini, M.Y. 1991. A Numerical Simulation of the Appearance of Chaos in Finite-Length Taylor-Couette Flow. *Applied Numerical Mathematics* **7**: 41-71.

Tomboulides, A.G., Triantafyllou, G.S., and Karniadakis, G.E. 1992. A New Mechanism of Period Doubling in Free Shear Flows. *Physics of Fluids A* **4**(7): 1329-1332.

Wolfram, S. 1991. *Mathematica: A System for Doing Mathematics by Computer.* Addison-Wesley Publishing Company, Inc.

Zang, T.A. 1984. Computer Code: SPCH. Used with Permission.

Zang, T.A., and Hussaini, M.Y. 1985a. Numerical Experiments on Subcritical Transition Mechanisms. *AIAA Paper 85-0296.*

Zang, T.A., and Hussaini, M.Y. 1985b. A Three-Dimensional Spectral Algorithm for Simulations of Transition and Turbulence. *ICASE Report No. 85-19.*

Zang, T.A., and Hussaini, M.Y. 1990. Multiple Paths to Subharmonic Laminar Breakdown in a Boundary Layer. *Physical Review Letters* **64**(6): 641-644.

Zang, T.A., and Hussaini, M.Y. 1987. Numerical Simulation of Nonlinear Interactions in Channel and Boundary-Layer Transition. *Nonlinear Wave Interactions in Fluids.* ASME Press.